NONLINEAR ATTITUDE CONTROL OF SPACECRAFT WITH STRAIN-ACTUATED SOLAR ARRAYS

BY

YASHWANTH KUMAR NAKKA

THESIS

Submitted in partial fulfillment of the requirements
for the degree of Master of Science in Aerospace Engineering
in the Graduate College of the
University of Illinois at Urbana-Champaign, 2016

Urbana, Illinois

Advisers:

Assistant Professor Soon-Jo Chung
Assistant Professor James T. Allison

Abstract

This thesis presents a mathematical framework for precision attitude control of a spacecraft using the inertial coupling between the spacecraft and solar arrays. The spacecraft with solar arrays is modeled as a one degree of freedom cylinder (rigid body rotation) with flexible appendages (infinite-dimensional system). The equations of motion that describe system evolution are derived using the extend generalizations of the Lagrangian for infinite dimension systems. Precision attitude control is achieved by bending the flexible appendage using strain actuators. Global asymptotic convergence of the controller's is proved using the Lyapunov direct method, which ensures that the control objectives of trajectory tracking and slewing are achieved. The Input-to-State stability of these controllers is used to generalize the control laws in terms of a variable that scales the stiffness term. The closed-loop system is simulated numerically for different values of the variable to verify stability.

An experimental setup, that mimics a spacecraft with solar arrays is designed as a cylinder that is secured to a flexible beam using an interference fit. The strain actuation of the beam is achieved using piezoelectric actuators. The rotation of the cylinder and bending in beam are estimated using measurements from a Vicon motion capture system. The closed-loop system is tested in real-time to achieve controlled rotation of the cylinder.

Acknowledgments

The author wishes to thank Dr. Soon-Jo Chung and Dr. James T. Allison for the opportunity to work on this project and for their guidance on this research. Special thanks to Dr.Jack B. Aldrich and Dr.Oscar S. Alvarez-Salazar of NASA Jet Propulsion Laboratory for insightful discussions during SASA project meetings. Finally, thanks to my parents and family for their support during the process of earning my Master's Degree.

Contents

List of Figures

List of Tables

1 Introduction

Space observatories call for precision attitude control and high pointing accuracy to achieve a quality image (Hubble and James Webb Space Telescopes require 6 milliarcsec and 15 milliarcsec pointing accuracies respectively [2]). A range of emerging science missions (e.g., Asteria [3], Exo-C [4]) and technologies like laser communication [5], precision formation flying, and interferometric sensing, place stringent requirements on spacecraft pointing accuracy and stability. Pointing error is measured relative to an inertial frame (called absolute pointing accuracy) or a reference celestial body (called relative pointing accuracy) [1]. In this thesis, it is assumed that there is no relative motion between the inertial frame and the reference celestial body (often the body of interest); the absolute and relative error are the same. Pointing error can be divided into a steady state DC (drift) component and an AC (jitter) component [6]. The DC component is driven by the need to keep the object of interest within the field of view of the scientific instrument, whereas pointing stability is defined for a particular frequency of AC component, i.e., angular variation of the pointing direction over the exposure time of the scientific instrument. For a detailed account on pointing accuracy and stability see Refs. [1, 6].

The state-of-the-art control architecture for achieving high pointing accuracy and stability of space observatories involves two stages [1, 4]: instrument pointing, which is achieved using a spacecraft Attitude Control System (ACS), and precision pointing and jitter reduction, which is achieved with a Fast Steering Mirror (FSM) in the payload. This architecture includes: 1) Fine Guidance Sensor (FGS), located on the focal plane of the telescope that provides high-rate pointing measurements that are fed back to the controller, 2) FSM that has high bandwidth due to its small inertia compared to the spacecraft to compensate for the jitter. The control architecture also

involves design decisions such as choosing Earth-trailing orbits, designing spacecraft structures to be as rigid as possible to eliminate control structure interaction i.e., avoiding excitation of structural vibration modes, and passive vibration isolators for Reaction Wheels Actuators (RWAs) to reduce jitter. For a comprehensive review of control architectures for high pointing precision see Refs. [1, 4].

The current technology for attitude control relies primarily on RWAs and thruster-based Reaction Control Systems (RCSs). RWAs have reliability issues [7, 8], and are primary source of jitter. RCSs are limited by the fuel carried on the spacecraft. Consequently, there is a patent need to develop better technology to achieve precision pointing. Traditionally, fraction of the control effort is used to keep the structural deflections small and damp different modes as shown in Fig. 1 and another part of the control effort is used to control the spacecraft as a rigid body [9]. In this thesis, we design a controller exploiting the Control Structure Interaction (CSI) by using the coupled dynamics of satellite hub and flexible solar array. Solar array bending is achieved by strain-actuation to perform trajectory tracking and slewing maneuvers. The maximum attitude rotation that can be achieved by bending the solar array is constrained by the maximum stress that can be applied to the solar array without compromising its structural integrity (also, within the elastic limit of the solar array). In Ref. [10], a preliminary analysis of Strain-Actuated Solar Array (SASA) technology was conducted by modelling the solar array as pseudo rigid body dynamic model, where the infinite-dimensional system is modelled as a finite-Degree of Freedom (DOF) system. As a consequence, this model is prone to spillover [11] as high frequency modes of the flexible appendage are not modelled. A preliminary investigation on using SASA technology to replace RWA assemblies with solar arrays of large inertia to achieve spacecraft slewing, attitude control, and momentum management was studied in Ref. [12]. Considering the critical nature

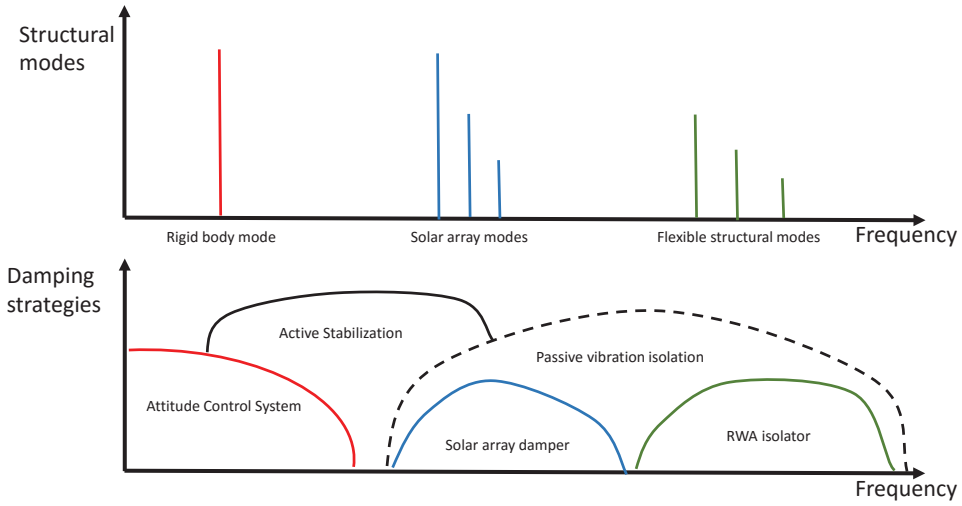

Figure 1: Structural modes and damping strategies used for attitude control taken from [1].

of the application, a simultaneous co-design of both the control architecture and structural design was conducted, and results are presented in Refs. [13, 14]. Here, we develop an accurate representation of the dynamics and distributed control design for attitude control.

In this thesis, we present a nonlinear ODE-PDE dynamical model for the 1-DOF rotation of the spacecraft with flexible appendages and two nonlinear ODE-PDE distributed controllers to achieve attitude control of the spacecraft. The combined finite and infinite-dimensional dynamics are modeled using an ODE-PDE system. The infinite-dimensional nature of the flexible appendage is modelled using Euler-Bernoulli beam theory [15, 16], which gives rise to a fourth-order PDE with boundary conditions given by the fixed root and free end of the solar array. The linear model for a circular hub with flexible appendages, Ref. [17], is extended by taking into consideration axial stiffness in the beam due to rotation and gyroscopic terms. The dynamics of the system is coupled, nonlinear and under-actuated in nature [18, 19]. This is because there is no actuator to control the rigid body rotation of the bus

directly. We exploit the structure in the dynamics and the kinetic symmetry [20] in the system to design the nonlinear controllers, which actuate the flexible beam to achieve satellite slewing using coupled nonlinear dynamics. Given a slewing trajectory, the controllers compute the flexible dynamics required to achieve the trajectory and give an appropriate command to the strain-actuators to bend the beam. The control laws are designed in terms of a variable 'δ', it is shown that the closed-loop system is stable for a range of values of 'δ'. The stability of the closed-loop system is proved for $\delta = 1$ using the Lyapunov direct method (See Ref. [21] for application of the Lyapunov direct method to prove the stability of infinite-dimensional systems). It is observed that the closed-loop system with $\delta = 1$ is Input-to-State Stable [22], which is used to define a range of 'δ' values for which the closed-loop system is stable. The infinite-dimensional ODE-PDE system was discretized using Galerkin method [15–17, 23] to form an ODE system. Galerkin functions were chosen based on the recommendations from Ref. [17].

The control law along with the dynamics is simulated numerically using MATLAB® and Simulink® for trajectory tracking and slewing. Here, we choose four Galerkin functions for discretization, which describe the dynamics of the flexible solar array. An experimental setup was built to test the ODE-PDE control law in real-time for slewing and tracking a sinusoidal trajectory. The test setup has a cylinder with beams symmetric about the axis of rotation. The term slewing in this paper means rotating to a given attitude from initial attitude and maintaining that attitude. The strain actuation in the beams is achieved by bonding piezoelectric (PZT) actuators asymmetrically about the axis of the cylinder. PZT actuators undergo uniform strain when an electric field is applied across them [24]. Due to their properties, PZT find applications in design of intelligent structures, active vibration control, and strain-actuated beams [11, 25–29]. The PZTs can be bonded to the surface of solar array or embedded

within the solar array substructure it for actuation [26,30]. References [26,30] discuss actuator models for SASA configurations described above, with and without perfect bonding. We present a quasi-static actuator model for the surface bonded PZT taken from [31], but corrected for the errors in the final model and validated experimentally using a cantilever beam setup. The actuator model can be extended to a distributed actuation configuration with multiple PZTs, using step functions.

The thesis is organized as follows. The kinematics and dynamics of the system, along with the actuator model of the composite beam (PZT and beam), are discussed in Chapter 2. Nonlinear ODE-PDE control law design and the stability proof using the Lyapunov direct method and Input-to-State Stability property are presented in Chapter 3. In Chapter 4, we derive the Galerkin implementation of the closed-loop system. We discuss the numerical implementation and results for trajectory tracking and slewing in Chapter 5. In Chapter 6, we present the experimental results to validate the actuator model and real-time trajectory tracking of the bus rotation. The results are enumerated in Chapter 7.

1.1 Piezoelectric Material (Background)

This section is taken from Refs. [28,32] and is added here for completeness. Piezoelectric phenomenon means electricity generated when pressure is applied on the surface. Materials which have this property are called piezoelectric materials (PZT), and can be used as a sensor or actuator (using the inverse piezoelectric phenomenon). PZT's are made from a ceramic powder of component metal oxides. The ceramic powder is formed into specific shapes and heated to a specific temperature to form a dense crystalline structure. The heated ceramic crystal below a critical temperature, called Curie temperature, has multiple domains with an associated dipole moment. The

dipole moments align when a high electric field is applied across the crystal, creating a net polarization in the material. This process is called poling. The aligned dipole moments are locked in this configuration even after the electric field is removed. When used as an actuator' piezoelectric material extends when voltage of same polarity as the poling voltage is applied across it. For further discussion on poled materials see Ref. [28].

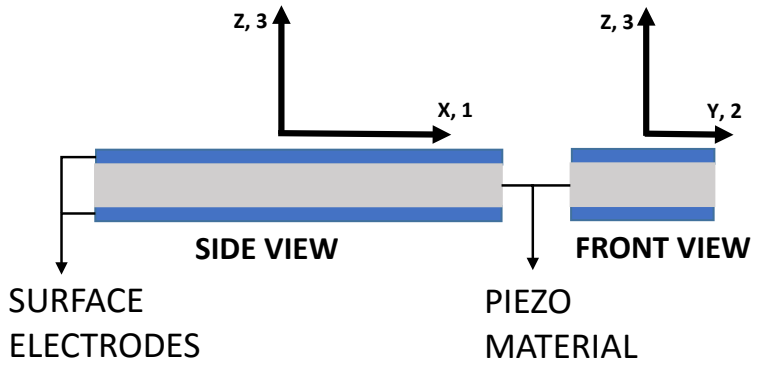

Figure 2: Piezoelectric actuator side and front view.

Here, we describe the linear constitute equations of the PZTs according to IEEE standard. References [28, 32] outline the relationship between strain and the applied electric field when used as an actuator. Figure 2 shows the piezoelectric material bonded with surface electrodes, on which wires are soldered to apply a potential difference. The axis definitions are numbered 1, 2, 3. It is assumed here that there is no mechanical stress on the PZT and it is poled only in direction 3. The strain in the piezo (ϵ) is only due to the applied electric field (E_f) (see Eq. (1)).

$$\epsilon = DE_f \tag{1}$$

$$\begin{bmatrix} \epsilon_1 \\ \epsilon_2 \\ \epsilon_3 \end{bmatrix} = \begin{bmatrix} d_{11} & d_{21} & d_{31} \\ d_{12} & d_{22} & d_{32} \\ d_{13} & d_{23} & d_{33} \end{bmatrix} \begin{bmatrix} E_1 \\ E_2 \\ E_3 \end{bmatrix} \tag{2}$$

$$D = \begin{bmatrix} 0 & 0 & d_{31} \\ 0 & 0 & d_{32} \\ 0 & 0 & d_{33} \end{bmatrix} \tag{3}$$

$$E_3 = \frac{V}{t} \tag{4}$$

$$\epsilon_1 = d_{31} \frac{V}{t} \tag{5}$$

The symbol 'ϵ_i' corresponds to the axial strain, and 'E_i' is the electric field applied in 'i'th direction. 'D' is the matrix of piezoelectric strain constants. Most piezo materials are transversely isotropic , allowing a simplified 'D' matrix representation as shown in Eq. (3). The coefficient 'd_{ij}' is the ratio of strain produced in 'j'th direction due to the electric field applied in 'i'th direction with all external mechanical and thermal stresses held constant. If the thickness of the piezo material is 't' and voltage applied 'V', the strain is given by Eq. (5). Note that due to the above assumptions, we only consider the effect of 'd_{31}' (Eq. (5)) in the final model, which is used in the following Chapters.

2 Kinematics and Dynamics of a 1-DOF Satellite with SASA

The spacecraft with asymmetric SASAs is modeled as a cylinder with flexible appendages that are fixed symmetrically to the rotational axis of the cylinder as shown in Fig. 3. The dynamics of the system include planar rotation of the spacecraft hub, and bending in the flexible composite beam due to strain-actuation. Our modelling approach uses explicit generalization of Lagrange's equations discussed in Ref. [17]. The equations of motion of the ODE-PDE system can also be derived by following the approach discussed in Ref. [33, 34]. Before proceeding to the derivation of the ODE-PDE, we briefly discuss system kinematics of the system, physical properties of the composite beam, and the actuator model for strain-actuation using PZTs.

2.1 Kinematics

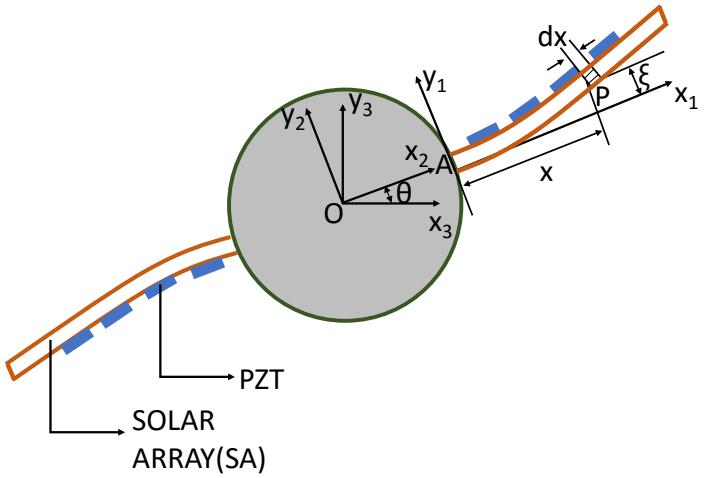

Figure 3: 1-DOF cylinder and flexible solar array model.

The spacecraft body is modeled as a cylinder of radius 'r', and the solar array is modeled as a composite beam with PZT actuators bonded to the surface of a beam with length 'ℓ'. It is assumed that the beam does not undergo any longitudinal vibration. The coordinate systems used in the derivation of kinematics are shown in Fig. 3. In the (x_1, y_1) coordinate system, the location of a point 'P' an element 'dx' on the beam is given by $R_{P/A} = [x, \xi]$ where $\xi(x,t) : (0,\ell) \times \mathbb{R}^+ \to \mathbb{R}$ is the displacement due to bending in y_1 direction. The spacecraft body rotation angle about origin 'O' is '$\theta(t)$', where $\theta(t) : \mathbb{R}^+ \to [-\pi, \pi]$. The position and velocity of 'P' with respect to origin of the spacecraft 'O' are given by Eq. (6) and Eq. (7), respectively. These equations are used to compute 'ξ' and 'x' using 'x_3' and 'y_3' obtained from the Vicon motion tracking system during real time experiments.

$$\begin{bmatrix} x_3 \\ y_3 \end{bmatrix} = \begin{bmatrix} \cos(\theta) & -\sin(\theta) \\ \sin(\theta) & \cos(\theta) \end{bmatrix} \begin{bmatrix} r + x \\ \xi \end{bmatrix} \tag{6}$$

The velocity kinematics are given by:

$$\begin{bmatrix} \dot{x}_3 \\ \dot{y}_3 \end{bmatrix} = \begin{bmatrix} -\sin(\theta) & -\cos(\theta) \\ \cos(\theta) & -\sin(\theta) \end{bmatrix} \begin{bmatrix} (r + x)\dot{\theta} + \dot{\xi} \\ \xi\dot{\theta} \end{bmatrix} \tag{7}$$

2.2 Mass Per Unit Length and Total Rigidity of the Composite Beam

The physical properties of the solar array, such as mass per unit length and location of the neutral axis, play an important role in the evolution of the system dynamics, are functions of the spatial variable 'x' due to the composite nature of the beam. The mass per unit length of the composite beam is given in Eq. (8). Here 'ρ_b' and 'ρ_p'

are the densities of the beam and the PZT, respectively. 'A_b' and 'A_p' are the cross sectional areas of the beam and the PZT, respectively. 'E_b', 'I_b', 't_b', 'E_p', 'I_p', and 't_p' are the Young's modulus, area moment of inertia about neutral axis, and thickness of the beam and PZT, respectively. The function $k\,(x) = 1$ at the locations where the PZT is bonded, and $k\,(x) = 0$ otherwise. For simulations and experiments conducted we use mass per unit length as in Eq. (9), which takes into account the effect of Vicon. The symbol 'm_v' is Vicon marker mass, 'δ_d' is the Dirac delta function, 'ℓ_{v_i}' is the distance to the 'i'th point mass (Vicon marker) on the beam from the root, and 'n'_v is the number of point masses (Vicon markers).

$$m_R = m_b + k\,(x)\,m_p,\ \ m_b = \rho_b A_b,\ \ m_p = \rho_p A_p \tag{8}$$

$$m_R = m_b + k\,(x)\,m_p + \sum_{i=1}^{n_v} m_v \delta_d(x - \ell_{v_i}) \tag{9}$$

The physical, structural, and geometric properties of the PZT and beam; as a result the neutral axis of the composite beam is offset from the geometric centroid. The distance between the top surface of the composite beam to the neutral axis 'h_n' is given in Eq. (10). See Fig. 4 for definition of 'h_n'.

$$h_n = \frac{E_p t_p^2 + E_b t_b\,(t_b + 2t_p)}{2\,(E_p t_p + E_b t_b)} \tag{10}$$

The total rigidity of the beam EI, with area moment of inertia about the new neutral axis is given by EI_t in Eq. (11) at the locations where PZT's are bonded.

$$
\begin{aligned}
EI_t &= E_b I_b + E_p I_p \\
I_b &= \frac{wt_b^3}{12} + wt_b \left(t_p + \frac{t_b}{2} - h_n \right)^2 \\
I_p &= \frac{wt_p^3}{12} + wt_p \left(h_n - \frac{t_p}{2} \right)^2
\end{aligned}
\tag{11}
$$

The total rigidity of the beam at locations with $k(x) = 0$ is given by 'EI_b' in Eq. (12).

$$
EI_b = \frac{E_b w t_b^3}{12} \tag{12}
$$

2.3 Actuator Model

Piezoelectric materials undergo an approximately uniform strain when a potential difference is applied across them. This property is used to achieve actuation of the beam by bonding PZT to its surface or by embedding it inside the beam. The actuator model gives the mathematical frame work for the response (internal moments) of the beam due to a voltage 'V' applied across the PZT bonded on the surface of the beam. It is assumed that the bonding between the PZT and beam is perfect and the composite beam is of constant width 'w'. Since the PZT is bonded only on the top surface, the strain distribution 'ϵ' along the cross section of the composite beam is assumed to be linear. In Eq. (13), 'κ' is the slope of the strain distribution due to bending and 'ϵ_0' corresponds to the extension of the beam due to the offset of the neutral axis. The PZT bonded to the surface of the beam and strain distribution along the cross section of the composite beam can be seen in Fig. 4. The following derivation is taken from Ref. [28], but the final model given in the reference has errors, so it is repeated here with corrections. The force and moment equilibrium are used

to calculate the values of 'κ' and 'ϵ_0'. The static model derived here is used in the dynamic model, assuming that the process is quasi-static in nature.

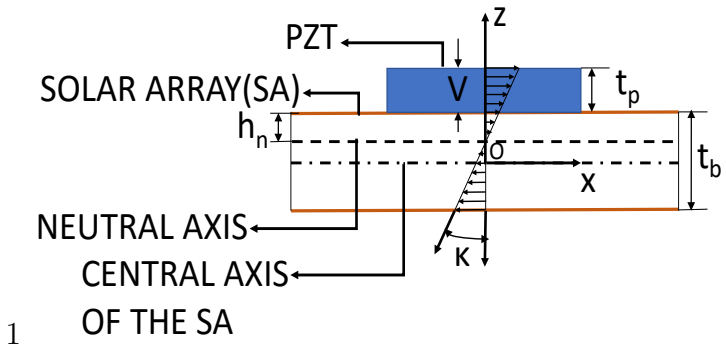

Figure 4: Strain distribution.

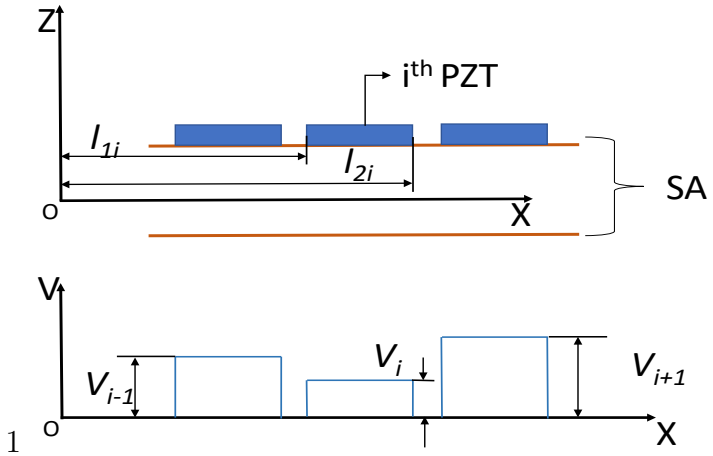

Figure 5: Distributed Piezo.

$$\epsilon = \alpha z + \epsilon_0 \tag{13}$$

In the following analysis, 'ϵ_p' is the strain of an unconstrained PZT when a voltage 'V' is applied across it. This strain is given by $\epsilon_p = \frac{d_{31}V}{t_p}$ (Ref. [28]). The piezoelectric coefficient 'd_{31}' is the ratio of strain in direction 1 when an electric field applied across PZT in direction 3. The stresses in the piezo (σ_p) and beam (σ_b), respectively, are

given in Eq. (14).

$$\begin{aligned}\sigma_p &= E_p(\kappa z + \epsilon_0 - \epsilon_p)\\ \sigma_b &= E_b(\kappa z + \epsilon_0)\end{aligned} \tag{14}$$

The force equilibrium equation is:

$$\int_{-t_b/2}^{t_b/2} \sigma_b(z)dz + \int_{t_b/2}^{t_b/2+t_p} \sigma_p(z)dz = 0 \tag{15}$$

The moment equilibrium equation is:

$$\int_{-t_b/2}^{t_b/2} \sigma_b(z)zdz + \int_{t_b/2}^{t_b/2+t_p} \sigma_p(z)zdz = 0 \tag{16}$$

Substituting the stress distributions in the above equilibrium equations we get:

$$\kappa\left(\frac{E_p\left(t_p t_b + t_p^2\right)}{2}\right) + \epsilon_0\left(E_b t_b + E_b t_b\right) - E_p\epsilon_p t_p = 0 \tag{17}$$

$$\begin{aligned}&\kappa\left(\frac{E_p}{3}\left(\left(t_p + \frac{t_b}{2}\right)^3 - \left(\frac{t_b}{2}\right)^3\right) + \frac{E_b t_b^3}{12}\right) + \epsilon_0\left(\frac{E_p\left(t_p t_b + t_p^2\right)}{2}\right)\\ &- \frac{E_p E_b\left(t_p t_b + t_p^2\right)}{2} = 0\end{aligned} \tag{18}$$

Solving the above two equations we can obtain expressions for 'κ' and 'ϵ_0'

$$\kappa = \frac{6E_b E_p \epsilon_p t_b t_p (t_b + t_p)}{E_b^2 t_b^4 + 4E_b E_p t_b^3 t_p + 6E_b E_p t_b^2 t_p^2 + 4E_b E_p t_b t_p^3 + E_p^2 t_p^4} \tag{19}$$

$$\epsilon_0 = \frac{\epsilon_p E_p t_p (E_p t_p^3 + E_b t_b^3)}{E_b^2 t_b^4 + 4E_b E_p t_b^3 t_p + 6E_b E_p t_b^2 t_p^2 + 4E_b E_p t_b t_p^3 + E_p^2 t_p^4} \tag{20}$$

The moment in the beam, due to the uniform PZT strain produced by the applied

voltage V is given by Eqs. (21) and (22).

$$\begin{aligned} M_b &= E_b I_b \kappa \\ &= \frac{6E_b^2 I_b E_p d_{31} V t_b (t_b + t_p)}{E_b^2 t_b^4 + 4E_b E_p t_b^3 t_p + 6E_b E_p t_b^2 t_p^2 + 4E_b E_p t_b t_p^3 + E_p^2 t_p^4} \end{aligned} \tag{21}$$

$$\begin{aligned} M_b &= cV \\ c &= \frac{6E_b^2 I_b E_p d_{31} t_b (t_b + t_p)}{E_b^2 t_b^4 + 4E_b E_p t_b^3 t_p + 6E_b E_p t_b^2 t_p^2 + 4E_b E_p t_b t_p^3 + E_p^2 t_p^4} \end{aligned} \tag{22}$$

The moment is proportional to the voltage applied across the PZT. The constant 'c' depends on the geometric parameters, structural properties of PZT, and the elastic modulus of the composite beam. The actuator model is extended to a scenario with multiple PZT's using step functions (see Fig. 5). The model with 'n' PZT's on the surface of the beam is given in Eq. (23), where 'V_i' is the voltage applied across 'i'th PZT, 'c_i' is the proportionality constant corresponding to the structural and geometric properties of the 'i'th PZT, and $u\,(x)$ is the step function with unit amplitude. 'l_{1i}' and 'l_{2i}' are defined for 'i'th PZT as shown in Fig. 5.

$$M_b = \sum_{i=1}^{n} c_i V_i \left(u(x - l_{1i}) - u(x - l_{1i})\right) \tag{23}$$

The Eqs. (21) and (23) are used to compute voltage signals required to achieve attitude control from control signal in the simulations and experiments.

2.4 Dynamics

The dynamics of the system include the bending of the composite beam, which is modeled using Euler-Bernoulli beam theory, and slewing of the satellite, which is planar rigid body rotation of the spacecraft. The dynamics of the rigid body and

flexible beam evolves based on the ODE-PDE system with fixed root and free end boundary conditions, forming a hybrid coordinate system with one rigid body and an infinite-dimensional system (also called as distributed parameter system). See Ref. [17] for a discussion of this type of hybrid system, which is distinct from hybrid dynamic systems that combine discrete and continuous dynamics. In deriving the model, we assume that the deflections due to bending are small and that the beam has no longitudinal vibration; the effect of 'ϵ_0' in Eq. (20) is assumed to be negligible. The state of the system corresponding to beam deflection is '$\xi(x,t)$', described by a continuous function of space 'x' and time 't'.

2.4.1 Euler-Lagrange Equations

The Lagrangian of the system, with mass moment of inertia of the spacecraft bus (cylinder) — 'J_θ', includes rotational kinetic energy of the spacecraft body —'T_s' (defined in Eq. (24)), kinetic energy of the beams assuming asymmetric strain-actuation — 'T_b' (defined in Eq. (25)), elastic potential energy and axial stiffening of the beams due to centrifugal force from bus rotation —'U' (defined in Eq. (26)). For derivation of equations of motion for a linear hybrid coordinate systems using a system's Lagrangian, see Ref. [17].

$$T_s = \frac{1}{2} J_\theta \dot{\theta}^2 \tag{24}$$

$$\begin{aligned} T_b &= \int_0^\ell m_R \left(\dot{x}_3^2 + \dot{y}_3^2\right) dx \\ &= \int_0^\ell m_R \Big[\dot{\theta}^2(r^2 + x^2 + \xi^2) + \dot{\xi}^2 + 2r\dot{\xi}\dot{\theta} + 2r\dot{\theta}^2 x + 2\dot{\xi}\dot{\theta}x\Big] dx \end{aligned} \tag{25}$$

$$U = \int_0^\ell \left[EI\left(\xi''\right)^2\right] dx + \int_0^\ell \left[P\left(\dot{\theta}, x\right)\left(\xi'\right)^2\right] dx \tag{26}$$

where $()' = \frac{\partial}{\partial x}()$, and $P\left(\dot{\theta}, x\right) = \int_{r+x}^{r+\ell} \left[m_R \dot{\theta}^2 s\right] ds = p(x)\dot{\theta}^2$ is the axial tension in the beam due to rotation, where 'm_R' is expressed as a function of 's', and $s = r + x$. The definition of total rigidity 'EI' of the composite beam is given in Section. 2.2. The Lagragian of the ODE-PDE system in terms of state variables is given in Eq. **??**

$$L = T_s + T_b - U \tag{27a}$$

$$= \frac{1}{2} J_\theta \dot{\theta}^2 + \int_0^\ell m_R \Big[\dot{\theta}^2 \left(r^2 + x^2 + \xi^2\right) + \dot{\xi}^2 + 2r\dot{\xi}\dot{\theta} + 2r\dot{\theta}^2 x + 2\dot{\xi}\dot{\theta}x\Big] dx$$
$$- \int_0^\ell \left[(EI\left(\xi''\right)^2\right] dx - \int_0^\ell P(\dot{\theta}, x)\left(\xi'\right)^2 dx \tag{27b}$$

The nonconservative work done 'W_{nc}' due to moment applied by strain actuation is given by Eq. (28). Here '$M_b(x,t)$' is the response of the beam (see Eq. (22)) due to the strain produced by the bonded piezo. The equations of motion are obtained by using the explicit generalization of Lagrange's equations for infinite-dimensional systems approach (see Ref. [17] for more details). The extended Hamilton's principle can be stated as, in Eq. (29), where 't_0' and 't_f' are the initial and final time values, respectively.

$$W_{nc} = \int_0^\ell \frac{M_b(x,t)^2}{E_b I_b} dx \tag{28}$$

$$\int_{t_0}^{t_f} (\delta L + \delta W_{nc})\, dt = 0 \tag{29}$$

Applying integration by parts to the expanded variations in terms of state variables, and using boundary conditions, we obtain the equations of motion in terms of Lagrangian as given in Eqs. (30) and (31).

$$\frac{d}{dt}\left(\frac{\partial L}{\partial \dot{\xi}}\right) - \frac{\partial L}{\partial \xi} + \frac{\partial}{\partial x}\left(\frac{\partial L}{\partial \xi'}\right) - \frac{\partial^2}{\partial x^2}\left(\frac{\partial L}{\partial \xi''}\right) = \frac{\partial^2}{\partial x^2}\left(M_b(x,t)\right) \tag{30}$$

$$\frac{d}{dt}\left(\frac{\partial L}{\partial \dot{\theta}}\right) - \frac{\partial L}{\partial \theta} = 0 \tag{31}$$

The structural damping in the system is modeled using Kelvin-Voigt constant 'μ'. The equations of motion after substituting the Lagrangian are:

$$\begin{aligned}\left(\frac{1}{2}J_\theta + \int_0^\ell \left(m_R\left((x+r)^2+\xi^2\right) - p(x)\xi'^2\right)dx\right)\ddot{\theta} + \int_0^\ell m_R\left(r+x\right)\ddot{\xi}dx \\ + \int_0^\ell 2m_R\xi\dot{\xi}\dot{\theta}dx - \int_0^\ell 2\dot{\theta}p(x)\xi'\dot{\xi}'dx = 0\end{aligned} \tag{32a}$$

$$m_R\left(r+x\right)\ddot{\theta} + m_R\ddot{\xi} - m_R\dot{\theta}^2\xi - \left(\dot{\theta}^2 p(x)\xi'\right)' + \left(EI\xi'' + \mu EI\dot{\xi}''\right)'' = \left(M_b(x,t)\right)'' \tag{32b}$$

The boundary conditions for the beam are due to fixed root and free end:

$$\begin{aligned}\xi(x,t)|_{x=0} = \xi'(x,t)\Big|_{x=0} = 0, \\ (EI\xi'' + \mu EI\dot{\xi}'')\Big|_{x=\ell} = 0, \quad (EI\xi'' + \mu EI\dot{\xi}'')'\Big|_{x=\ell} = 0\end{aligned} \tag{33}$$

2.4.2 Matrix Form of Euler-Lagrangian System

$$\int_0^\ell M_s \begin{bmatrix}\ddot{\theta}\\ \ddot{\xi}\end{bmatrix} dx + \int_0^\ell C_s \begin{bmatrix}\dot{\theta}\\ \dot{\xi}\end{bmatrix} dx + \begin{bmatrix}0\\ S_s\end{bmatrix} = \begin{bmatrix}0\\ 2\int_0^\ell (M_b(x,t))''dx\end{bmatrix} \tag{34}$$

$$
\begin{aligned}
M_s &= \begin{bmatrix} m_{11}(\xi) & m_{12} \\ m_{12} & m_{22} \end{bmatrix} \\
&= \begin{bmatrix} \left(J_\theta/\ell + 2\left(m_R\left((x+r)^2+\xi^2\right) - p(x)\xi'^2\right)\right) & 2m_R\left(x+r\right) \\ 2m_R\left(x+r\right) & 2m_R \end{bmatrix} \\
S_s &= 2\int_0^\ell \left(EI\xi'' + \mu EI\dot{\xi}''\right)'' dx \qquad (35) \\
C_s &= \begin{bmatrix} c_{11}(\xi,\dot{\xi}) & c_{12}(\xi,\dot{\theta}) \\ -c_{12}(\xi,\dot{\theta}) & 0 \end{bmatrix} \\
&= \begin{bmatrix} 2\left(m_R\xi\dot{\xi} - p(x)\xi'\dot{\xi}'\right) & 2\left(m_R\xi\dot{\theta} + (p(x)\xi')'\dot{\theta}\right) \\ -2\left(m_R\xi\dot{\theta} + (p(x)\xi')'\dot{\theta}\right) & 0 \end{bmatrix}
\end{aligned}
$$

Equations (32a) and (32b) are expressed in standard Euler-Lagrangian matrix form in Eq. (34), with matrices 'M_s' and 'C_s' defined in Eq. (35). The boundary conditions still apply.

3 Nonlinear ODE-PDE Control Design of SASA

3.1 Properties of the Underactuated Hybrid System

The dynamics in Eq. (34) possesses kinetic symmetry [20] with respect to the spacecraft attitude, 'θ', since the inertia matrix per unit length is independent of 'θ'. The kinetic symmetry with respect to 'θ' in the absence of gravitational effects leads to symmetry in mechanics satisfying Eq. 3.1.

$$\frac{\partial K}{\partial \theta} = \frac{\partial L}{\partial \theta} = 0 \tag{36}$$

since the corresponding Lagrangian 'L' is independent of 'θ'. Note that the first generalized angular momentum for the variable 'θ', which is denoted by 'z_1' is given in Eq. 3.1.

$$z_1 = \frac{\partial L}{\partial \dot{\theta}} = \int_0^\ell (m_{11}\dot{\theta} + m_{12}\dot{\xi})dx, \qquad \dot{z}_1 = \frac{d}{dt}\frac{\partial L}{\partial \dot{\theta}} = \frac{\partial L}{\partial \theta} = 0 \tag{37}$$

We can verify that $c_{11} = \frac{\dot{m}_{11}}{2}$ and $\int_0^\ell \left(\dot{M}_s - \left(C_s + C_s^T\right)\right) dx$ is skew-symmetric, which is exploited in the control design.

3.2 NonLinear ODE-PDE Control Law

In this section, we present nonlinear ODE-PDE control laws designed using the properties discussed in Section. 3.1 for trajectory tracking. In order to track a desired rotation signal 'θ_d', with angular speed '$\dot{\theta}_d$', and angular acceleration '$\ddot{\theta}_d$', a reference rotation signal Eq. (38a), (38b) is computed using the desired signal to use in the control law. The reference signal 'θ_r' converges exponentially to desired signal 'θ_d'

with the convergence rate depending on the gain value 'λ_θ'.

$$\dot{\theta}_r(t) = \dot{\theta}_d(t) - \lambda_\theta(\theta - \theta_d(t)) \tag{38a}$$

$$\ddot{\theta}_r(t) = \ddot{\theta}_d(t) - \lambda_\theta(\dot{\theta} - \dot{\theta}_d(t)) \tag{38b}$$

The reference rotation signal 'θ_r' is used to compute reference deflection signal 'ξ_r' using Eq. (39), which is the 'θ' dynamics for the reference signal 'θ_r' augmented with the error feedback term $K_\theta\left(\dot{\theta} - \dot{\theta}_r\right)$, where '$K_\theta$' is gain.

$$m_{12}\ddot{\xi}_r + m_{11}\ddot{\theta}_r + c_{11}\dot{\theta}_r + c_{12}\dot{\xi}_r = K_\theta(\dot{\theta} - \dot{\theta}_r) \tag{39}$$

Using Eqs. (38a), (38b), (39) and variables $s_\theta = \dot{\theta} - \dot{\theta}_r$ and $s_\xi = \dot{\xi} - \dot{\xi}_r$, we can design control laws to achieve trajectory tracking and slewing as described in the following sections.

3.2.1 Controller 1

Let $\tau = (M_b(x,t))''$. The control effort τ is computed using Eq. (40). The closed-loop system with this controller is given in Eq. (41), where 'δ' is a constant and 'K_ξ' is gain.

$$\tau = m_{12}\ddot{\theta}_r + m_{22}\ddot{\xi}_r + c_{12}\dot{\theta}_r + 2\left(\delta EI\xi'' + \mu EI\delta\dot{\xi}''\right)'' - K_\xi s_\xi \tag{40}$$

$$\begin{aligned}&\int_0^\ell \left(M_s \begin{bmatrix} \dot{s}_\theta \\ \dot{s}_\xi \end{bmatrix} + C_s \begin{bmatrix} s_\theta \\ s_\xi \end{bmatrix} + \begin{bmatrix} 0 \\ (1-\delta)\left(2EI\xi'' + \mu 2EI\dot{\xi}''\right)'' \end{bmatrix} \right) dx \\ &+ \int_0^\ell \left(\begin{bmatrix} K_\theta & 0 \\ 0 & K_\xi \end{bmatrix} \begin{bmatrix} s_\theta \\ s_\xi \end{bmatrix} \right) dx = \begin{bmatrix} 0 \\ 0 \end{bmatrix}\end{aligned} \tag{41}$$

Before proving the stability of the closed-loop system in Eq. (41), we will prove stability for a special case with $\delta = 1$. The closed-loop system with $\delta = 1$ is given in Eq. (42). The Input-to-State Stability [22] of this special case is used to define a range for 'δ' which stabilize the closed-loop system Eq. (41).

Lemma 3.1. *The closed-loop system with dynamics Eq. (34), control law Eqs. (38a-40), in Eq. (42) is globally asymptotically stable.*

$$\int_0^\ell M_s \begin{bmatrix} \dot{s}_\theta \\ \dot{s}_\xi \end{bmatrix} dx + \int_0^\ell C_s \begin{bmatrix} s_\theta \\ s_\xi \end{bmatrix} dx + \int_0^\ell \begin{bmatrix} K_\theta & 0 \\ 0 & K_\xi \end{bmatrix} \begin{bmatrix} s_\theta \\ s_\xi \end{bmatrix} dx = \begin{bmatrix} 0 \\ 0 \end{bmatrix}, \tag{42}$$

Proof. We use the Lyapunov direct method [21] to prove the stability of the closed-loop system, which ensures trajectory tracking. The Lyapunov function in Eq. (43) is positive definite as 'M_s' is the mass matrix in the open loop dynamics.

$$V_{L_1} = \int_0^\ell \frac{1}{2} \begin{bmatrix} s_\theta \\ s_\xi \end{bmatrix}^T \begin{bmatrix} m_{11}(\xi) & m_{12} \\ m_{12} & m_{22} \end{bmatrix} \begin{bmatrix} s_\theta \\ s_\xi \end{bmatrix} dx \tag{43}$$

$$\dot{V}_{L_1} = \int_0^\ell \begin{bmatrix} s_\theta \\ s_\xi \end{bmatrix}^T \begin{bmatrix} m_{11}(\xi) & m_{12} \\ m_{12} & m_{22} \end{bmatrix} \begin{bmatrix} \dot{s}_\theta \\ \dot{s}_\xi \end{bmatrix} dx + \int_0^\ell \frac{1}{2} \begin{bmatrix} s_\theta \\ s_\xi \end{bmatrix}^T \begin{bmatrix} \dot{m}_{11}(\xi) & 0 \\ 0 & 0 \end{bmatrix} \begin{bmatrix} s_\theta \\ s_\xi \end{bmatrix} dx \tag{44}$$

Using the equations of motion, and dynamic properties, the derivative of the Lyapunov function can be simplified to Eq. (45).

$$\dot{V}_{L_1} = \int_0^\ell \begin{bmatrix} s_\theta \\ s_\xi \end{bmatrix}^T \begin{bmatrix} -K_\theta & 0 \\ 0 & -K_\xi \end{bmatrix} \begin{bmatrix} s_\theta \\ s_\xi \end{bmatrix} dx \tag{45}$$

The Lyapunov derivative $\dot{V}_{L_1}$ is negative definite provided that the gain values K_θ and K_ξ are chosen to be positive. By the Lyapunov direct method, the closed-loop

system is globally asymptotically stable. Therefore $s_\theta \to 0$ and $s_\xi \to 0$, implying $\dot{\theta} \to \dot{\theta}_r$ and $\dot{\xi} \to \dot{\xi}_r$. To prove $\theta \to \theta_d$ we need to subtract $\dot{\theta}$ from both sides of Eq. (38a), and use the fact that $\left(\dot{\theta} - \dot{\theta}_r\right) \to 0$ (see Eqs. (46a), (46b)).

$$\dot{\theta}_r(t) - \dot{\theta} = \dot{\theta}_d(t) - \dot{\theta} - \lambda_\theta(\theta - \theta_d(t)) \tag{46a}$$

$$\dot{\theta} - \dot{\theta}_d(t) = -\lambda_\theta(\theta - \theta_d(t)) \tag{46b}$$

Equation (46b) is of the form $\dot{e} = -\lambda e$, where $e = \theta - \theta_d(t)$, which implies $\theta \to \theta_d$ exponentially with a rate of convergence that depends on the constant 'λ_θ'. □

The term $(1-\delta)\left(2EI\xi'' + \mu 2EI\dot{\xi}''\right)''$ describes strain energy and the dissipation modelled in terms of strain rate. Let $d_1 = (1-\delta)\left(2EI\xi'' + \mu 2EI\dot{\xi}''\right)''$; '$d_1$' is bounded because the strain energy should be bounded so as not to compromise the structural integrity of the solar array, to maintain internal stress in the beam with in the elastic limit of the solar array. Let the bound on d_1 be ρ_{d_1}, i.e, $||d_1|| \leq \rho_{d_1}$. Using the Lyapunov function Eq. (43), closed-loop system Eq. (41) the derivative of the Lyapunov function can be simplified to following:

$$\dot{V}_{L_{1_g}} = \int_0^\ell \begin{bmatrix} s_\theta \\ s_\xi \end{bmatrix}^T \begin{bmatrix} m_{11}(\xi) & m_{12} \\ m_{12} & m_{22} \end{bmatrix} \begin{bmatrix} \dot{s}_\theta \\ \dot{s}_\xi \end{bmatrix} dx + \int_0^\ell \frac{1}{2} \begin{bmatrix} s_\theta \\ s_\xi \end{bmatrix}^T \begin{bmatrix} \dot{m}_{11}(\xi) & 0 \\ 0 & 0 \end{bmatrix} \begin{bmatrix} s_\theta \\ s_\xi \end{bmatrix} dx \tag{47a}$$

$$= \int_0^\ell -K_\theta s_\theta^2 dx - \int_0^\ell K_\xi s_\xi^2 dx - \int_0^\ell d_1 \; s_\xi dx \tag{47b}$$

$$\leq \int_0^\ell -K_\theta s_\theta^2 dx - \int_0^\ell K_\xi s_\xi^2 dx + \int_0^\ell ||d_1||\; ||s_\xi|| dx \tag{47c}$$

$$\leq \int_0^\ell -K_\theta s_\theta^2 dx - \int_0^\ell K_\xi ||s_\xi||\; ||s_\xi|| dx + \int_0^\ell ||d_1||\; ||s_\xi|| dx \tag{47d}$$

$$\leq \int_0^\ell -K_\theta s_\theta^2 dx - \int_0^\ell \left(K_\xi ||s_\xi|| - ||d_1||\right) ||s_\xi|| dx \tag{47e}$$

Note that $\dot{V}_{L_{1_g}}$ is negative definite provided that $||d_1|| < K_\xi |||s_\xi||$, which proves that the Lyapunov function is an ISS-Lyapunov function [22]. For trajectory tracking, we need to choose 'K_ξ' and 'δ' to ensure that $||d_1|| < K_\xi |||s_\xi||$. It was observed during the simulations and experiments that the control law works for a range of 'K_ξ' and 'δ' values. This range can be found easily with the help of simulations).

3.2.2 Controller 2

The control objective of trajectory tracking can also be achieved by using the reference deflection signal ξ_r instead of the deflection ξ in the control law. Here we assume that reference signal ξ_r satisfies the same boundary conditions (see Eq. (48)) as the dynamics ξ in Eq. (33). The closed-loop system with the controller Eq. (49) is given in Eq. (50).

$$\begin{aligned} \xi_r(x,t)|_{x=0} = \xi_r^{'}(x,t)\Big|_{x=0} = 0, \\ (EI\xi_r^{''} + \mu EI\dot{\xi}_r^{''})\Big|_{x=\ell} = 0, \quad (EI\xi_r^{''} + \mu EI\dot{\xi}_r^{''})'\Big|_{x=\ell} = 0 \end{aligned} \tag{48}$$

$$\tau = m_{12}\ddot{\theta}_r + m_{22}\ddot{\xi}_r + c_{12}\dot{\theta}_r + \delta\left(2EI\xi_r^{''} + \mu 2EI\dot{\xi}_r^{''}\right)^{''} - K_\xi s_\xi \tag{49}$$

$$\begin{aligned} &\int_0^\ell \left(M_s \begin{bmatrix} \dot{s}_\theta \\ \dot{s}_\xi \end{bmatrix} + C_s \begin{bmatrix} s_\theta \\ s_\xi \end{bmatrix} + \begin{bmatrix} 0 \\ 2\left(EI\left(\xi - \delta\xi_r\right)^{''} + \mu EI(\dot{\xi} - \delta\dot{\xi}_r)^{''}\right)^{''} \end{bmatrix} \right) dx \\ &+ \int_0^\ell \left(\begin{bmatrix} K_\theta & 0 \\ 0 & K_\xi \end{bmatrix} \begin{bmatrix} s_\theta \\ s_\xi \end{bmatrix} \right) dx = \begin{bmatrix} 0 \\ 0 \end{bmatrix} \end{aligned} \tag{50}$$

Similar to the development in Section. 3.2.1 we prove the stability of the closed-loop system in Eq. (50) for $\delta = 1$, and then use the ISS property to define conditions for

which controller in Eq. (49) achieves trajectory tracking.

Lemma 3.2. *The closed-loop system with dynamics Eq. (34), control law Eqs. (38a)-(49), given in Eq. (50) is globally asymptotically stable.*

$$\begin{aligned}\int_0^\ell \left(M_s \begin{bmatrix} \dot{s}_\theta \\ \dot{s}_\xi \end{bmatrix} + C_s \begin{bmatrix} s_\theta \\ s_\xi \end{bmatrix} + \begin{bmatrix} 0 \\ 2\left(EI\left(\xi - \xi_r\right)'' + \mu EI s_\xi''\right)'' \end{bmatrix} \right) dx \\ + \int_0^\ell \left(\begin{bmatrix} K_\theta & 0 \\ 0 & K_\xi \end{bmatrix} \begin{bmatrix} s_\theta \\ s_\xi \end{bmatrix} \right) dx = \begin{bmatrix} 0 \\ 0 \end{bmatrix}\end{aligned} \tag{51}$$

Proof. We need the equalities in Eqs. (52a) and (52b) to prove the stability of Eq. (51), which can be proved by applying integration by parts twice to the left hand side of the equation and using boundary conditions of both the reference signal 'ξ_r' and the dynamics 'ξ'.

$$\int_0^\ell \left(EI\left(\xi - \xi_r\right)''\right)'' \left(\dot{\xi} - \dot{\xi}_r\right) dx = \int_0^\ell EI\left(\xi - \xi_r\right)'' \left(\dot{\xi} - \dot{\xi}_r\right)'' dx \tag{52a}$$

$$\int_0^\ell \left(EI\left(\dot{\xi} - \dot{\xi}_r\right)''\right)'' \left(\dot{\xi} - \dot{\xi}_r\right) dx = \int_0^\ell EI\left(\left(\dot{\xi} - \dot{\xi}_r\right)''\right)^2 dx \tag{52b}$$

Consider the Lyapunov function V_{L_2} in Eq. (53):

$$V_{L_2} = \int_0^\ell \frac{1}{2} \begin{bmatrix} s_\theta \\ s_\xi \end{bmatrix}^T \begin{bmatrix} m_{11}(\xi) & m_{12} \\ m_{12} & m_{22} \end{bmatrix} \begin{bmatrix} s_\theta \\ s_\xi \end{bmatrix} dx + \int_0^\ell \left(EI\left(\xi - \xi_r\right)''\right)^2 dx \tag{53}$$

$$\dot{V}_{L_2} = \int_0^\ell \begin{bmatrix} s_\theta \\ s_\xi \end{bmatrix}^T \begin{bmatrix} m_{11}(\xi) & m_{12} \\ m_{12} & m_{22} \end{bmatrix} \begin{bmatrix} \dot{s}_\theta \\ \dot{s}_\xi \end{bmatrix} dx + \int_0^\ell \frac{1}{2} \begin{bmatrix} s_\theta \\ s_\xi \end{bmatrix}^T \begin{bmatrix} \dot{m}_{11}(\xi) & 0 \\ 0 & 0 \end{bmatrix} \begin{bmatrix} s_\theta \\ s_\xi \end{bmatrix} dx \\ + 2 \int_0^\ell EI \left(\xi - \xi_r\right)'' \left(\dot{\xi} - \dot{\xi}_r\right)'' dx \tag{54}$$

Using the equations of motion, the derivative of the Lyapunov function can be simplified to Eq. (55):

$$\dot{V}_{L_2} = \int_0^\ell \begin{bmatrix} s_\theta \\ s_\xi \end{bmatrix}^T \begin{bmatrix} -K_\theta & 0 \\ 0 & -K_\xi \end{bmatrix} \begin{bmatrix} s_\theta \\ s_\xi \end{bmatrix} dx - 2\mu \int_0^\ell EI \left(\left(\dot{\xi} - \dot{\xi}_r\right)'' \right)^2 dx \tag{55}$$

It can be observed that Eq. (55) is negative definite for positive gains K_θ and K_ξ, and $\mu > 0$. $\theta \to \theta_d$ due to the same argument used for the proof of controller 1. □

Consider the Lyapunov function in Eq. (56), for defining the values of δ for which the closed-loop system in Eq. (50) is stable. Let $d_2 = \left(EI\left(\xi - \delta\xi_r\right)''\right)'' + \left(EI\left(\dot{\xi} - \delta\dot{\xi}_r\right)''\right)''$; '$d_2$' is bounded due to the structural constraints on the system as explained in Section. 3.2.1. As can be seen in the Eq. (57c), if we find 'K_ξ for given 'δ' such that $||d_2|| \leq K_\xi ||s_\xi||$, the closed-loop system in Eq. (50) is stable.

$$V_{L_{2_g}} = \int_0^\ell \begin{bmatrix} s_\theta \\ s_\xi \end{bmatrix}^T \begin{bmatrix} m_{11}(\xi) & m_{12} \\ m_{12} & m_{22} \end{bmatrix} \begin{bmatrix} s_\theta \\ s_\xi \end{bmatrix} dx \tag{56}$$

$$\dot{V}_{L_{2_g}} = \int_0^\ell \begin{bmatrix} s_\theta \\ s_\xi \end{bmatrix}^T \begin{bmatrix} m_{11}(\xi) & m_{12} \\ m_{12} & m_{22} \end{bmatrix} \begin{bmatrix} \dot{s}_\theta \\ \dot{s}_\xi \end{bmatrix} dx + \int_0^\ell \frac{1}{2} \begin{bmatrix} s_\theta \\ s_\xi \end{bmatrix}^T \begin{bmatrix} \dot{m}_{11}(\xi) & 0 \\ 0 & 0 \end{bmatrix} \begin{bmatrix} s_\theta \\ s_\xi \end{bmatrix} dx \tag{57a}$$

$$= \int_0^\ell -K_\theta s_\theta^2 dx - \int_0^\ell K_\xi s_\xi^2 dx - \int_0^\ell d_2 \; s_\xi dx \tag{57b}$$

$$\leq \int_0^\ell -K_\theta s_\theta^2 dx - \int_0^\ell \left(K_\xi ||s_\xi|| - ||d_2||\right) ||s_\xi|| dx \tag{57c}$$

The closed-loop ODE-PDE system for both controller 1 and controller 2 is described in the flow chart Fig. 6.

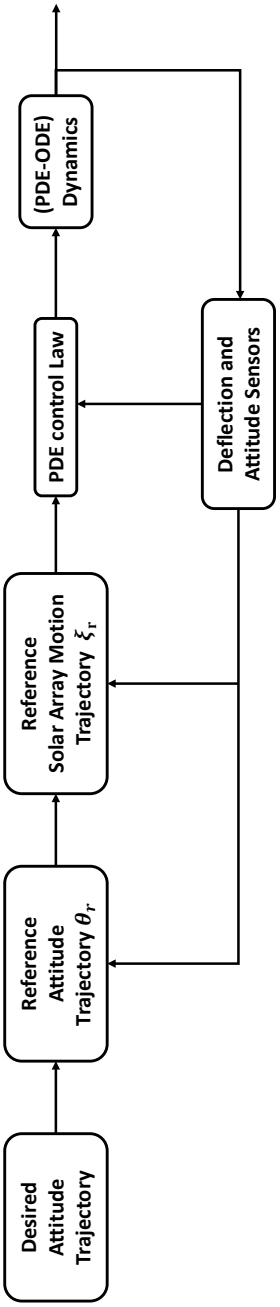

Figure 6: Closed-loop of the ODE-PDE system.

4 Finite Dimensional Approximation of ODE-PDE Dynamics and Control Law

The hybrid ODE-PDE model is discritized to obtain an ODE model using Galerkin method [15, 17] for numerical simulations and experiments. The deflection in the beam is approximated as $\xi(x,t) = \phi^T(x)\eta(t)$, where '$\phi(x)$' are Galerkin functions. The 'j'th Galerkin function $\phi_j(x)$ in Eq. (58) is taken from Ref. [17], and is chosen to satisfy the boundary conditions. The discretization is implemented by minimizing the weighted residual of the 'ξ' dynamics (see Eq. (59)). Here, we use four Galerkin functions ($j = 1, 2, 3, 4$) which sufficiently describe the dynamics for a sinusoidal attitude trajectory and slewing.

$$\phi_j(x) = 1 - \cos\left(\frac{j\pi x}{\ell}\right) + \frac{1}{2}(-1)^{j+1}\left(\frac{j\pi x}{\ell}\right)^2 \tag{58}$$

$$\begin{aligned}&\int_0^\ell \phi\left(m_R\left(r+x\right)\ddot{\theta} + m_R\ddot{\xi} - m_R\dot{\theta}^2\xi - \left(\dot{\theta}^2 p(x)\xi'\right)' + \left(EI\xi'' + \mu EI\dot{\xi}''\right)''\right)dx \\ &- \int_0^\ell \phi M_b''(x,t)dx = 0\end{aligned} \tag{59}$$

4.1 Dynamics in Galerkin Form

The equations of motion in Galerkin form are given in Eq. (60). The matrices $[A]$, $[B]$, $[C]$ are used to define the mass matrix $[M_g]$ and gyroscopic cross coupling terms in matrix $[C_g]$. The matrix $[E]$ corresponds to the stiffness of the beam.

The matrices in Eq. (62) are referred to as Galerkin matrices in this paper.

$$[\boldsymbol{M_g}]\begin{bmatrix}\ddot{\theta}\\ \ddot{\boldsymbol{\eta}}\end{bmatrix}+[\boldsymbol{C_g}]\begin{bmatrix}\dot{\theta}\\ \dot{\boldsymbol{\eta}}\end{bmatrix}+\begin{bmatrix}0\\ 2[\boldsymbol{E}](\boldsymbol{\eta}+\mu\dot{\boldsymbol{\eta}})\end{bmatrix}=\begin{bmatrix}0\\ \int_0^\ell 2\boldsymbol{\phi}M_b^{''}dx\end{bmatrix} \tag{60}$$

$$\begin{aligned}[\boldsymbol{M_g}]&=\begin{bmatrix}m_{11_g} & m_{12_g}\\ m_{21_g} & m_{22_g}\end{bmatrix}=\begin{bmatrix}\left(J_\theta+2\int_0^\ell m_R\left(x+r\right)^2dx+2\boldsymbol{\eta}^T\left([\boldsymbol{A}]-[\boldsymbol{B}]\right)\boldsymbol{\eta}\right) & 2[\boldsymbol{C}]\\ 2[\boldsymbol{C}]^T & 2[\boldsymbol{A}]\end{bmatrix}\\ [\boldsymbol{C_g}]&=\begin{bmatrix}c_{11_g} & c_{12_g}\\ c_{21_g} & c_{22_g}\end{bmatrix}=\begin{bmatrix}2\dot{\boldsymbol{\eta}}^T\left([\boldsymbol{A}]-[\boldsymbol{B}]\right)\boldsymbol{\eta} & 2\boldsymbol{\eta}^T\left([\boldsymbol{A}]-[\boldsymbol{B}]\right)\dot{\theta}\\ -2([\boldsymbol{A}]-[\boldsymbol{B}])\boldsymbol{\eta}\dot{\theta} & 0\end{bmatrix}\end{aligned} \tag{61}$$

$$\begin{aligned}[\boldsymbol{A}]&=\int_0^\ell m_R\boldsymbol{\phi}\boldsymbol{\phi}^Tdx,\quad [\boldsymbol{B}]=\int_0^\ell p\boldsymbol{\phi}^{'}\boldsymbol{\phi}^{'T}dx,\\ [\boldsymbol{C}]&=\int_0^\ell m_R(x+r)\boldsymbol{\phi}^Tdx,\quad [\boldsymbol{E}]=\int_0^\ell \boldsymbol{\phi}(EI\boldsymbol{\phi}^{''T})''dx\end{aligned} \tag{62}$$

4.2 NonLinear Controller in Galerkin Form

The reference signal can be approximated using Galerkin functions, $\xi_r=\phi^T(x)\eta_r(t)$, as 'ξ_r' also satisfies the boundary conditions in Eq. (48). The control laws designed in Section. 3.2 are expressed in Galerkin form as follows:

$$s_\theta=\dot{\theta}-\dot{\theta}_r,\ s_\xi=\phi^T\left(\dot{\eta}-\dot{\eta}_r\right) \tag{63}$$

$$m_{12_g}\ddot{\eta}_r+c_{12_g}\dot{\eta}_r=K_\theta(\dot{\theta}-\dot{\theta}_r)\ell-m_{11_g}\ddot{\theta}_r-c_{11_g}\dot{\theta}_r \tag{64}$$

Controller 1:

$$\int_0^\ell 2\boldsymbol{\phi}M_b^{''}dx=m_{21_g}\ddot{\theta}_r+m_{22_g}\ddot{\eta}_r+c_{21_g}\dot{\theta}_r+2\delta[E](\eta+\mu\dot{\eta})-K_\xi\int_0^\ell\boldsymbol{\phi}\boldsymbol{\phi}^Tdx\left(\dot{\eta}-\dot{\eta}_r\right) \tag{65}$$

Controller 2:

$$\int_0^\ell 2\boldsymbol{\phi} M_b^{''} dx = m_{21_g}\ddot{\theta}_r + m_{22_g}\ddot{\eta}_r + c_{21_g}\dot{\theta}_r + 2\delta[E](\eta_r + \mu\dot{\eta}_r) - K_\xi \int_0^\ell \boldsymbol{\phi}\boldsymbol{\phi}^T dx\,(\dot{\eta} - \dot{\eta}_r) \tag{66}$$

4.3 Computation of Voltage Signal from Control Signal

For actuation, a potential difference is applied across the PZT material, bonded onto the beam. The voltage signal, which is the input to the actuator, is computed from the control signal defined in Eqs. (65) and (66). Consider 'n' discrete PZT actuators bonded onto the solar array (see Fig. 5), where l_{1i} and l_{2i} are distances of two ends of the 'i'th PZT from the root of the solar array. For 'n' PZTs, the moment produced can be modeled as described in Eq. (23), which is used in the following model:

$$\tau = \int_0^\ell \phi M_b^{''} dx \tag{67a}$$

$$= \int_0^\ell \phi \sum_{i=1}^{n} c_i V_i(t) \left(u(x - l_{1i}) - u(x - l_{1i})\right)^{''} dx \tag{67b}$$

$$= \sum_{i=1}^{n} c_i V_i(t) \int_0^\ell \phi \left(u(x - l_{1i}) - u(x - l_{1i})\right)^{''} dx \tag{67c}$$

The function 'u' used in the above equations is a step function, whose derivative is the dirac delta function 'δ_d'. The term $\int_0^\ell \phi \left(u(x - l_{1i}) - u(x - l_{1i})\right)^{''} dx$ can be simplified to $\int_0^\ell -\phi^{'} \left(\delta_d(x - l_{1i}) - \delta_d(x - l_{1i})\right) dx$ using integration by parts. Using the shifting property of the impulse function, we get Eq. (68):

$$\tau = \sum_{i=1}^{n} c_i V_i(t) \left(\phi^{'}(l_{2i}) - \phi^{'}(l_{1i})\right) \tag{68}$$

With two PZT actuators on the beam, the voltage signal is computed using Eq. (68) as follows:

$$\begin{bmatrix} \phi_1'(l_{21}) - \phi_1'(l_{11}) & \phi_1'(l_{22}) - \phi_1'(l_{12}) \\ \phi_2'(l_{21}) - \phi_2'(l_{11}) & \phi_2'(l_{22}) - \phi_2'(l_{12}) \\ \phi_3'(l_{21}) - \phi_3'(l_{11}) & \phi_3'(l_{22}) - \phi_3'(l_{12}) \\ \phi_4'(l_{21}) - \phi_4'(l_{11}) & \phi_4'(l_{22}) - \phi_4'(l_{12}) \end{bmatrix} \begin{bmatrix} V_1 \\ V_2 \end{bmatrix} = \tau \tag{69}$$

$$\begin{bmatrix} V_1 \\ V_2 \end{bmatrix} = \left(\begin{bmatrix} \phi_1'(l_{21}) - \phi_1'(l_{11}) & \phi_1'(l_{22}) - \phi_1'(l_{12}) \\ \phi_2'(l_{21}) - \phi_2'(l_{11}) & \phi_2'(l_{22}) - \phi_2'(l_{12}) \\ \phi_3'(l_{21}) - \phi_3'(l_{11}) & \phi_3'(l_{22}) - \phi_3'(l_{12}) \\ \phi_4'(l_{21}) - \phi_4'(l_{11}) & \phi_4'(l_{22}) - \phi_4'(l_{12}) \end{bmatrix} \right)^{-1} \tau \tag{70}$$

Equation (70) is the optimal least squares solution to Eq. (69). The model can be simplified to the case with one PZT, by replacing the second column of the Galerkin function dependent matrix in Eq. (69) with zeros.

5 Numerical Simulations

5.1 Formulation

The closed-loop system is simulated in Simulink nased on the flowchart in Fig. 8. The system properties used for simulation are given in Table 1 and correspond to the experimental setup described in Chapter 6.

Table 1: Physical, geometrical and structural parameters of Bus, Array and PZT.

ℓ	29.7×10^{-2} m	E_b	68.9 GPa	E_p	66 GPa
t_b	0.45×10^{-3} m	ρ_b	2738 kg/m^3	ρ_p	7800 kg/m^3
w	0.036 m	μ	10^{-4}	t_p	0.48×10^{-3} m
d_{31}	190×10^{-12} m/V	ℓ_{11}	1.1×10^{-2}m	ℓ_{21}	8.144×10^{-2} m
ℓ_{12}	8.614×10^{-2} m	ℓ_{22}	15.858×10^{-2} m	r	0.6×10^{-2}
J_θ	1.0759×10^{-6} m	-	-	-	-

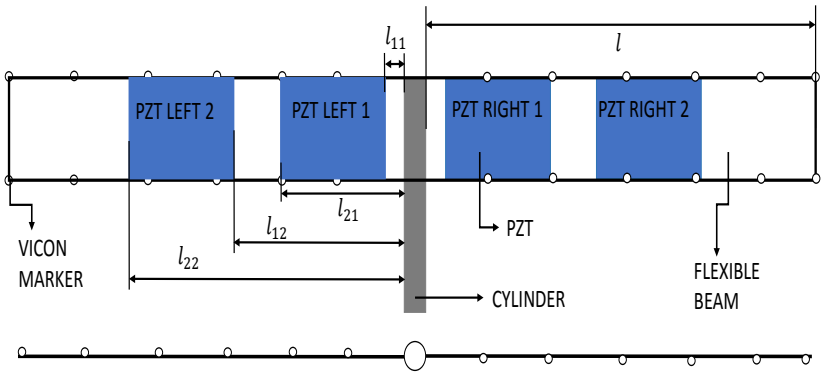

Figure 7: Front and Top view of the experimental setup.

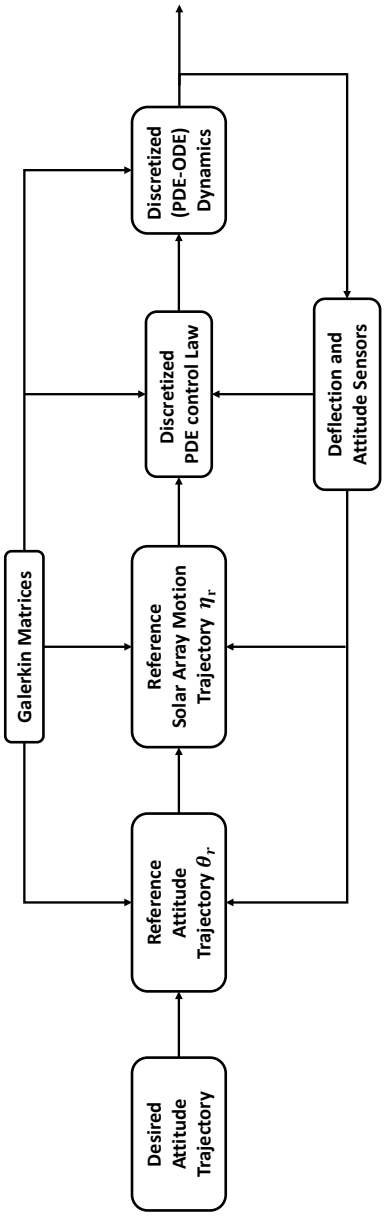

Figure 8: Closed-loop ODE system as implemented in Simulink.

The Galerkin matrices are computed using Eq. (81) for the configuration shown in Fig. 7. The functions in Eqs. (71 - 80) define axial stiffness at different cross sections of the beam. Using the Galerkin matrices, the closed-loop system defined by the ODE given in Eqs. (60)-(62), and Eqs. (64)-(66) can be integrated using Euler's method.

$$p_{10}(x) = \int_{r+x}^{r+\ell} m_b s ds + m_v(r + \ell_{v_6}), \tag{71}$$

$$p_9(x) = m_b \int_{r+x}^{r+\ell_{v_5}} s ds + m_b \int_{r+\ell_{v_5}}^{r+\ell} s ds + m_v(r + \ell_{v_5}) + m_v(r + \ell_{v_6}) \tag{72}$$

$$\begin{aligned} p_8(x) = {} & m_b \int_{r+x}^{r+\ell_{v_4}} s ds + m_v(r + \ell_{v_4}) + m_b \int_{r+\ell_{v_4}}^{r+\ell_{v_5}} s ds + m_b \int_{r+\ell_{v_5}}^{r+\ell} s ds \\ & + m_v(r + \ell_{v_5}) + m_v(r + \ell_{v_6}) \end{aligned} \tag{73}$$

$$\begin{aligned} p_7(x) = {} & m_R \int_{r+x}^{r+\ell_{22}} s ds + m_b \int_{r+\ell_{22}}^{r+\ell_{v_4}} s ds + m_v(r + \ell_{v_4}) + m_b \int_{r+\ell_{v_4}}^{r+\ell_{v_5}} s ds \\ & + m_b \int_{r+\ell_{v_5}}^{r+\ell} s ds + m_v(r + \ell_{v_5}) + m_v(r + \ell_{v_6}) \end{aligned} \tag{74}$$

$$\begin{aligned} p_6(x) = {} & m_R \int_{r+x}^{r+\ell_{v_3}} s ds + m_R \int_{r+\ell_{v_3}}^{r+\ell_{22}} s ds + m_b \int_{r+\ell_{22}}^{r+\ell_{v_4}} s ds + m_v(r + \ell_{v_4}) \\ & + m_b \int_{r+\ell_{v_4}}^{r+\ell_{v_5}} s ds + m_b \int_{r+\ell_{v_5}}^{r+\ell} s ds + m_v(r + \ell_{v_5}) + m_v(r + \ell_{v_6}) \end{aligned} \tag{75}$$

$$\begin{aligned} p_5(x) = {} & m_R \int_{r+x}^{r+\ell_{v_2}} s ds + m_v(r + \ell_{v_2}) + m_R \int_{r+\ell_{v_2}}^{r+\ell_{v_3}} s ds \\ & + m_R \int_{r+\ell_{v_3}}^{r+\ell_{22}} s ds + m_b \int_{r+\ell_{22}}^{r+\ell_{v_4}} s ds + m_v(r + \ell_{v_4}) + m_b \int_{r+\ell_{v_4}}^{r+\ell_{v_5}} s ds \\ & + m_b \int_{r+\ell_{v_5}}^{r+\ell} s ds + m_v(r + \ell_{v_5}) + m_v(r + \ell_{v_6} \end{aligned} \tag{76}$$

$$\begin{aligned} p_4(x) = {} & m_b \int_{r+x}^{r+\ell_{12}} s ds + m_R \int_{r+\ell_{12}}^{r+\ell_{v_2}} s ds + m_v(r + \ell_{v_2}) + m_R \int_{r+\ell_{v_2}}^{r+\ell_{v_3}} s ds \\ & + m_R \int_{r+\ell_{v_3}}^{r+\ell_{22}} s ds + m_b \int_{r+\ell_{22}}^{r+\ell_{v_4}} s ds + m_v(r + \ell_{v_4}) + m_b \int_{r+\ell_{v_4}}^{r+\ell_{v_5}} s ds \\ & + m_b \int_{r+\ell_{v_5}}^{r+\ell} s ds + m_v(r + \ell_{v_5}) + m_v(r + \ell_{v_6}) \end{aligned} \tag{77}$$

$$
\begin{aligned}
p_3(x) = {} & m_R \int_{r+x}^{r+\ell_{21}} sds + m_b \int_{r+\ell_{21}}^{r+\ell_{12}} sds + m_R \int_{r+\ell_{12}}^{r+\ell_{v_2}} sds + m_v(r+\ell_{v_2}) \\
& + m_R \int_{r+\ell_{v_2}}^{r+\ell_{v_3}} sds + m_R \int_{r+\ell_{v_3}}^{r+\ell_{22}} sds + m_b \int_{r+\ell_{22}}^{r+\ell_{v_4}} sds + m_v(r+\ell_{v_4}) \\
& + m_b \int_{r+\ell_{v_4}}^{r+\ell_{v_5}} sds + m_b \int_{r+\ell_{v_5}}^{r+\ell} sds + m_v(r+\ell_{v_5}) + m_v(r+\ell_{v_6})
\end{aligned} \tag{78}
$$

$$
\begin{aligned}
p_2(x) = {} & m_R \int_{r+x}^{r+\ell_{v_1}} sds + m_v(r+\ell_{v_1}) + m_R \int_{r+x}^{r+\ell_{21}} sds + m_b \int_{r+\ell_{21}}^{r+\ell_{12}} sds \\
& + m_R \int_{r+\ell_{12}}^{r+\ell_{v_2}} sds + m_v(r+\ell_{v_2}) + m_R \int_{r+\ell_{v_2}}^{r+\ell_{v_3}} sds \\
& + m_R \int_{r+\ell_{v_3}}^{r+\ell_{22}} sds + m_b \int_{r+\ell_{22}}^{r+\ell_{v_4}} sds + m_v(r+\ell_{v_4}) + m_b \int_{r+\ell_{v_4}}^{r+\ell_{v_5}} sds \\
& + m_b \int_{r+\ell_{v_5}}^{r+\ell} sds + m_v(r+\ell_{v_5}) + m_v(r+\ell_{v_6})
\end{aligned} \tag{79}
$$

$$
\begin{aligned}
p_1(x) = {} & m_b \int_{r+x}^{r+\ell_{11}} sds + m_R \int_{r+\ell_{11}}^{r+\ell_{v_1}} sds + m_v(r+\ell_{v_1}) + m_R \int_{r+x}^{r+\ell_{21}} sds \\
& + m_b \int_{r+\ell_{21}}^{r+\ell_{12}} sds + m_R \int_{r+\ell_{12}}^{r+\ell_{v_2}} sds + m_v(r+\ell_{v_2}) + m_R \int_{r+\ell_{v_2}}^{r+\ell_{v_3}} sds \\
& + m_R \int_{r+\ell_{v_3}}^{r+\ell_{22}} sds + m_b \int_{r+\ell_{22}}^{r+\ell_{v_4}} sds + m_v(r+\ell_{v_4}) + m_b \int_{r+\ell_{v_4}}^{r+\ell_{v_5}} sds \\
& + m_b \int_{r+\ell_{v_5}}^{r+\ell} sds + m_v(r+\ell_{v_5}) + m_v(r+\ell_{v_6})
\end{aligned} \tag{80}
$$

$$
\begin{aligned}
[A] = {} & \int_0^{\ell_{11}} m_b \phi\phi^T dx + \int_{\ell_{11}}^{\ell_{21}} m_R \phi\phi^T dx + \int_{\ell_{21}}^{\ell_{12}} m_b \phi\phi^T dx + \int_{\ell_{12}}^{\ell_{22}} m_R \phi\phi^T dx \\
& + \int_{\ell_{22}}^{\ell} m_b \phi\phi^T dx + m_v \phi\phi^T|_{x=l_{v_1}} + m_v \phi\phi^T|_{x=l_{v_2}} + m_v \phi\phi^T|_{x=l_{v_3}} \\
& + m_v \phi\phi^T|_{x=l_{v_4}} + m_v \phi\phi^T|_{x=l_{v_5}} + m_v \phi\phi^T|_{x=l_{v_6}}
\end{aligned} \tag{81a}
$$

$$
\begin{aligned}
[C] &= \int_0^{\ell_{11}} m_b(x+r)\phi dx + \int_{\ell_{11}}^{\ell_{21}} m_R(x+r)\phi dx + \int_{\ell_{21}}^{\ell_{12}} m_b(x+r)\phi dx \\
&+ \int_{\ell_{12}}^{\ell_{22}} m_R(x+r)\phi dx + \int_{\ell_{22}}^{\ell} m_b(x+r)\phi dx + m_v\phi(x+r)|_{x=l_{v_1}} \\
&+ m_v\phi(x+r)|_{x=l_{v_2}} + m_v\phi(x+r)|_{x=l_{v_3}} + m_v\phi(x+r)|_{x=l_{v_4}} \\
&+ m_v\phi(x+r)|_{x=l_{v_5}} + m_v\phi(x+r)|_{x=l_{v_6}}
\end{aligned} \tag{81b}
$$

$$
\begin{aligned}
[E] &= \int_0^{\ell_{11}} EI_b\phi\phi^{''''T} dx + \int_{\ell_{11}}^{\ell_{21}} EI_t\phi\phi^{''''T} dx + \int_{\ell_{21}}^{\ell_{12}} EI_b\phi\phi^{''''T} dx \\
&+ \int_{\ell_{12}}^{\ell_{22}} EI_t\phi\phi^{''''T} dx + \int_{\ell_{22}}^{\ell} EI_b\phi\phi^{''''T} dx
\end{aligned} \tag{81c}
$$

$$
\begin{aligned}
[B] &= \int_0^{\ell_{11}} p_1(x)\phi^{'}\phi^{'T} dx + \int_{\ell_{11}}^{\ell_{v_1}} p_2(x)\phi^{'}\phi^{'T} dx + \int_{\ell_{v_1}}^{\ell_{21}} p_3(x)\phi^{'}\phi^{'T} dx \\
&+ \int_{\ell_{21}}^{\ell_{12}} p_4(x)\phi^{'}\phi^{'T} dx + \int_{\ell_{12}}^{\ell_{v_2}} p_5(x)\phi^{'}\phi^{'T} dx + \int_{\ell_{v_2}}^{\ell_{v_3}} p_6(x)\phi^{'}\phi^{'T} dx \\
&+ \int_{\ell_{v_3}}^{\ell_{22}} p_7(x)\phi^{'}\phi^{'T} dx + \int_{\ell_{22}}^{\ell_{v_4}} p_8(x)\phi^{'}\phi^{'T} dx + \int_{\ell_{v_4}}^{\ell_{v_5}} p_9(x)\phi^{'}\phi^{'T} dx \\
&+ \int_{\ell_{v_5}}^{\ell_{v_6}} p_{10}(x)\phi^{'}\phi^{'T} dx
\end{aligned} \tag{81d}
$$

$$
[A] = \begin{bmatrix}
0.264 & -0.6009 & 1.6038 & -2.6446 \\
-0.6009 & 1.4694 & -3.6984 & 6.2020 \\
1.6038 & -3.6984 & 9.8163 & -16.1620 \\
-2.6446 & 6.2020 & -16.1620 & 26.8670
\end{bmatrix} \tag{82a}
$$

$$
[C] = \begin{bmatrix}
0.0141 & -0.0298 & 0.0850 & -0.1367
\end{bmatrix} \tag{82b}
$$

$$[E] = 1.0e+05 \begin{bmatrix} 0.0004 & 0.0250 & 0.0908 & -0.2259 \\ -0.0024 & -0.0160 & -0.0887 & 0.4024 \\ 0.0015 & 0.1299 & 0.6259 & -1.0887 \\ -0.0072 & -0.1983 & -0.7193 & 2.5227 \end{bmatrix} \tag{82c}$$

$$[B] = \begin{bmatrix} 0.3326 & -0.8411 & 1.9941 & -3.5240 \\ -0.8411 & 2.5495 & -5.3221 & 9.5762 \\ 1.9941 & -5.3221 & 12.7840 & -21.6810 \\ -3.5240 & 9.5762 & -21.6810 & 39.3600 \end{bmatrix} \tag{82d}$$

$$c = -1.2028e-05 \tag{82e}$$

5.2 Results

The Galerkin matrices are computed offline using Eqs. (81a-81d), given in Eqs. (82). The closed-loop system is simulated using Simulink, with the Galerking matrices. Here we track a sinusoidal signal of amplitude 0.001 radians and frequency 0.02Hz, and slew from a zero initial attitude to 0.001 radians using both controller 1 and controller 2 for different values of 'δ'. We present results for two cases: 1) Configuration 1: with only 'PZT LEFT 1' and 'PZT RIGHT 1' active (see Fig. 7), and 2) Configuration 2: Distributed configuration, with all the four PZTs active. For controller 1 and 2, it was observed that trajectory tracking and slewing is achieved for $\delta \in [0, 1]$ with the specified gain values.

For controller 1, in configuration 1 we present results for $\delta = \{1, 0.5, 0\}$, (see Figs. 9–11) for trajectory tracking and (Figs. 12–14) for slewing. If the closed-loop simulation is performed with the same gain values for the three δ values, it was

observed that the tracking error is inversely proportional to the 'δ' value in the range $[0, 1]$. The voltage signals were computed from the control signal online using Eq. (70). Note that the maximum voltage required to do the tracking and slewing is well within $\pm 200V$ (the saturation limit of the PZT actuator used in experiments). It is observed that the controller 1 predominantly uses first free vibration mode of the beam to achieve tracking. The deflections in the beam during the closed-loop simulations are shown in Fig. 52 (although not plotted here, the bending in all the cases is the same as shown in Fig. 52). Note that for an anti-clockwise rotation of the spacecraft, the solar array bends in the clockwise direction. For slewing results, the time to reach steady state is increased for smaller δ. Figures 15–16 show tracking and slewing in configuration 2.

For controller 2 in configuration 1, the closed-loop system is simulated for $\delta = \{1, 0.0001, 1e-5\}$ using different gain values. See Figs. 9–21 for trajectory tracking and Figs. 22–24 for slewing. In configuration 2, trajectory tracking and slewing are simulated for $\delta = 0.0001$ (Figs 25–26). Similar to controller 1, as δ value gets close to one, the tracking error becomes small for the gain values chosen. Unlike controller 1, for $\delta = 1$ the control effort is high and would saturate the PZTs during the experiment. To avoid saturation, we choose smaller δ values to make sure that the control effort is within the saturation limit. While for $\delta = 0.0001$ the control effort is more than that predicted by controller 1, it is within the saturation limit. Based on these simulation results, experiments are performed for values of δ for which control effort is within $\pm 200V$.

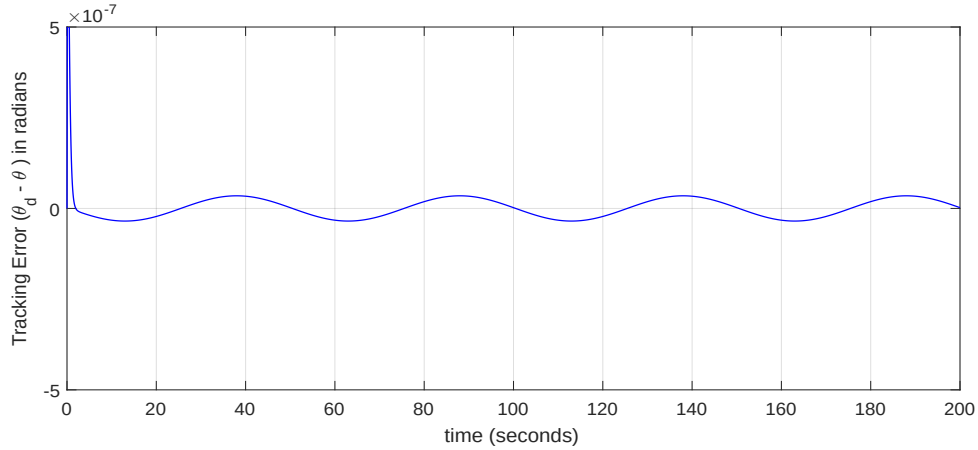

(9a) Tracking error.

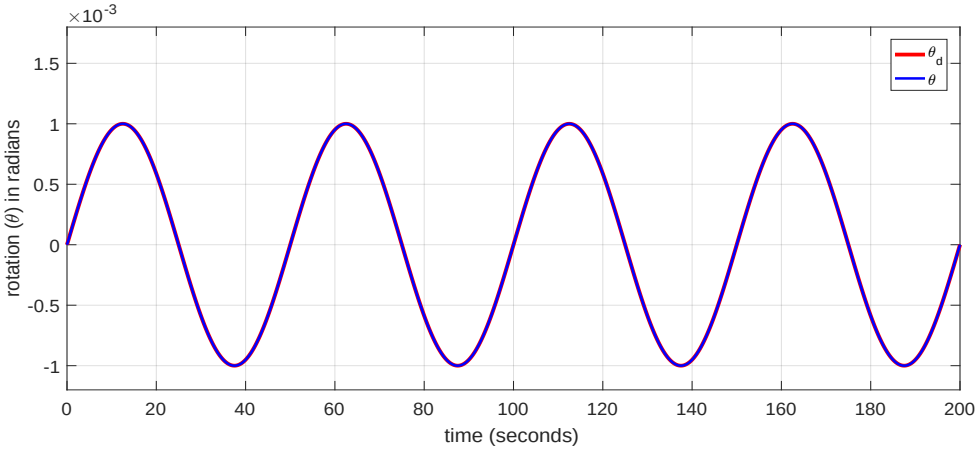

(9b) Trajectory tracking.

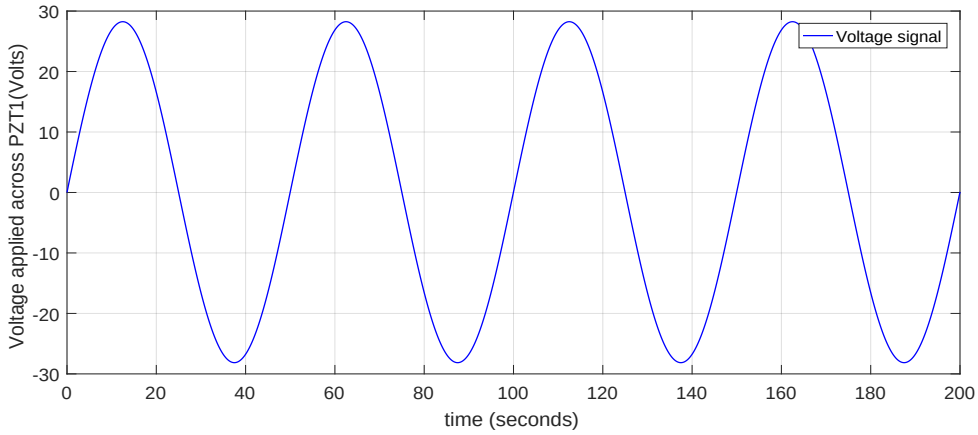

(9c) Control effort in Volts.

Figure 9: Trajectory tracking (Simulation) for $\delta = 1$ using controller 1 with gains $\lambda = 3$, $K_\theta = 0.5$, $K_\xi = 0.5$.

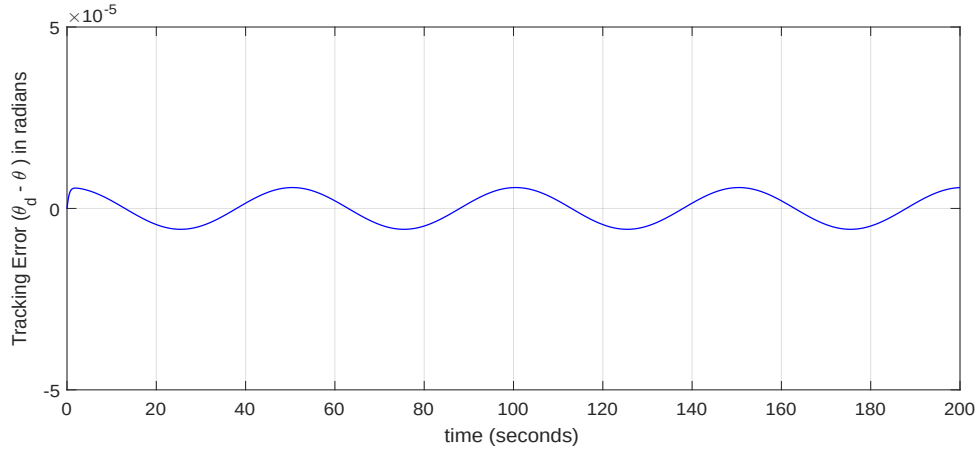

(10a) Tracking error.

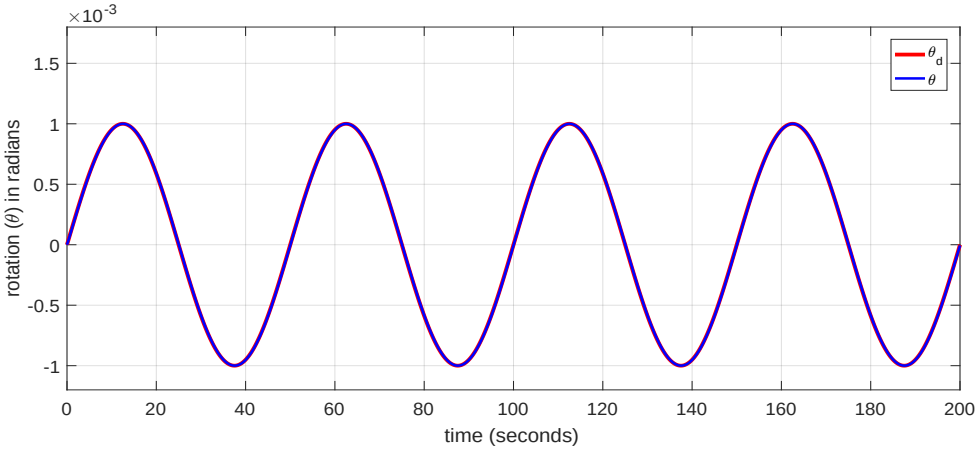

(10b) Trajectory tracking.

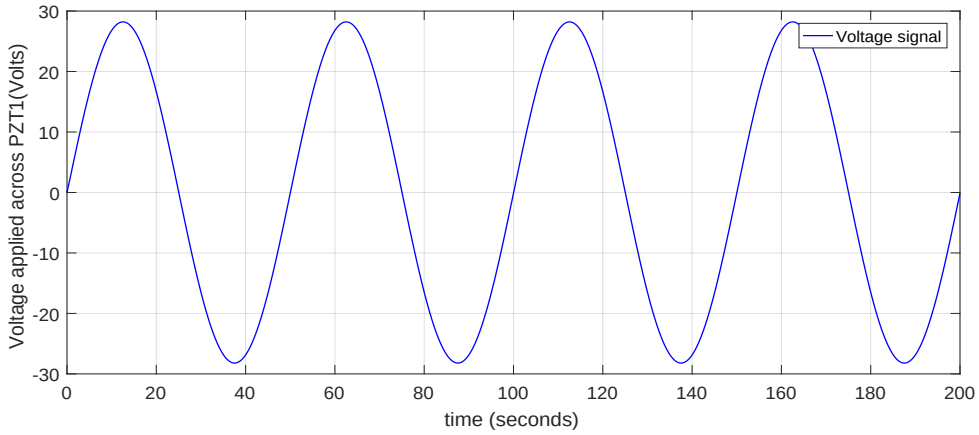

(10c) Control effort in Volts.

Figure 10: Trajectory tracking (Simulation) for $\delta = 0.5$ using controller 1 with gains $\lambda = 3$, $K_\theta = 0.5$, $K_\xi = 0.5$.

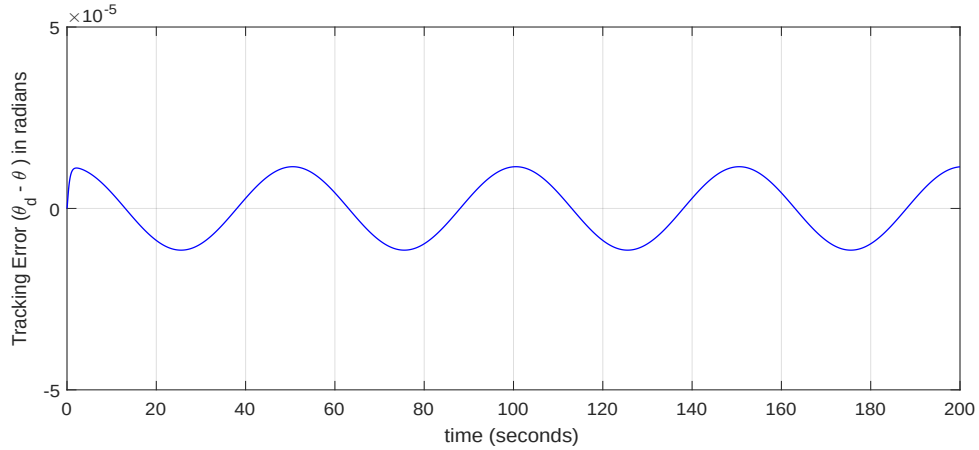

(11a) Tracking error.

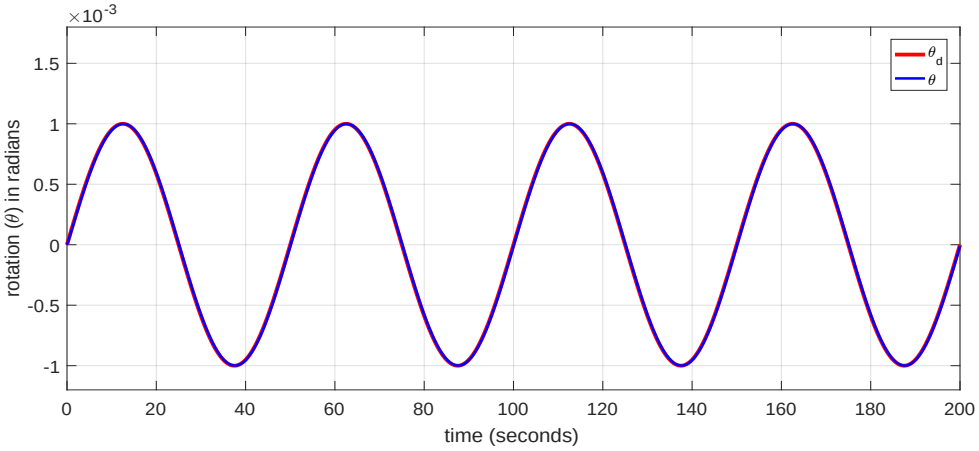

(11b) Trajectory tracking.

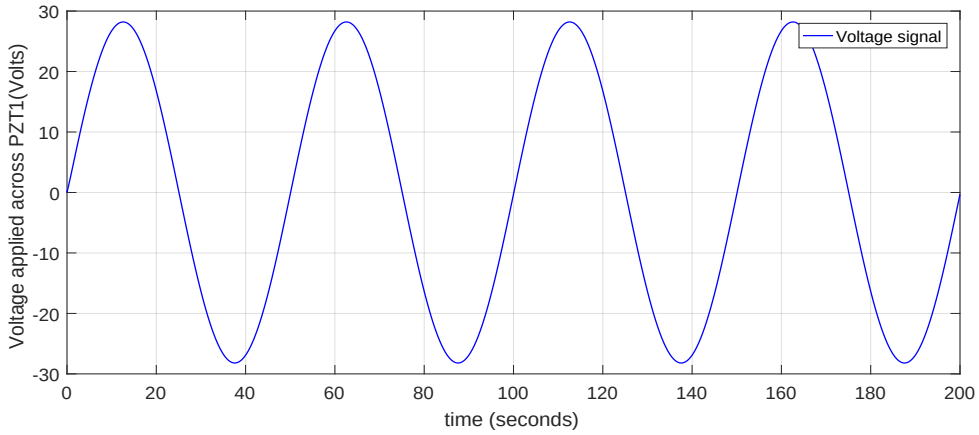

(11c) Control effort in Volts.

Figure 11: Trajectory tracking (Simulation) for $\delta = 0$ using controller 1 with gains $\lambda = 3$, $K_\theta = 0.5$, $K_\xi = 0.5$.

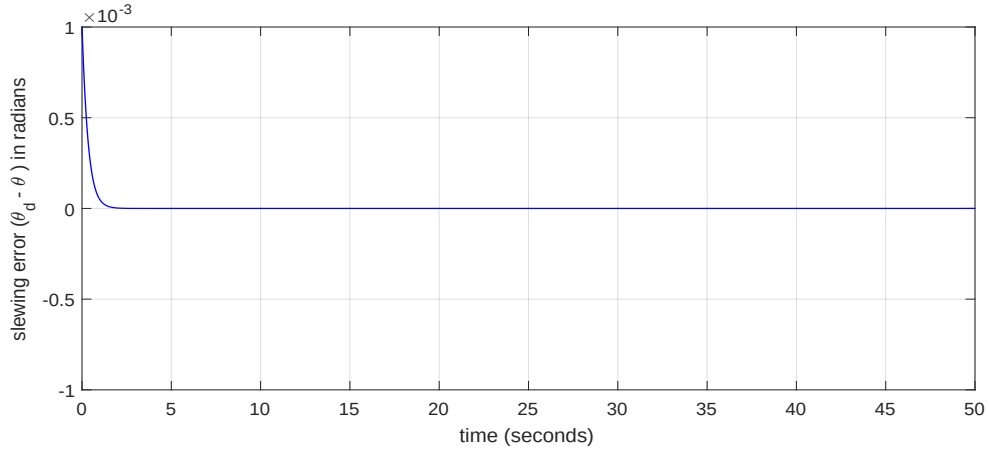

(12a) Slewing error.

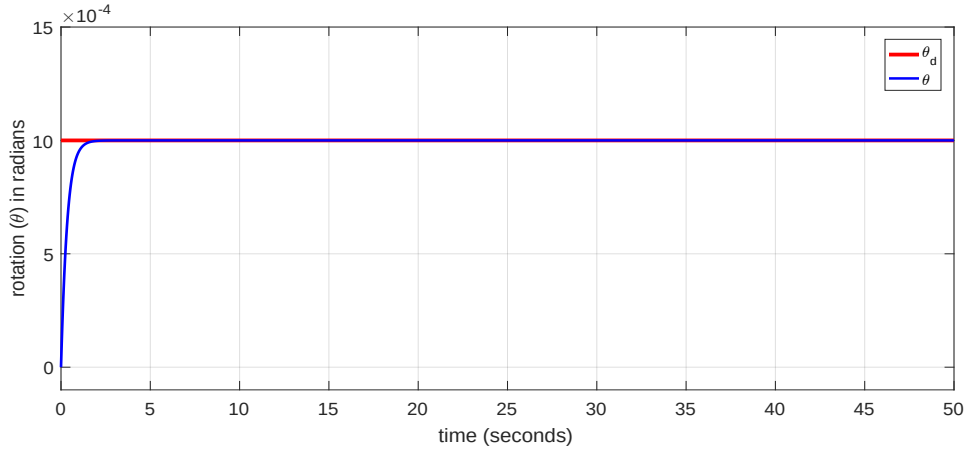

(12b) Slewing.

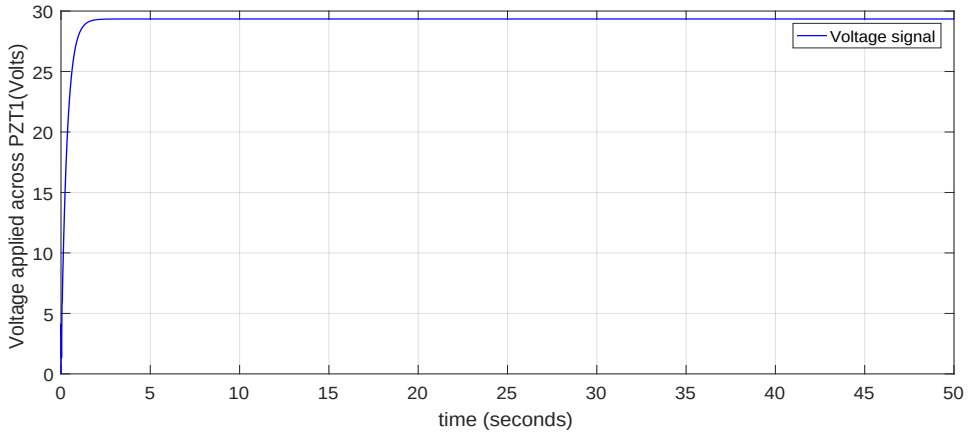

(12c) Control effort in Volts.

Figure 12: Slewing (Simulation) for $\delta = 1$ using controller 1 with gains $\lambda = 3$, $K_\theta = 0.5$, $K_\xi = 0.5$.

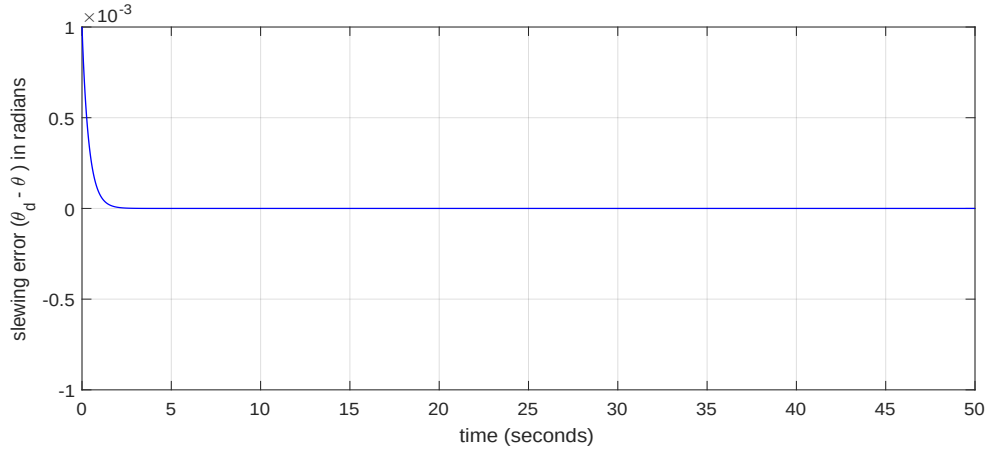

(13a) Slewing error.

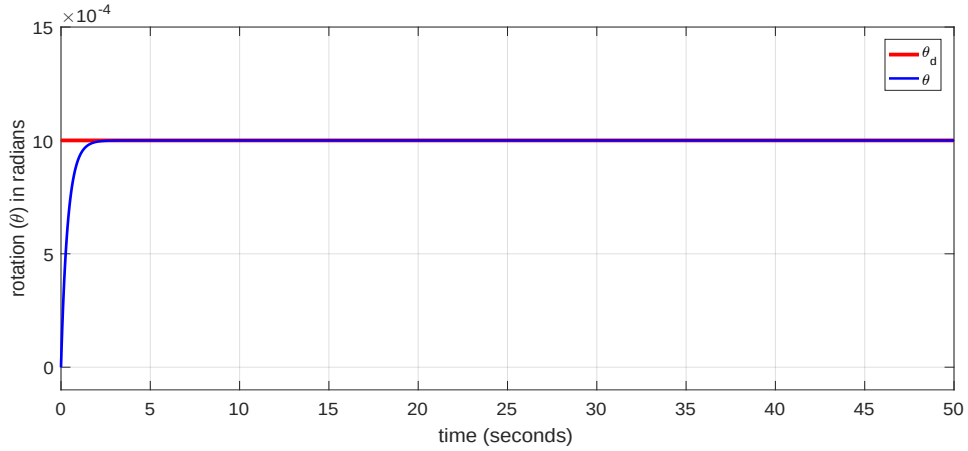

(13b) Slewing.

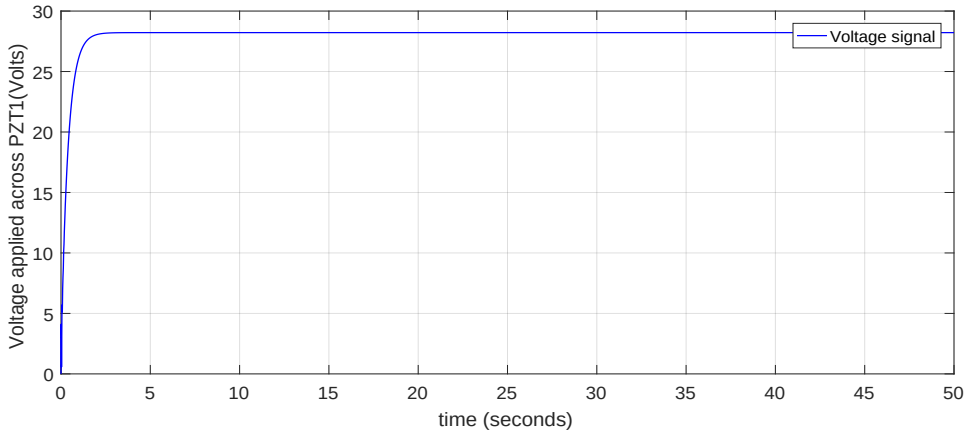

(13c) Control effort in Volts.

Figure 13: Slewing (Simulation) for $\delta = 0.5$ using controller 1 with gains $\lambda = 3$, $K_\theta = 0.5$, $K_\xi = 0.5$.

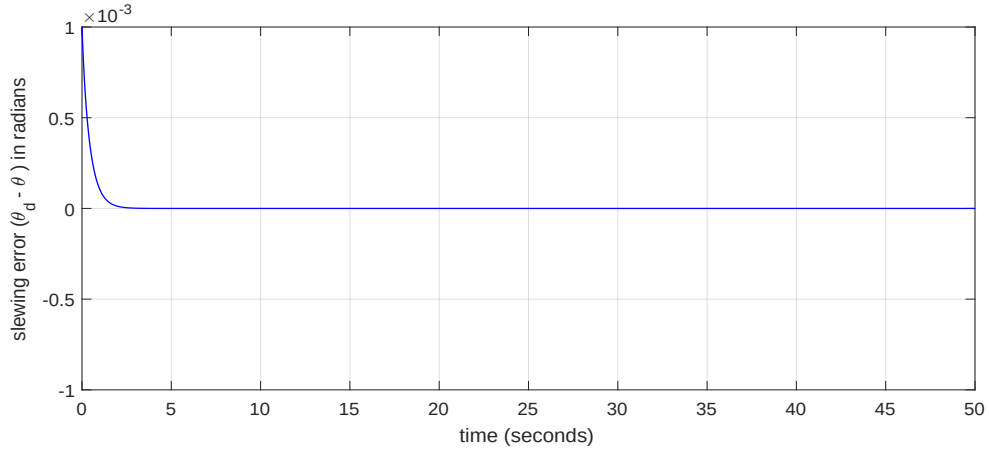

(14a) Slewing error.

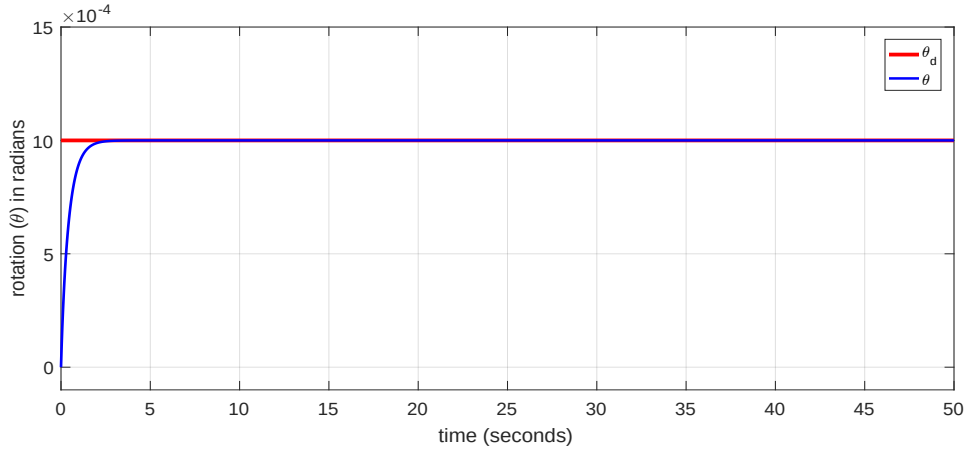

(14b) Slewing.

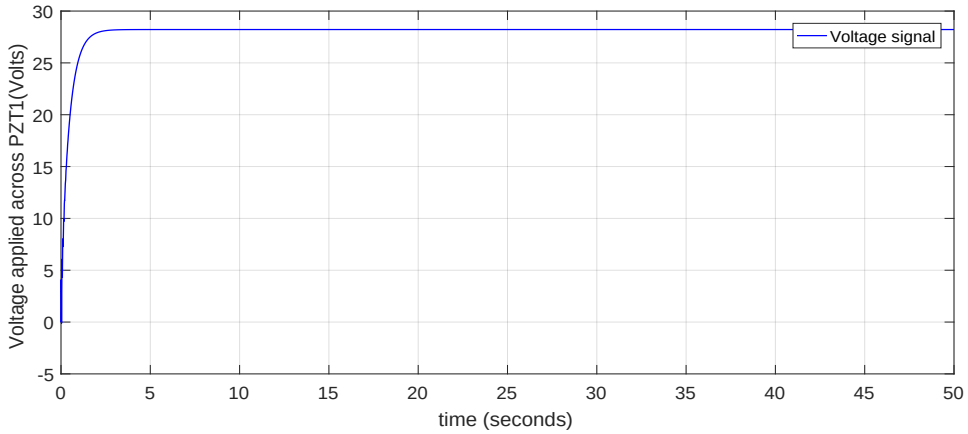

(14c) Control effort in Volts.

Figure 14: Slewing (Simulation) for $\delta = 0$ using controller 1 with gains $\lambda = 3$, $K_\theta = 0.5$, $K_\xi = 0.5$.

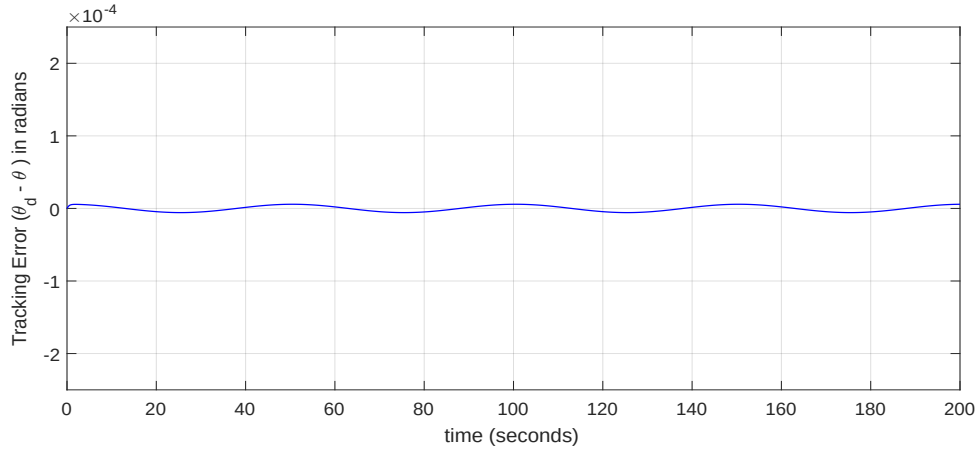

(15a) Tracking error.

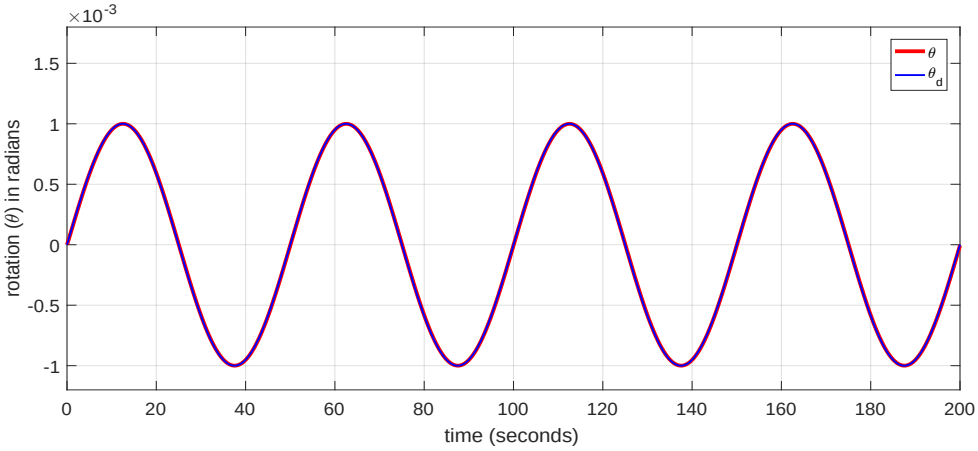

(15b) Trajectory tracking.

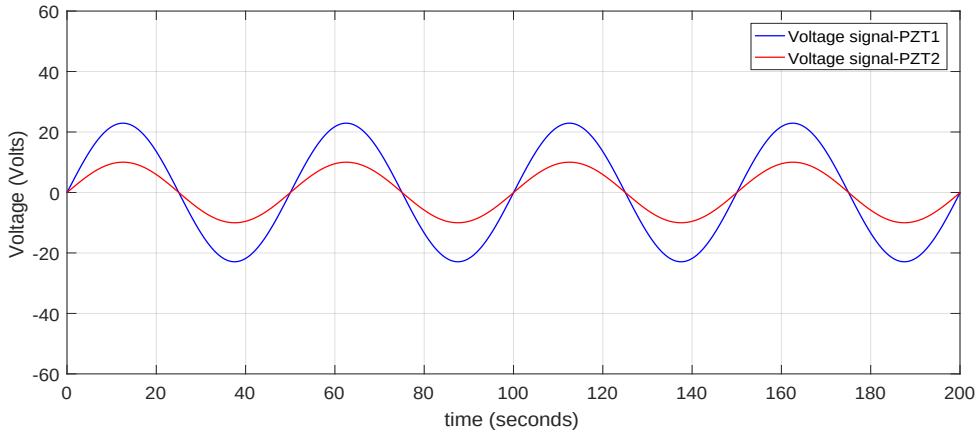

(15c) Control effort in Volts.

Figure 15: Trajectory tracking (Simulation) for $\delta = 0.5$ using controller 1 distributed PZT (configuration 2) with gains $\lambda = 3$, $K_\theta = 0.5$, $K_\xi = 0.5$.

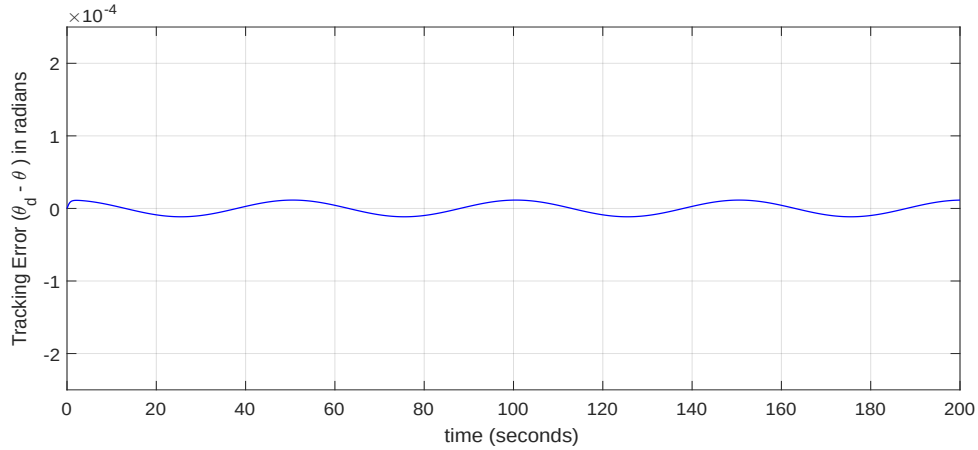

(16a) Tracking error.

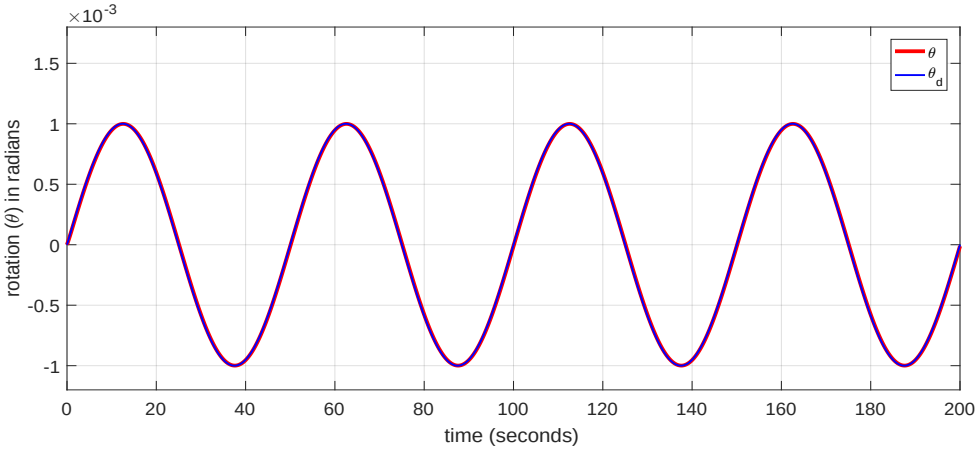

(16b) Trajectory tracking.

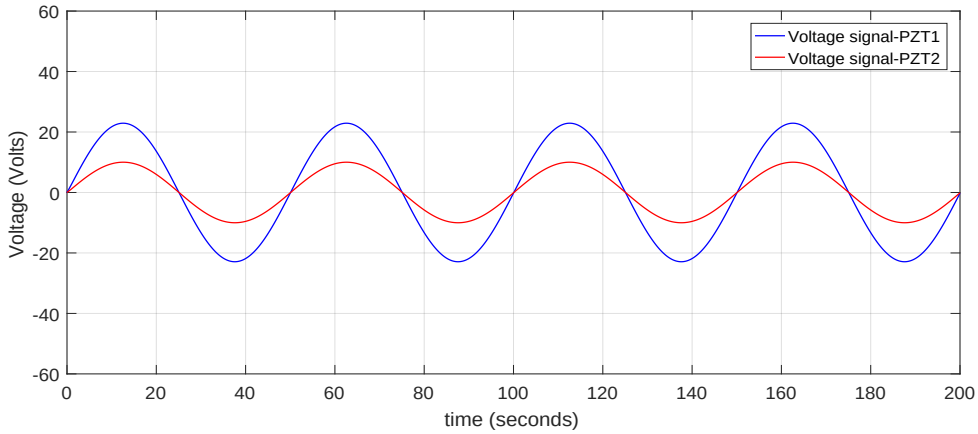

(16c) Control effort in Volts.

Figure 16: Trajectory tracking (Simulation) for $\delta = 0$ using controller 1 distributed PZT (configuration 2) with gains $\lambda = 3$, $K_\theta = 0.5$, $K_\xi = 0.5$.

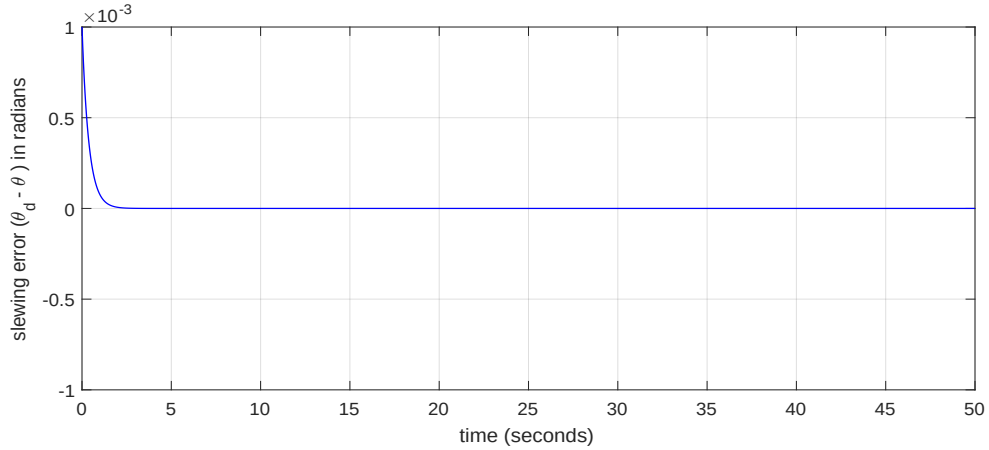

(17a) Slewing error.

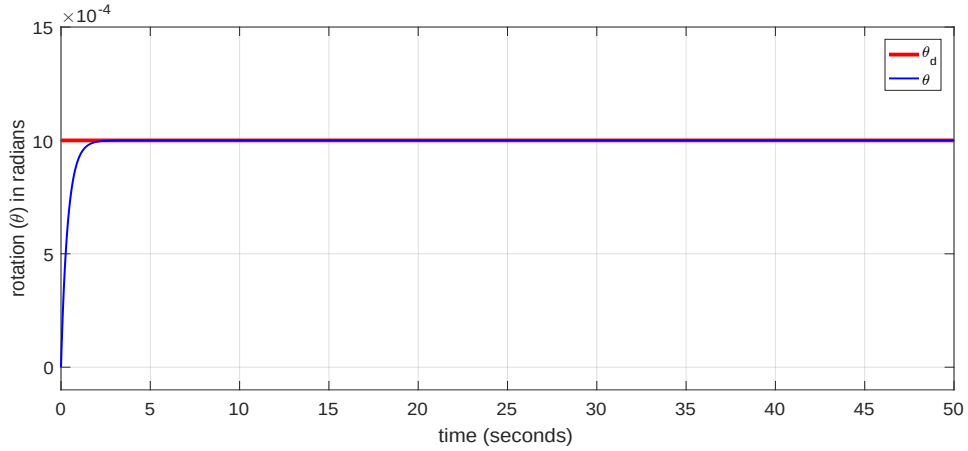

(17b) Slewing.

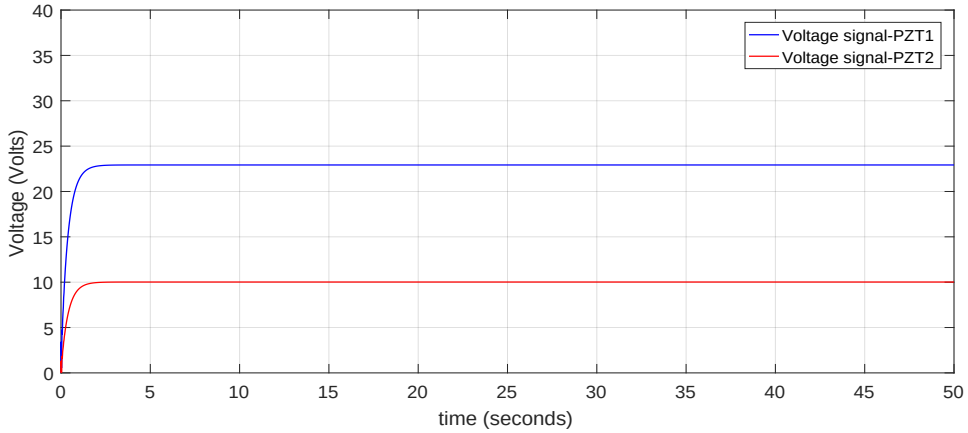

(17c) Control effort in Volts.

Figure 17: Slewing (Simulation) for $\delta = 0.5$ using controller 1 distributed PZT (configuration 2) with gains $\lambda = 3$, $K_\theta = 0.5$, $K_\xi = 0.5$.

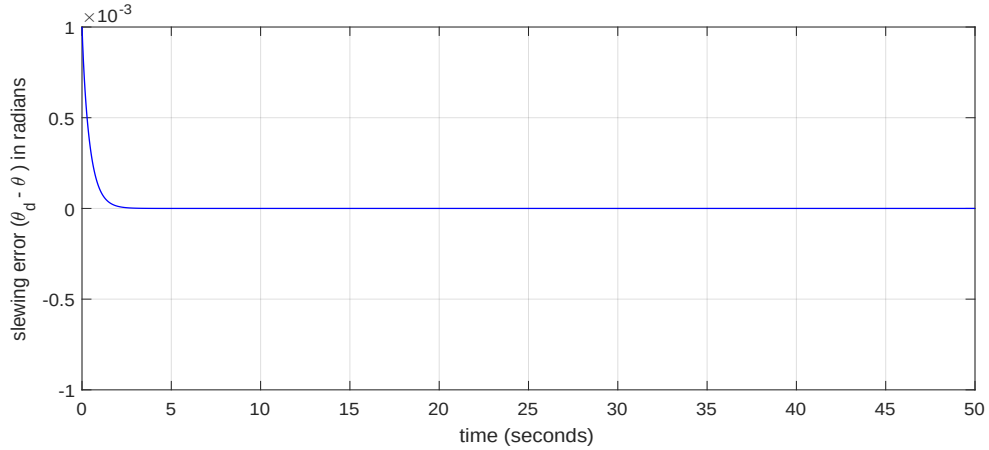

(18a) Slewing error.

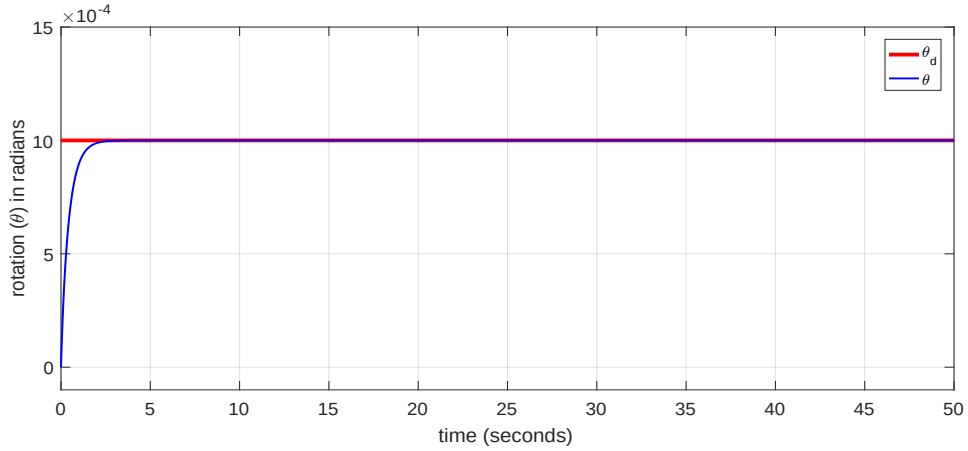

(18b) Slewing.

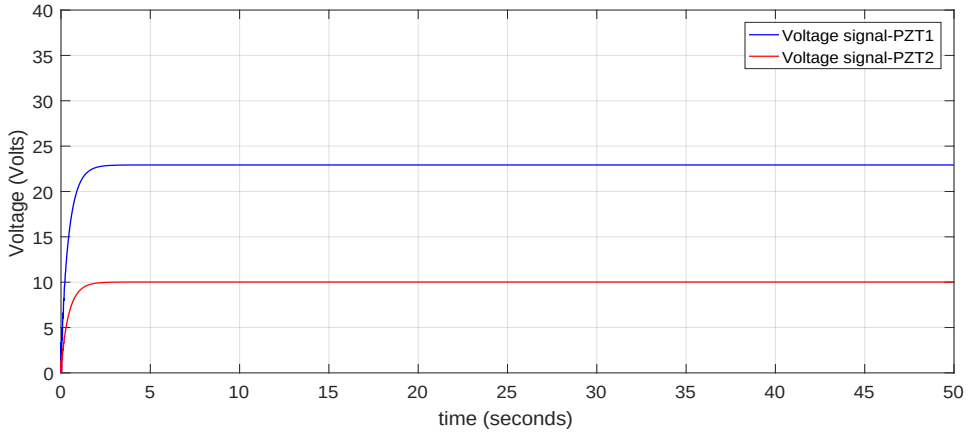

(18c) Control effort in Volts.

Figure 18: Slewing (Simulation) for $\delta = 0$ using controller 1 with gains distributed PZT (configuration 2) $\lambda = 3$, $K_\theta = 0.5$, $K_\xi = 0.5$.

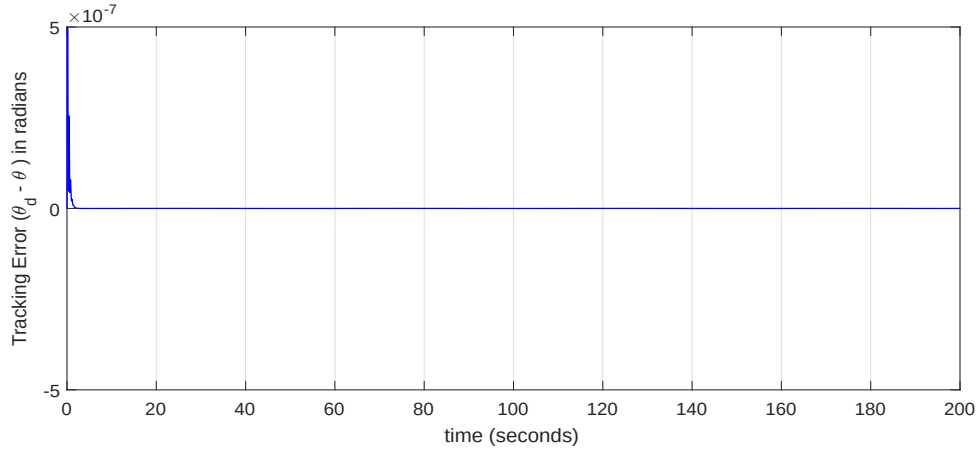

(19a) Tracking error.

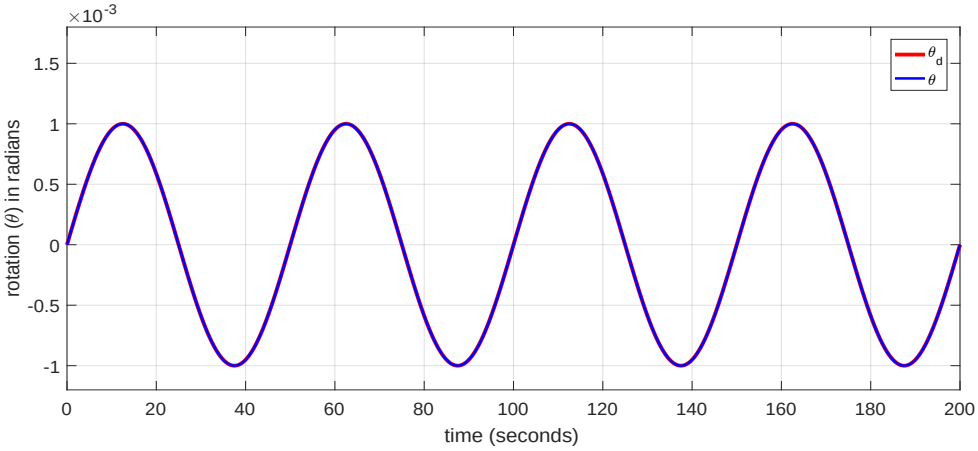

(19b) Trajectory tracking.

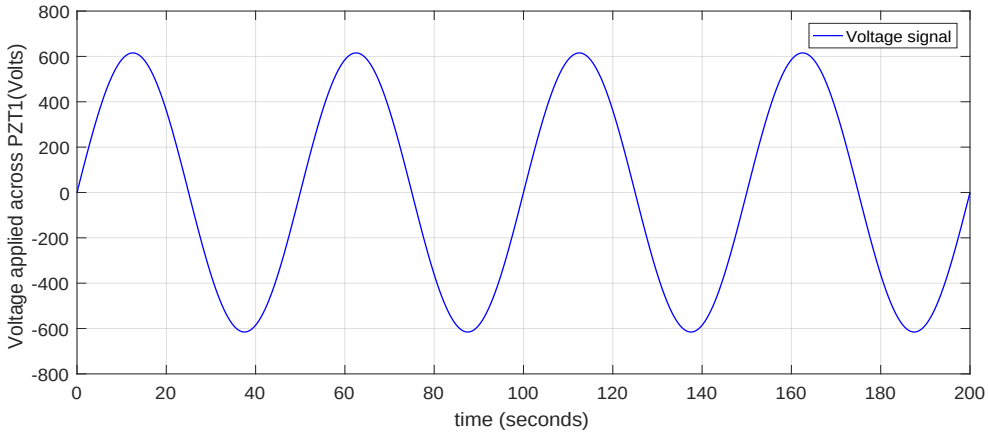

(19c) Control effort in Volts.

Figure 19: Trajectory tracking (Simulation) for $\delta = 1$ using controller 2 with gains $\lambda = 3$, $K_\theta = 0.5$, $K_\xi = 0.5$.

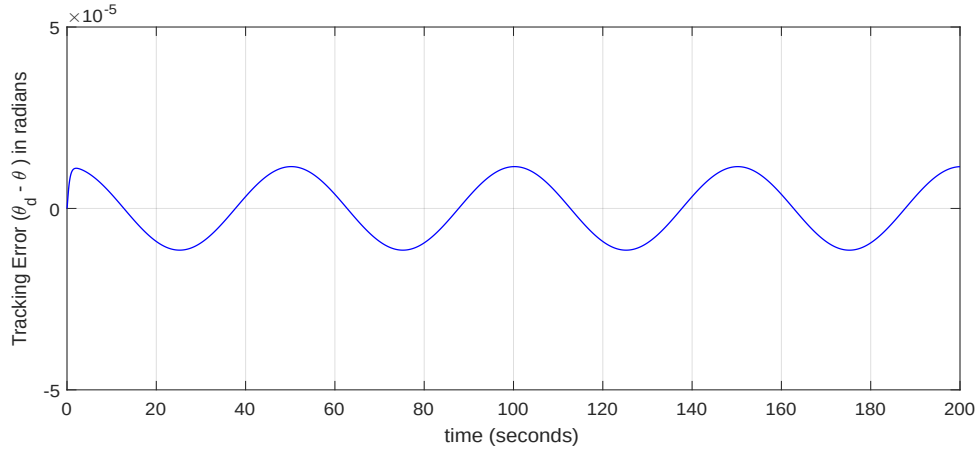

(20a) Tracking error.

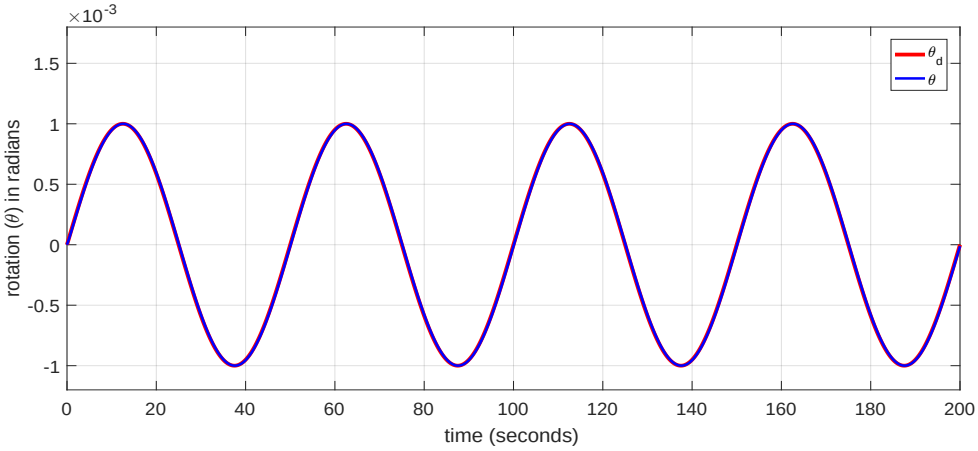

(20b) Trajectory tracking.

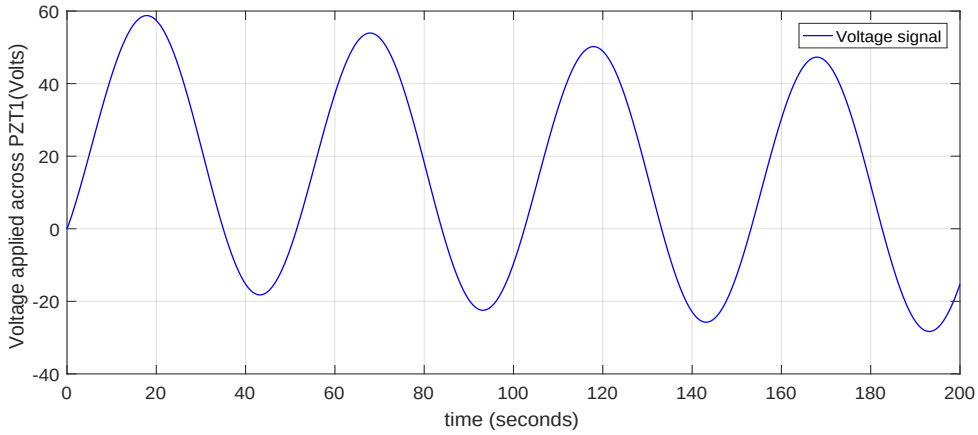

(20c) Control effort in Volts.

Figure 20: Trajectory tracking (Simulation) for $\delta = 0.0001$ using controller 2 with gains $\lambda = 10$, $K_\theta = 5$, $K_\xi = 5$.

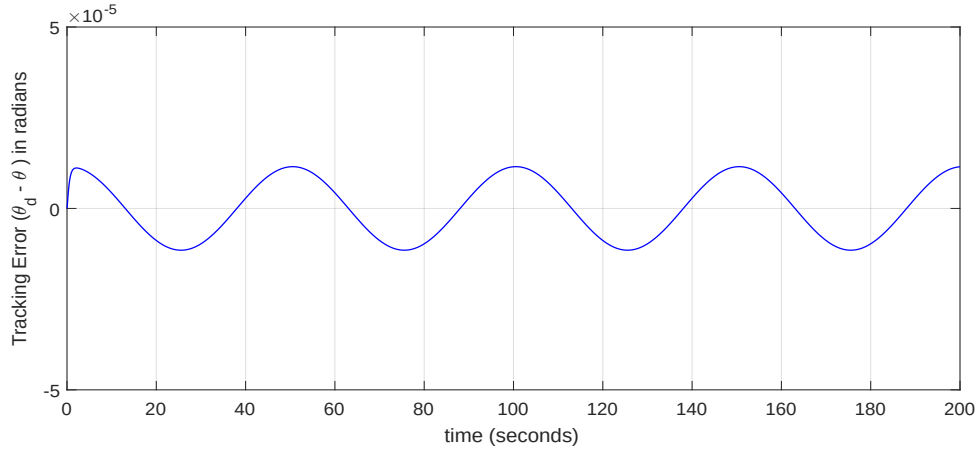

(21a) Tracking error.

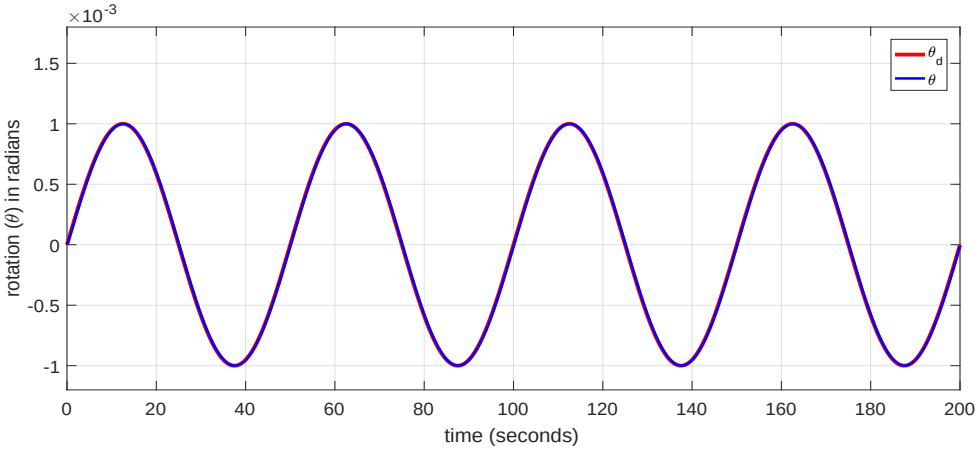

(21b) Trajectory tracking.

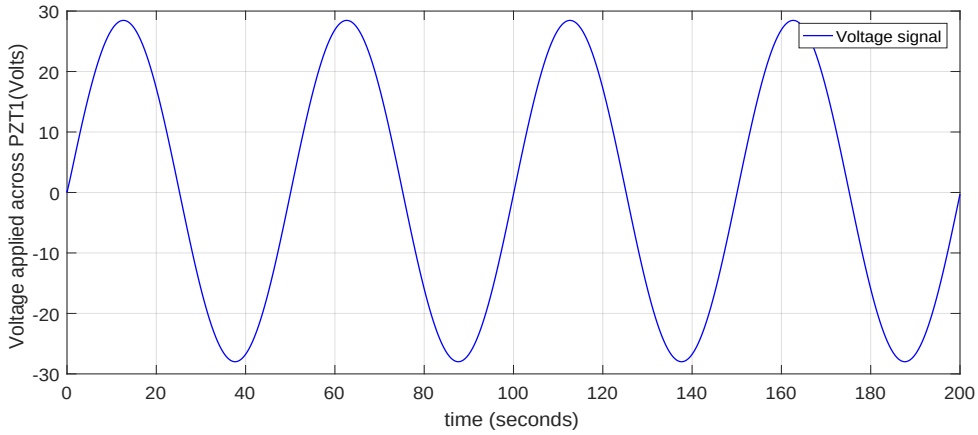

(21c) Control effort in Volts.

Figure 21: Trajectory tracking (Simulation) for $\delta = 1e-5$ using controller 2 with gains $\lambda = 3$, $K_\theta = 0.5$, $K_\xi = 0.5$.

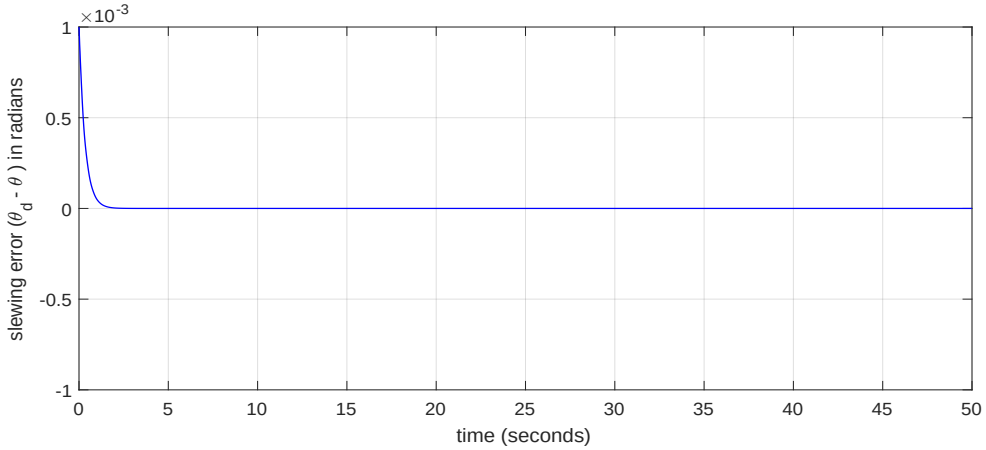

(22a) Slewing error.

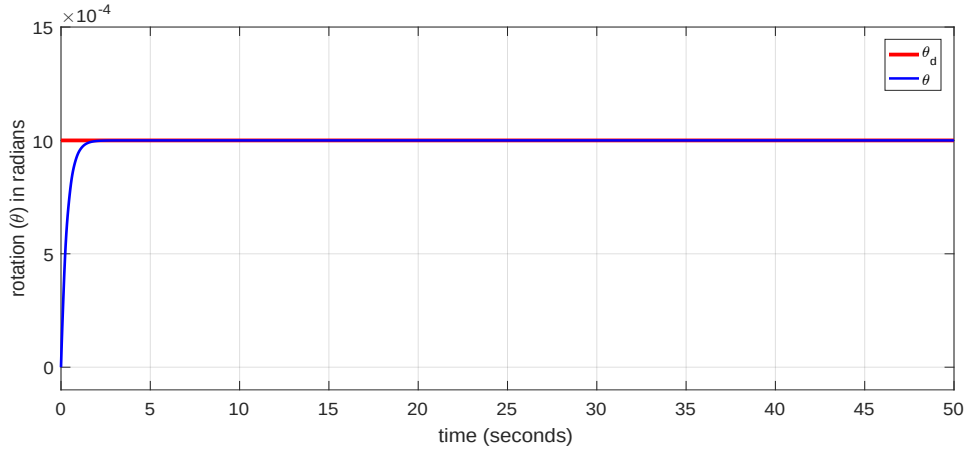

(22b) Slewing.

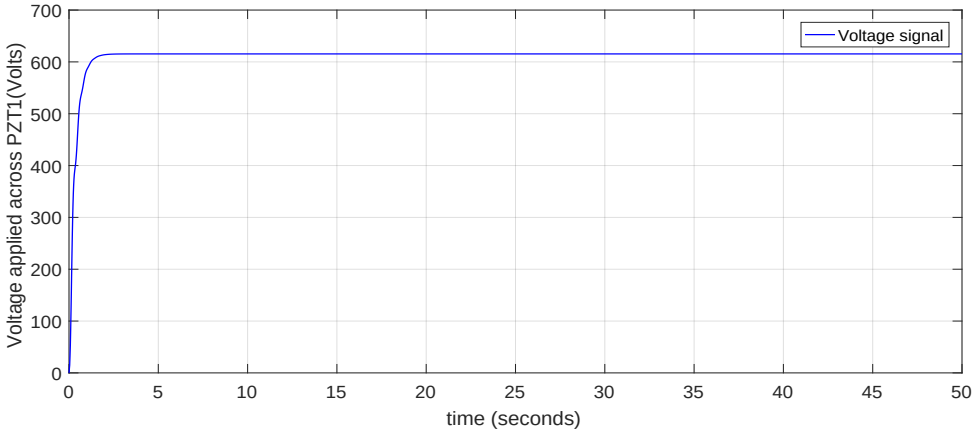

(22c) Control effort in Volts.

Figure 22: Slewing (Simulation) for $\delta = 1$ using controller 2 with gains $\lambda = 3$, $K_\theta = 0.5$, $K_\xi = 0.5$.

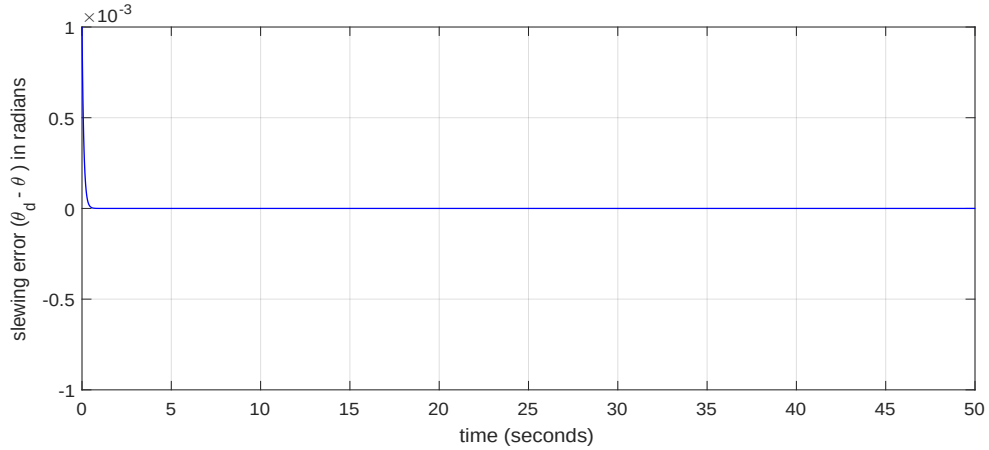

(23a) Slewing error.

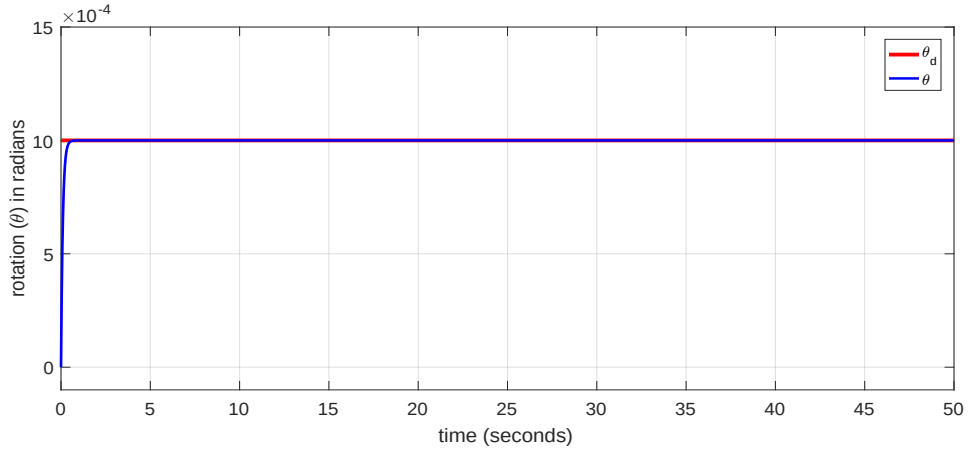

(23b) Slewing.

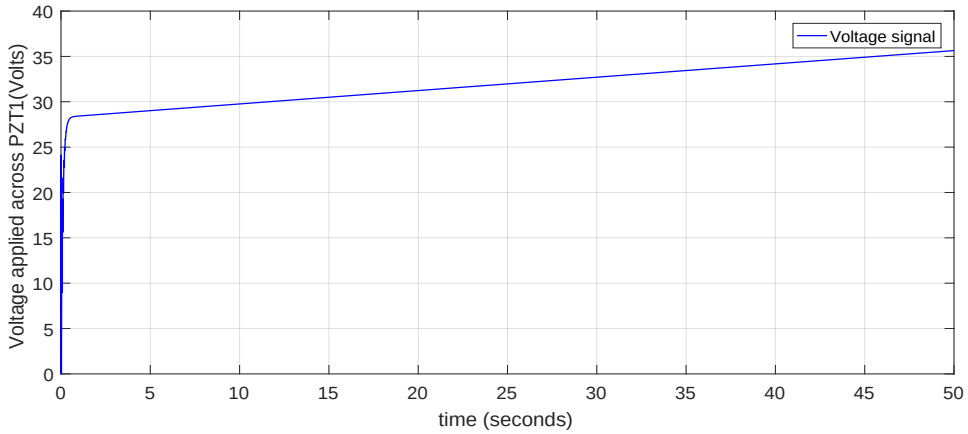

(23c) Control effort in Volts.

Figure 23: Slewing (Simulation) for $\delta = 0.0001$ using controller 2 with gains $\lambda = 10$, $K_\theta = 5$, $K_\xi = 5$.

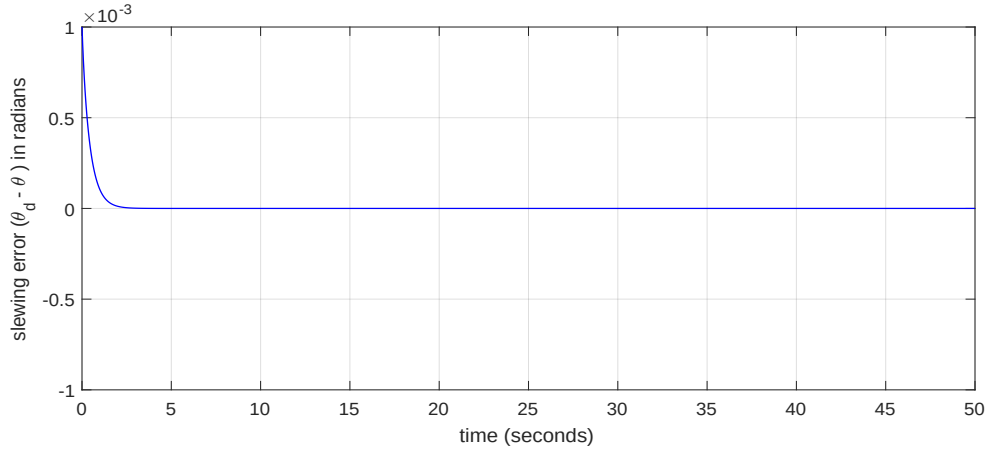

(24a) Slewing error.

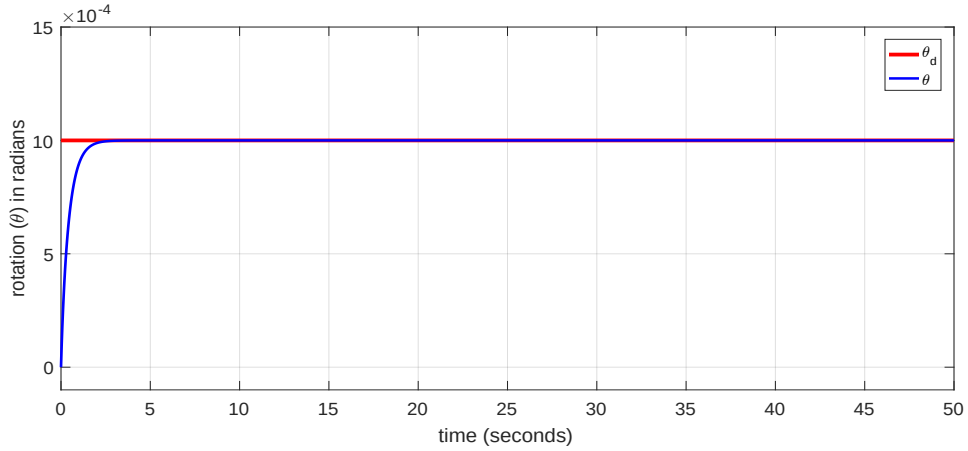

(24b) Slewing.

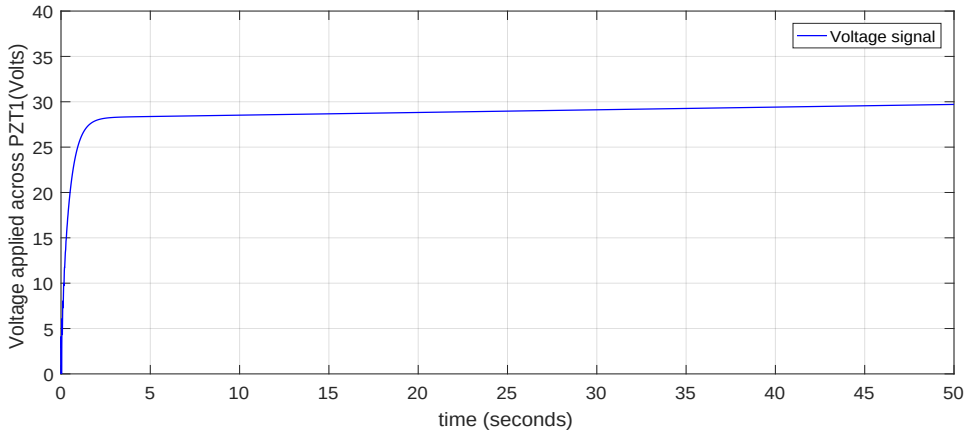

(24c) Control effort in Volts.

Figure 24: Slewing (Simulation) for $\delta = 1e-5$ using controller 2 with gains $\lambda = 3$, $K_\theta = 0.5$, $K_\xi = 0.5$.

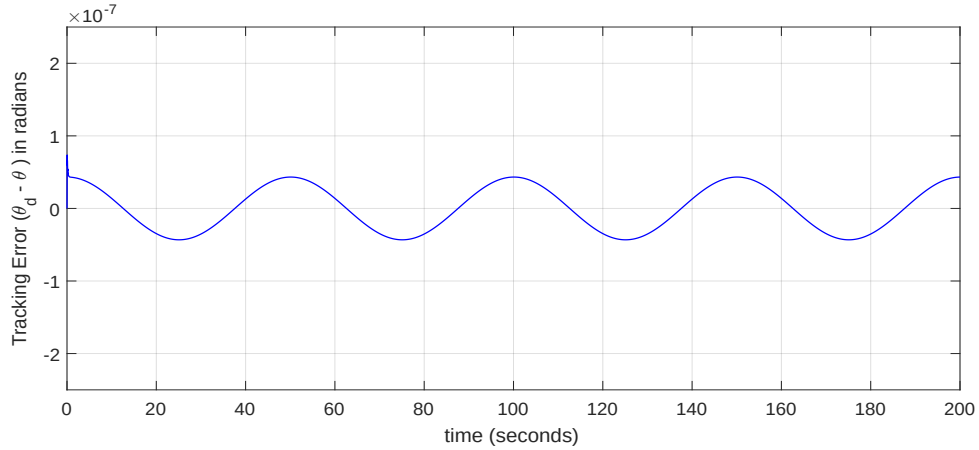

(25a) Tracking error.

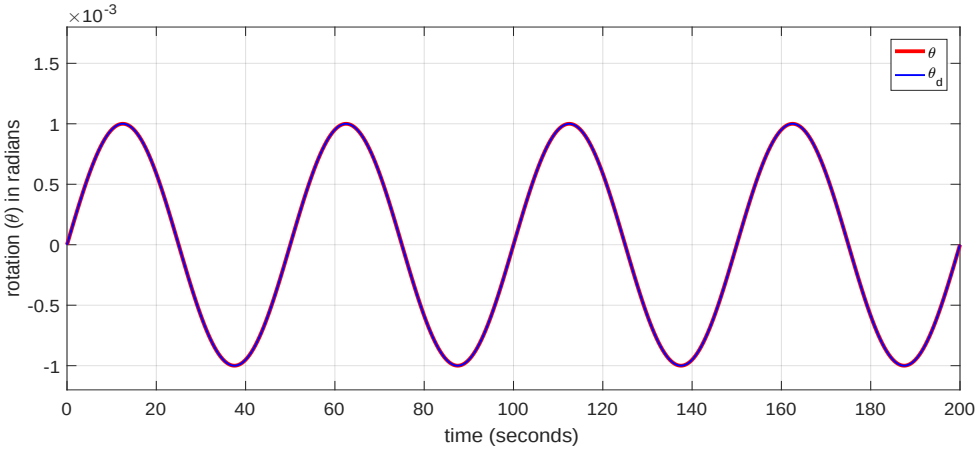

(25b) Trajectory tracking.

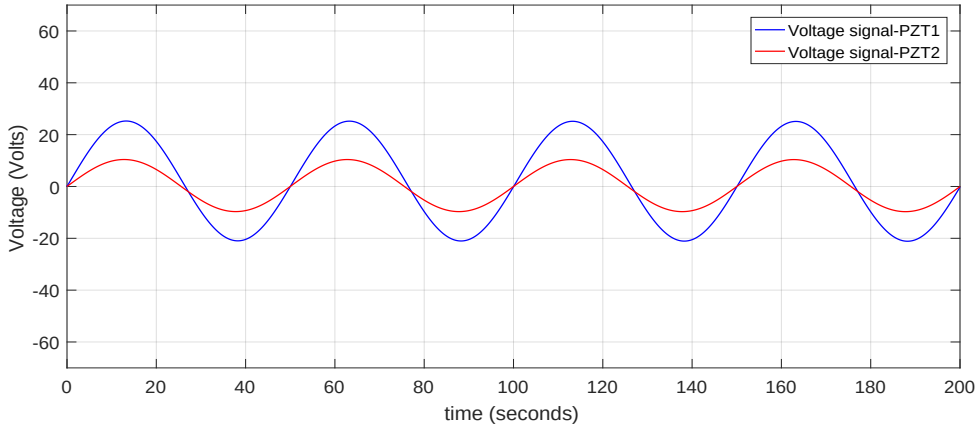

(25c) Control effort in Volts.

Figure 25: Trajectory tracking (Simulation) for $\delta = 0.0001$ using controller 2 distributed PZT (configuration 2) with gains $\lambda = 10$, $K_\theta = 5$, $K_\xi = 5$.

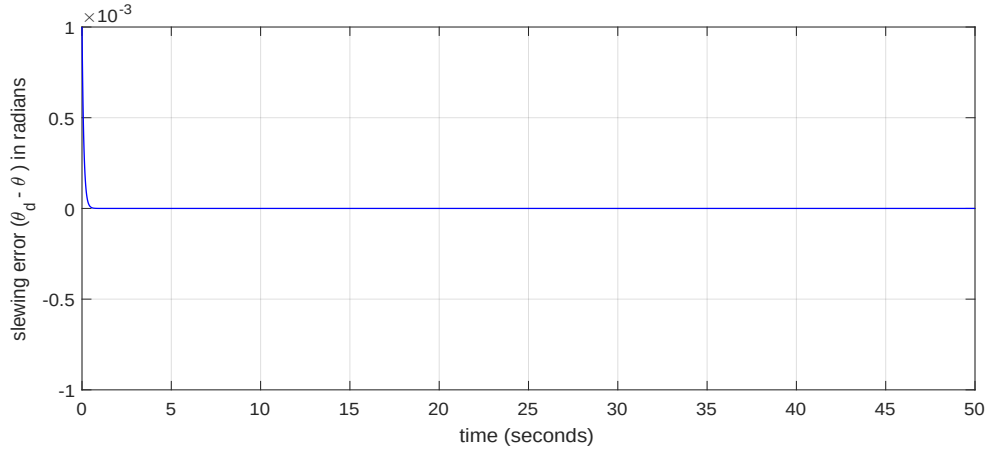

(26a) Slewing error.

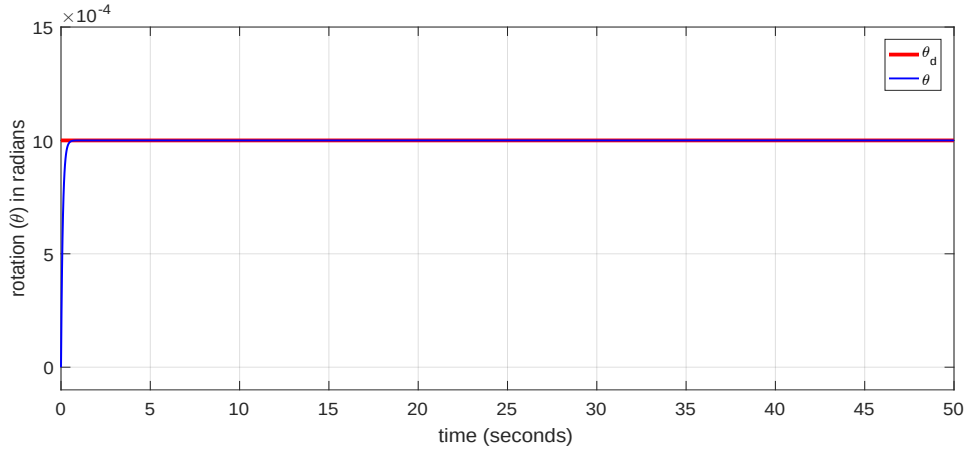

(26b) Slewing.

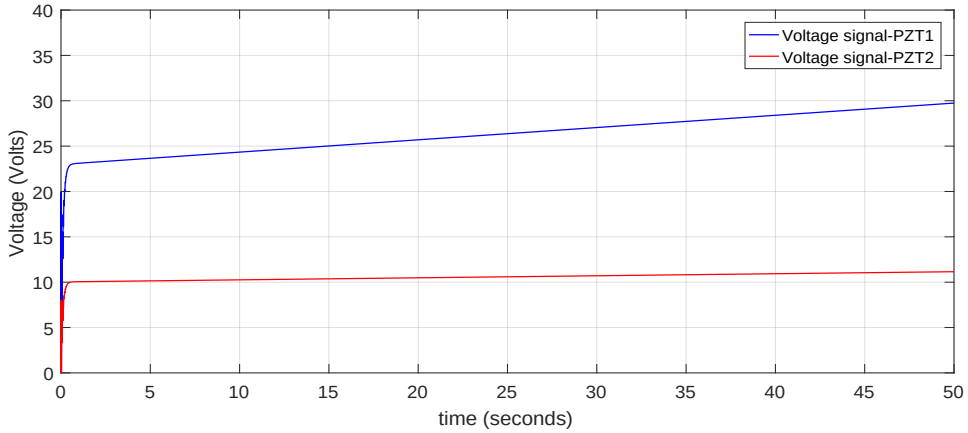

(26c) Control effort in Volts.

Figure 26: Slewing (Simulation) for $\delta = 0.0001$ using controller 2 distributed PZT (configuration 2) with gains $\lambda = 10$, $K_\theta = 5$, $K_\xi = 5$.

6 Experiments

6.1 Actuator Model Validation

The quasi-static actuator model in Eq. (22) is validated using a cantilever beam setup (see Fig. 27). The system parameters of the setup are given in Table 2, density of the beam and PZT are taken from Table 1. The dynamics of a cantilever beam in PDE form is given in Eq. (83) (see Ref. [15]). The Galerkin method was used to discretize the PDE equation to form the ODE in Eq. (84). In Figs. 28, we compare the open-loop response of the beam computed from simulations against results measured using the Vicon motion capture system during experiments at different location on the beam. For a sinusoidal input, the frequency of the simulated response matches experimental results. The amplitude of the response is not an exact match because 1) we assume there is perfect bonding between beam and PZT, 2) the beam is fixed at the root using a 'C-clamp', which is not an ideal cantilever beam, and 3) the Vicon marker effect on the beam is not is not modeled. We proceed and use this model in the real time experiments as the difference between the simulation and experiments can be compensated with extra control effort (it can be considered as a bounded uncertainty at the input of the system Eq. (34)).

$$m_R\ddot{\xi} + \left(EI\xi'' + \mu EI\dot{\xi}''\right)'' - M_b''(x,t) = 0 \tag{83}$$

$$\left(\int_0^{\ell_{ab}} m_R\phi\phi^T dx\right)\ddot{\eta} + \left(\int_0^{\ell_{ab}} \phi\left(EI\phi''^T\right)'' dx\right)(\eta + \mu\dot{\eta}) - \int_0^{\ell_{ab}} \phi M_b''(x,t)dx = 0 \tag{84}$$

Table 2: Beam geometrical parameters.

ℓ_{ba}	24.4×10^{-2} m	ℓ_{1pa}	0.9×10^{-2} m	ℓ_{pa}	7.244×10^{-2} m

(27a) Beam test setup.

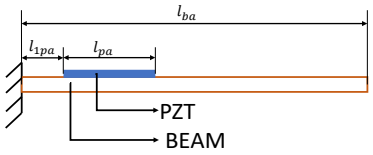

(27b) Beam schematic.

Figure 27: Beam Schematic and test setup with Vicon markers.

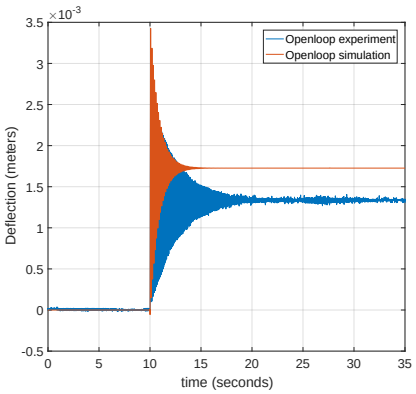

(28a) Response to step input.

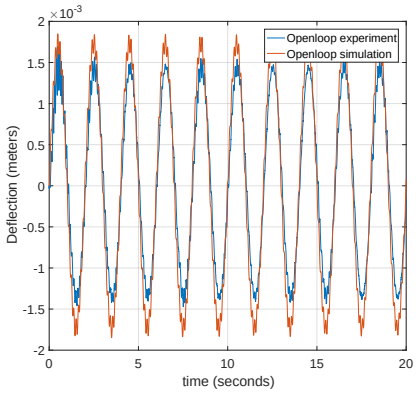

(28b) Response to a sinusoidal input.

Figure 28: Open-loop experiment vs simulation, tip deflection of the beam.

6.2 SASA Experimental Setup

The entire experimental setup is shown in Fig. 29, which includes SASA setup, Vicon system, amplifiers, and the controller. The top and side view of the SASA setup are shown in Fig. 30. The setup has a cylinder, a beam, and two plates. These components are machined to the dimensions specified in Figs. 31 and 32. The properties of the beam and PZT used are given in Table 1. The cylinder has a slot manufactured using wire cut Electrical discharge machining (EDM), through which beam is fitted

to the cylinder. The ball bearings are secured to the plates using an interference fit and the cylinder is press fit into the inner bearing race. The ball bearings are fitted at two vertical locations as a strategy to resist a torque perpendicular to the axis of the cylinder and to allow for rotation about axis of the cylinder. Here, we use T120-A4E-602 PZT sheet manufactured by Piezo Systems, Inc. with a maximum input voltage of $\pm 200V$. Two PZTs are bonded on each side of the beam using superglue[1] (the results obtained in the cantilever beam experiments use this bonding agent as well), for asymmetric actuation. Voltage is supplied to the PZTs using a Humusoft MF624 controller, which can produce up to $\pm 10V$. We use linear amplifiers manufactured by Piezo systems to amplify the voltage supplied by the controller before applying it across the PZTs. The real-time code for experiment was setup in MATLAB using Simulink® Desktop real-time™ toolbox. For computation of derivatives and integrals we used the discrete time function blocks[2] available in Simulink®. The flowchart in Fig. 35 shows the flow of real-time implementation. As seen in Fig. 35, we use three Vicon cameras to measure the beam deflection and rotation of the cylinders. The Simulink implementation for Vicon system is taken from Ref. [35]. The Vicon system communicates with the controller (computer with the Humusoft controller) using a local wireless area network.

[1] Loctite® Super Glue

[2] http://www.mathworks.com/help/simulink/discrete.html

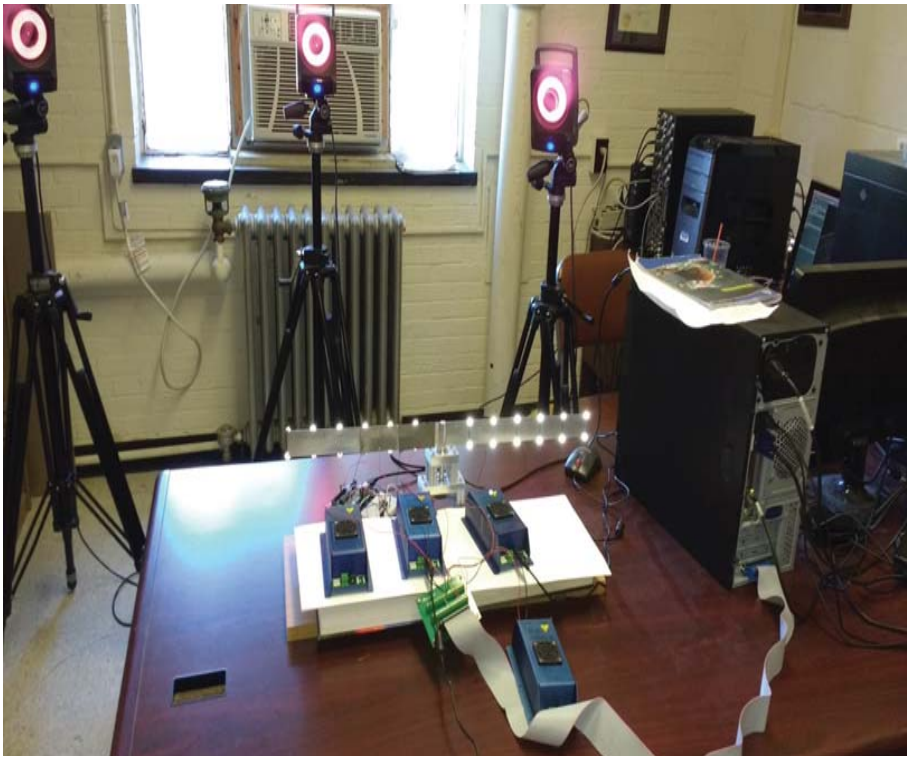

Figure 29: SASA experimental setup.

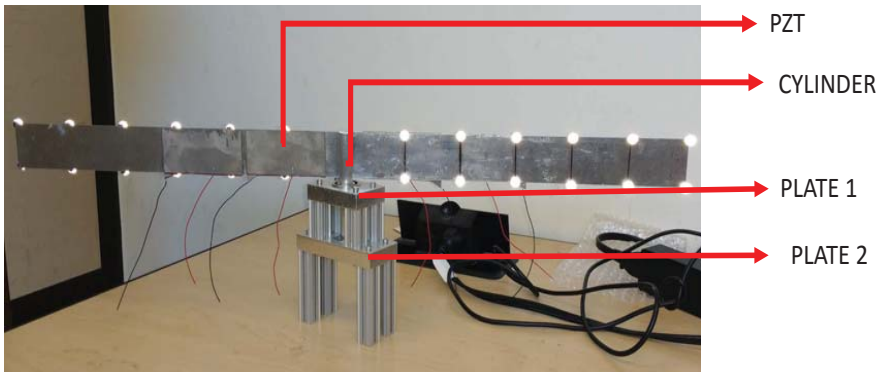

(30a) Side view.

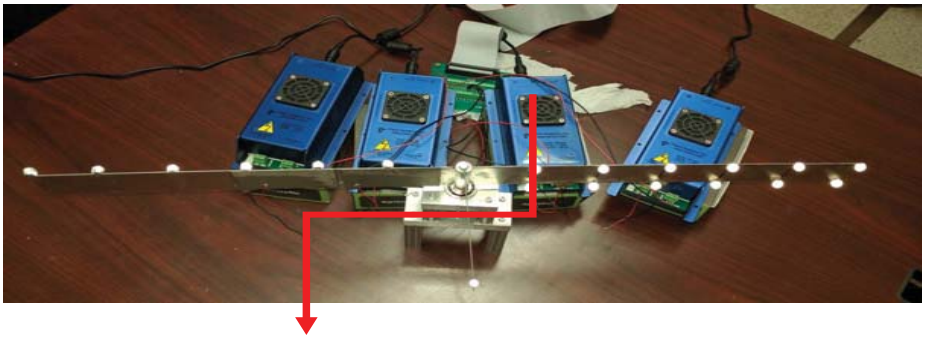

(30b) Top view with amplifiers.

Figure 30: SASA setup views.

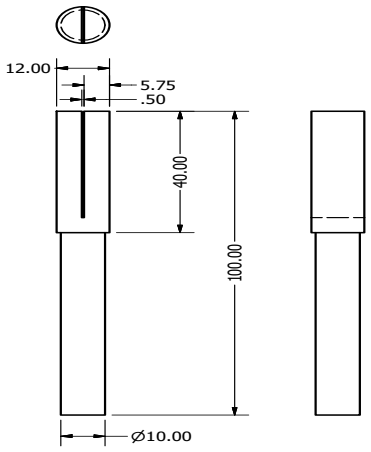

Figure 31: Cylinder projections.

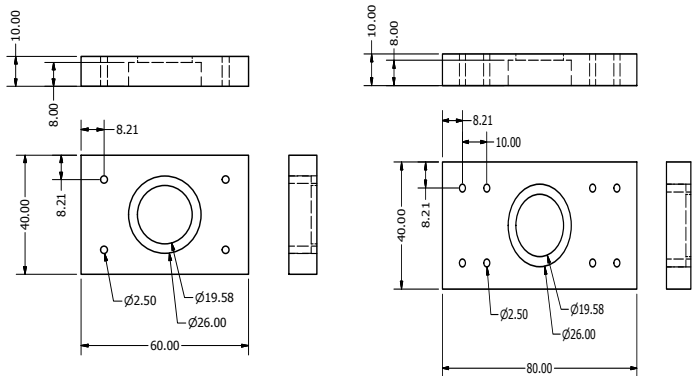

(32a) Plate 1. **(32b) Plate 2.**

Figure 32: Plates used for support.

The properties in Table 1 are estimated using physical properties of the Aluminum beam, cylinder, and steel ball bearings. The experimental system is built to be symmetric so that we can use measurements from a single beam to compute control effort during the real-time experiments. To use the dynamics and control laws derived, we transform the Vicon system's world coordinate system e_{a_1}, e_{a_2} to an inertial coordinate system fixed to the center of the cylinder e_{c_1}, e_{c_2}. The location of the center of the cylinder is determined using the Vicon system by a hit and trial method. This point is marked with a Vicon marker for further experiments. The angle 'α' can also be inferred from Vicon measurements without actuation. Note that in Figs. 7, 29, and 33, there are 12 Vicon markers at 6 locations on each beam. The Vicon system calculates x, y coordinates of these Vicon markers with respect to coordinate system e_{c_1}, e_{c_2}. The deflection at the 6 Vicon marker locations is computed by solving an inverse kinematic problem Eq. (85), where 'θ' is measured using the Vicon marker as shown in Fig. 33.

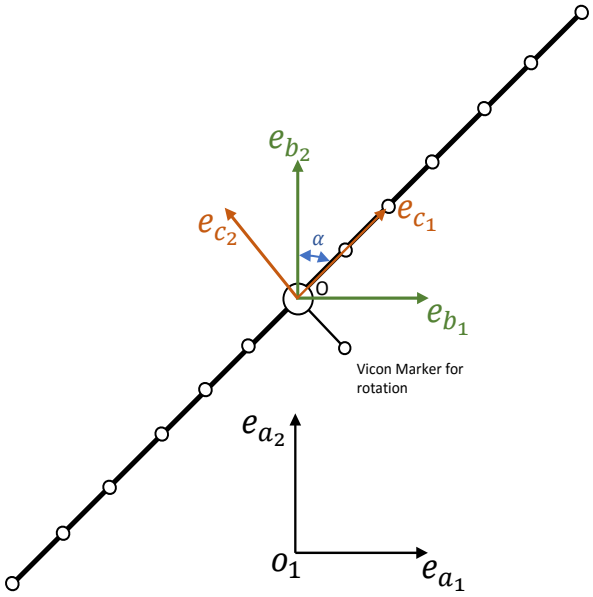

Figure 33: Top view of the setup showing coordinate systems used in experiments.

$$\begin{bmatrix} r+x \\ \xi \end{bmatrix} = \begin{bmatrix} \cos(\theta) & \sin(\theta) \\ -\sin(\theta) & \cos(\theta) \end{bmatrix} \begin{bmatrix} x \\ y \end{bmatrix} \tag{85}$$

Let the deflection measured at the 6 Vicon marker locations (with distances from root $[\ell_{v_1}\ \ell_{v_2}\ \ell_{v_3}\ \ell_{v_4}\ \ell_{v_5}\ \ell_{v_6}]$) using the Vicon system be $\xi_{exp} = [\xi_1\ \xi_2\ \xi_3\ \xi_4\ \xi_5\ \xi_6]$. The ξ_{exp} is used to compute η for 4 Galerkin functions Eq. (86). The derivatives $\dot{\theta}$ and $\dot{\eta}$ are estimated using discrete derivatives of the computed θ and η from Vicon measurements.

$$\xi_{exp}^{T} = \begin{bmatrix} \phi_1(\ell_{v_1}) & \phi_2(\ell_{v_1}) & \phi_3(\ell_{v_1}) & \phi_4(\ell_{v_1}) \\ \phi_1(\ell_{v_2}) & \phi_2(\ell_{v_2}) & \phi_3(\ell_{v_2}) & \phi_4(\ell_{v_2}) \\ \phi_1(\ell_{v_3}) & \phi_2(\ell_{v_3}) & \phi_3(\ell_{v_3}) & \phi_4(\ell_{v_3}) \\ \phi_1(\ell_{v_4}) & \phi_2(\ell_{v_4}) & \phi_3(\ell_{v_4}) & \phi_4(\ell_{v_4}) \\ \phi_1(\ell_{v_5}) & \phi_2(\ell_{v_5}) & \phi_3(\ell_{v_5}) & \phi_4(\ell_{v_5}) \\ \phi_1(\ell_{v_6}) & \phi_2(\ell_{v_6}) & \phi_3(\ell_{v_6}) & \phi_4(\ell_{v_6}) \end{bmatrix} \eta \tag{86}$$

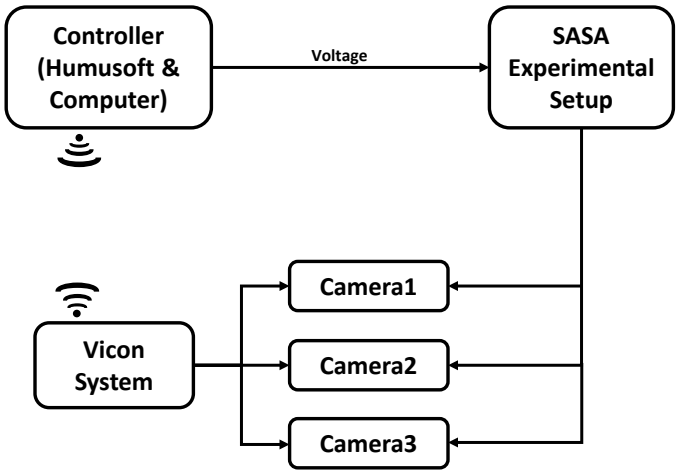

Figure 34: Schematic of SASA test setup.

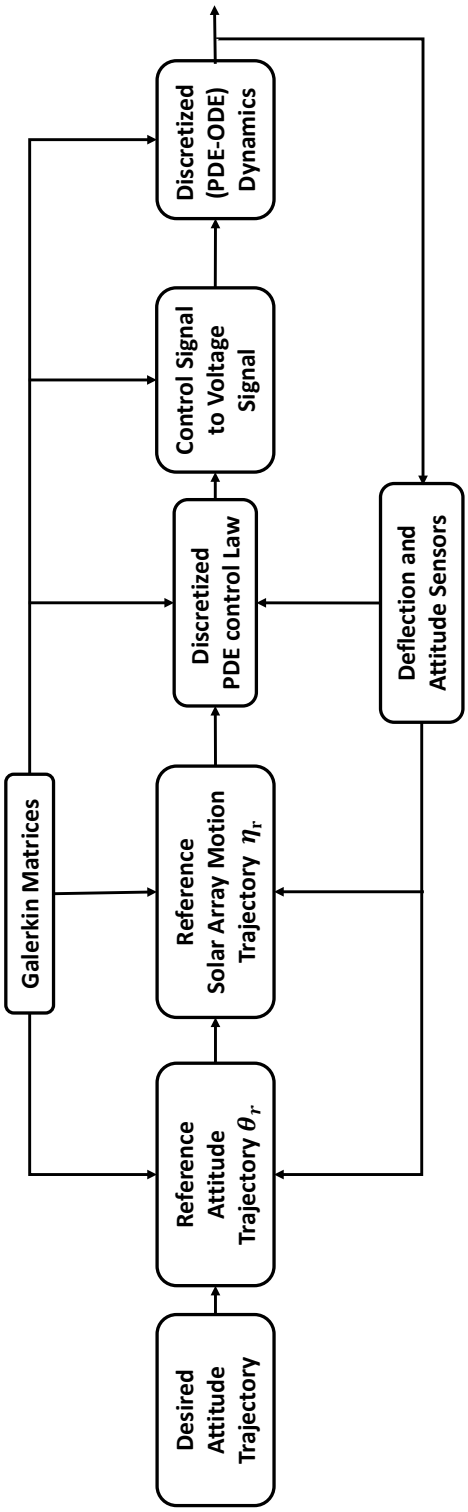

Figure 35: closed-loop ODE system as implemented in Simulink for experiments.

6.3 SASA Open-loop Simulation vs Experiments

For the open-loop results, we measure the hub rotation due to an applied voltage across PZT on the beam. The estimation errors are clearly seen in Figs. 36 and 37, which illustrates a comparison of open-loop simulation and experiment. The response to a sinusoidal input is a good match. For the step input, simulations predict larger rotation. This difference is due to the estimation of system parameters and not modelling the ball bearing friction. In spite of the modeling errors, the closed-loop system achieves the control objectives (see Section. 6.4 for details).

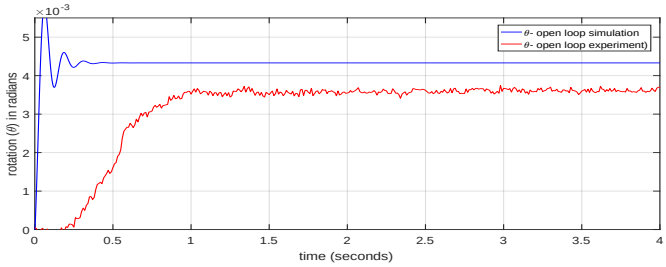

(36a) Response to step input of 160 volts.

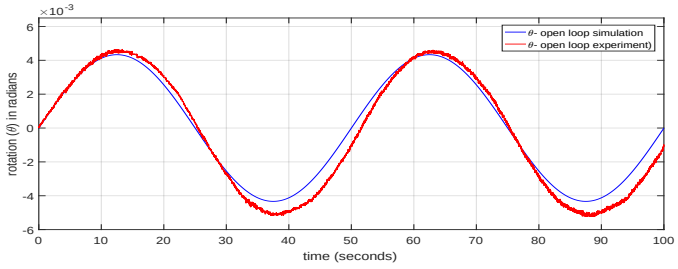

(36b) Response to a sinusoidal input of amplitude 160 V and 0.02 Hz.

Figure 36: Open-loop experiment vs simulation, cylinder rotation for 160 Volts amplitude inputs.

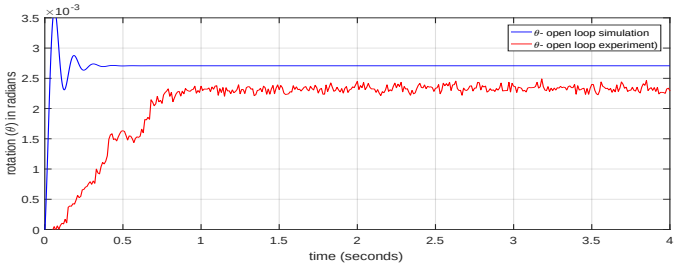

(37a) Response to step input of 100 volts.

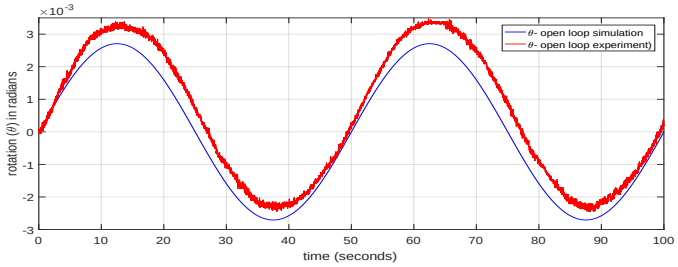

(37b) Response to a sinusoidal input of amplitude 100 V and 0.02 Hz.

Figure 37: Open-loop experiment vs simulation, cylinder rotation for 100 Volts amplitude inputs.

6.4 Results

The experimental setup described above, is used to test the two control laws. Based on the simulation results, we test controller 1 in configuration 1 for $\delta = \{1, 0.5, 0\}$ (Figs. 38–45) and in configuration 2 for $\delta = \{0.5, 0\}$ (Figs. 44–47). Controller 2 was only tested for $\delta = 0.0001$ (Fig. 48-51) as it was observed that for values of 'δ' closer to 1 it induces oscillations and saturates the actuator. Similar to the simulation, we track a sinusoidal signal of amplitude 0.001 radians, with a frequency of 0.02Hz, and slew to 0.001 radians from a zero initial angle. As mentioned earlier, the real-time code was setup using Simulink Desktop real-time toolbox. For all the 'δ' mentioned earlier we achieve the control objectives. As Matlab is a single-threaded application, the measurements are made and control signal is applied to PZT's at the same frequency (100 Hz) during the experiment. For controller 1 in configuration 2, the PZTs on

each side become more active as 'δ' value is reduced to 0. Note that the controllers work inspite of the modelling errors and parametric uncertainties. The control effort computed by the control algorithm during experiments is atleast 20 Volts more than predicted during simulations.

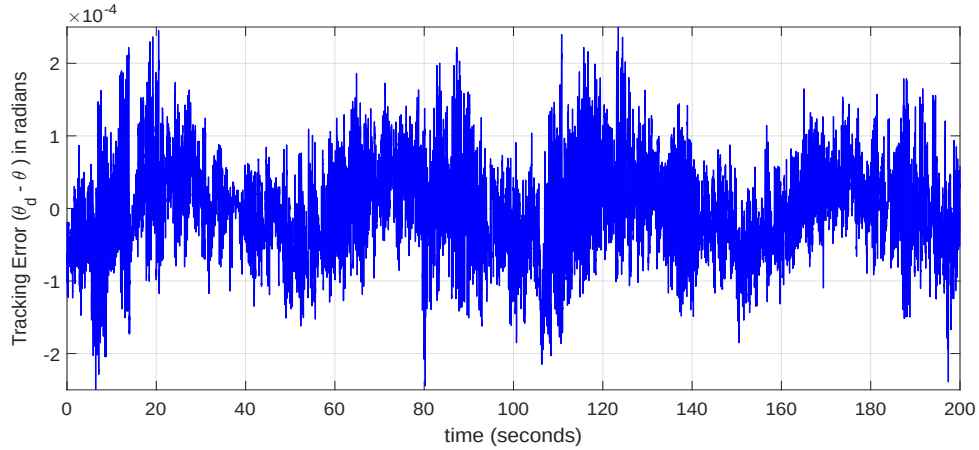

(38a) Tracking error.

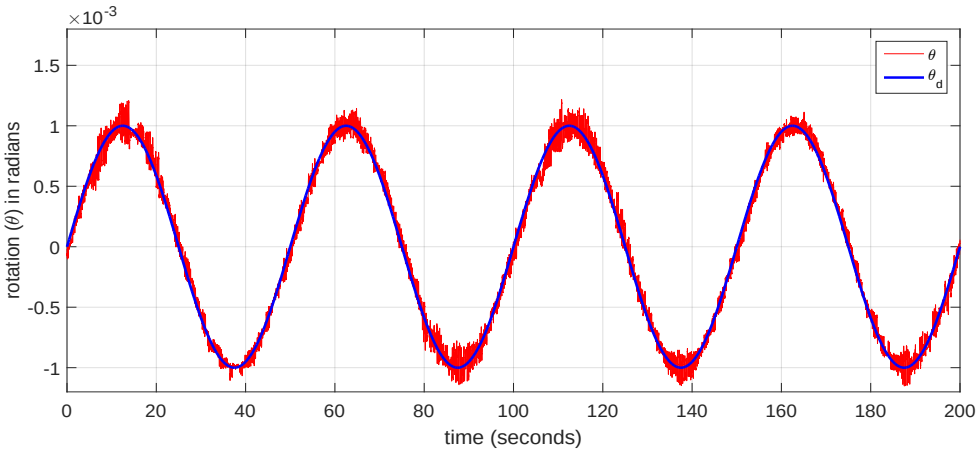

(38b) Trajectory tracking.

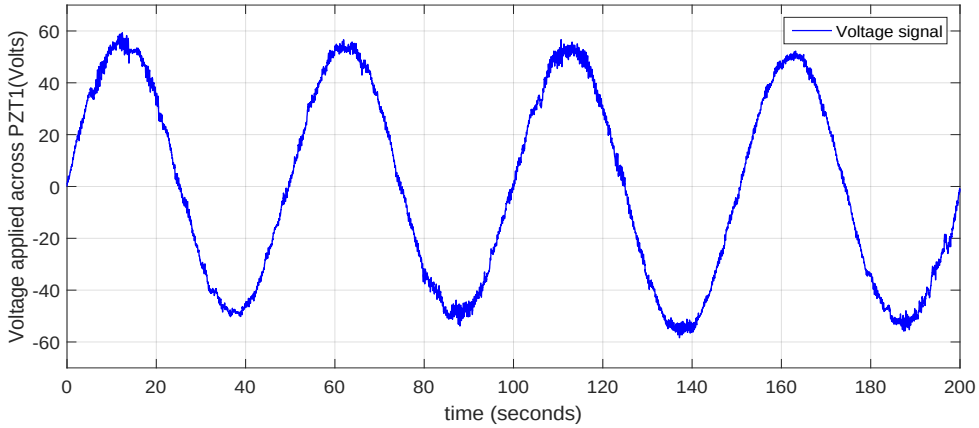

(38c) Control effort in Volts.

Figure 38: Trajectory tracking (Experiment) for $\delta = 1$ using controller 1 with gains $\lambda = 1.5$, $K_\theta = 0.5$, $K_\xi = 0.5$.

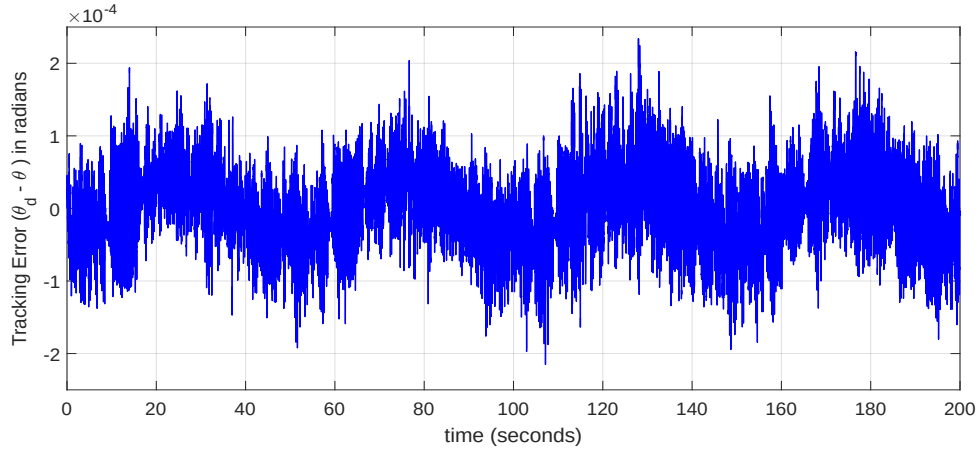

(39a) Tracking error.

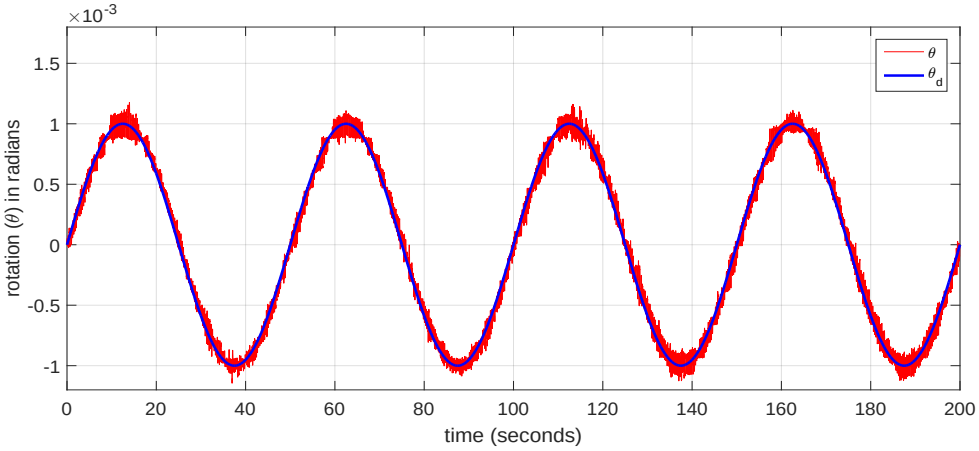

(39b) Trajectory tracking.

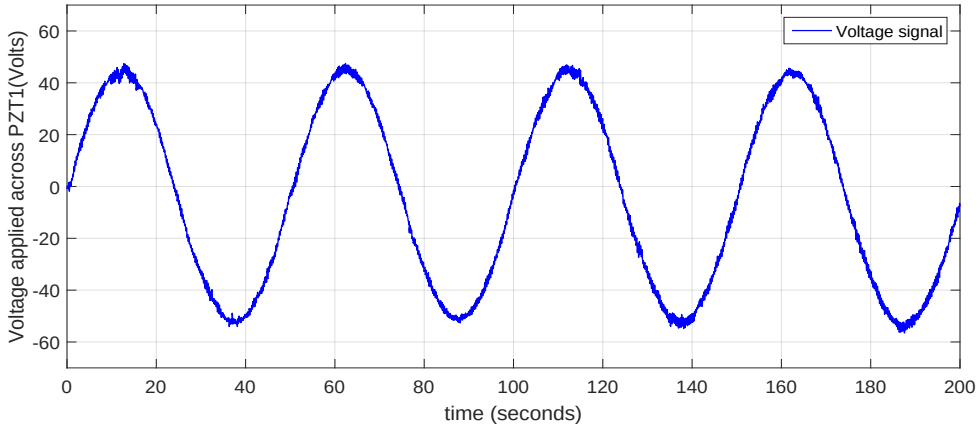

(39c) Control effort in Volts.

Figure 39: Trajectory tracking (Experiment) for $\delta = 0.5$ using controller 1 with gains $\lambda = 1.5$, $K_\theta = 0.5$, $K_\xi = 0.5$.

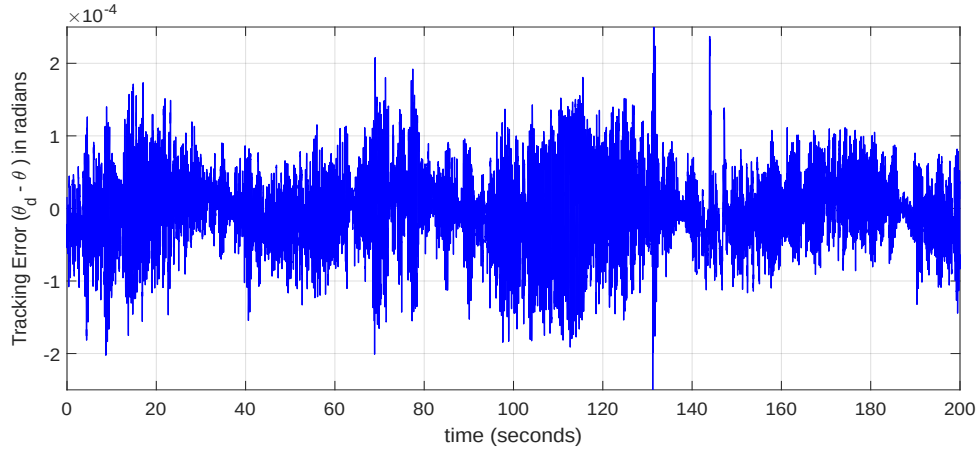

(40a) Tracking error.

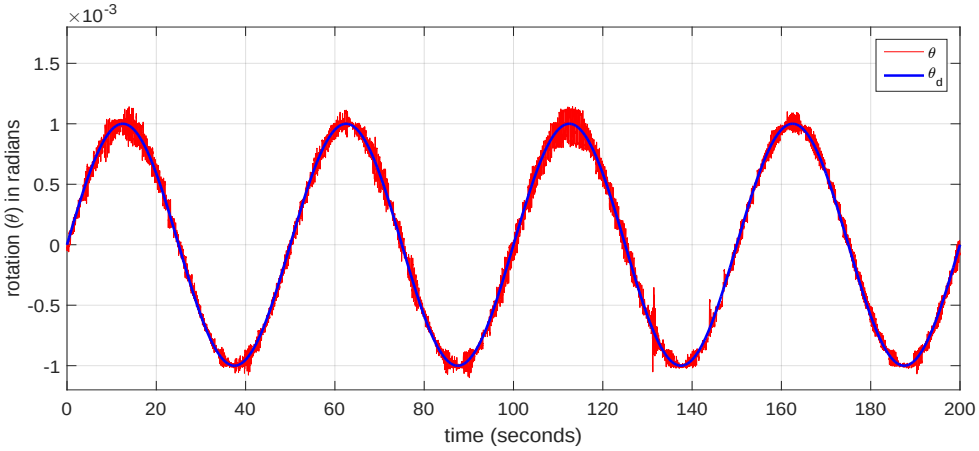

(40b) Trajectory tracking.

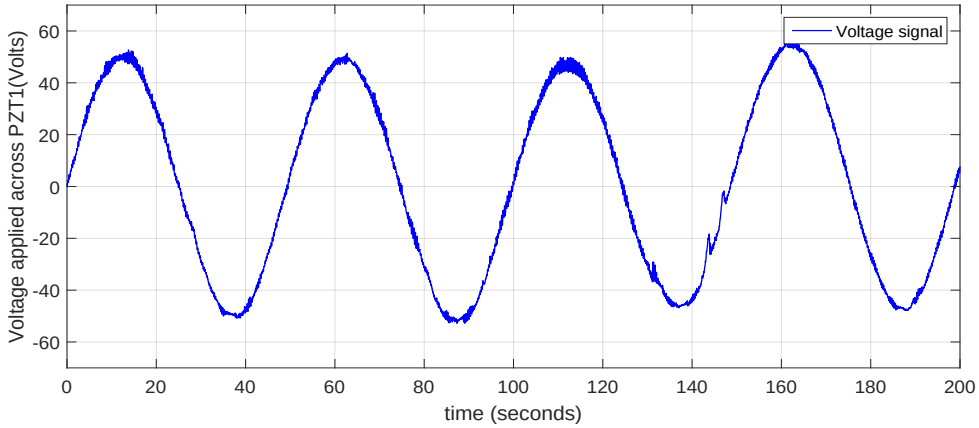

(40c) Control effort in Volts.

Figure 40: Trajectory tracking (Experiment) for $\delta = 0$ using controller 1 with gains $\lambda = 2$, $K_\theta = 0.5$, $K_\xi = 0.5$.

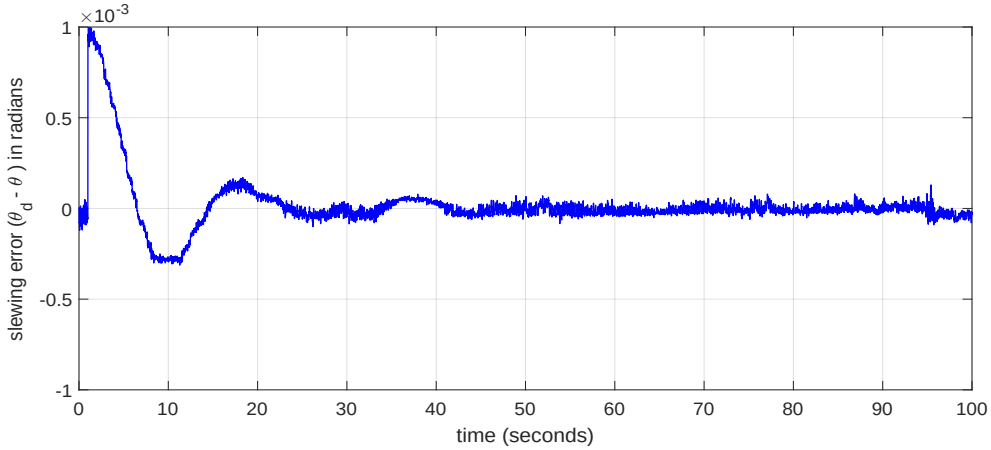

(41a) Slewing error.

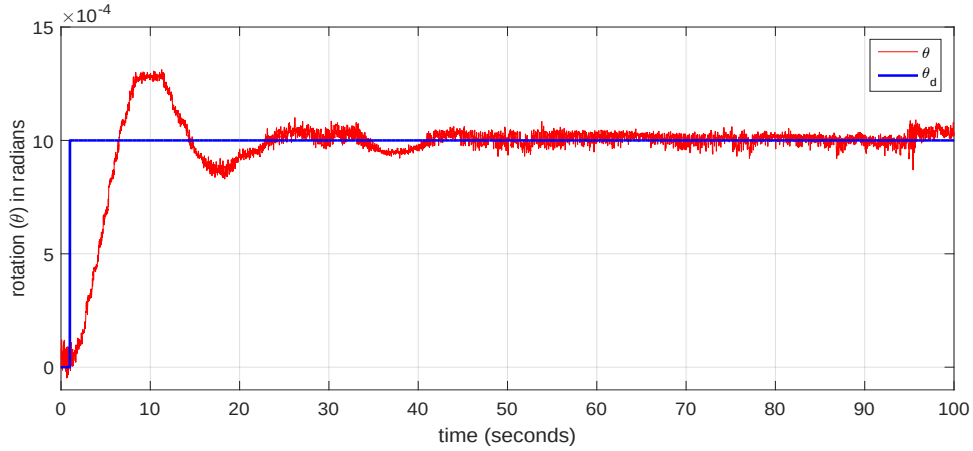

(41b) Slewing.

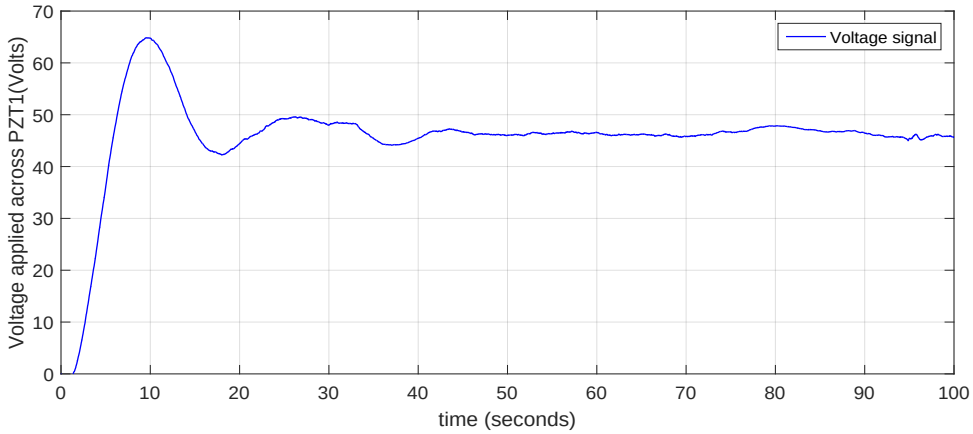

(41c) Control effort in Volts.

Figure 41: Slewing (Experiment) for $\delta = 1$ using controller 1 with gains $\lambda = 1$, $K_\theta = 0.25$, $K_\xi = 0.5$.

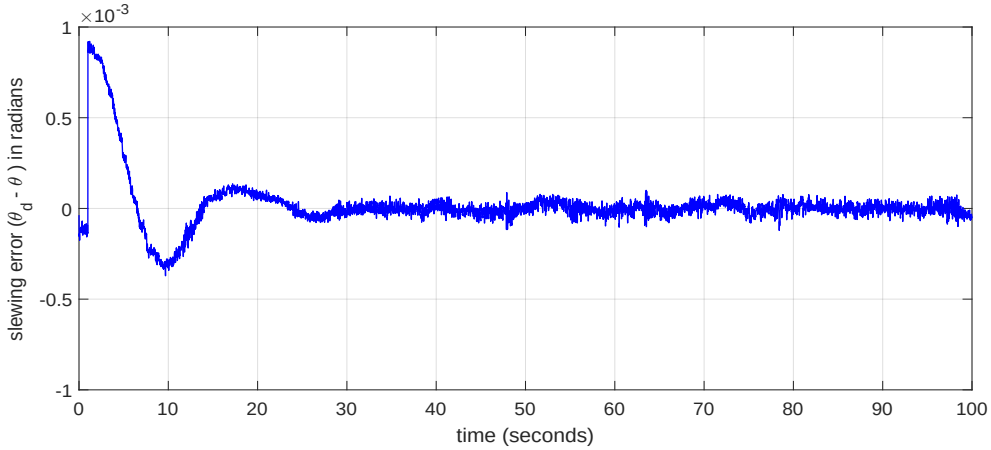

(42a) Slewing error.

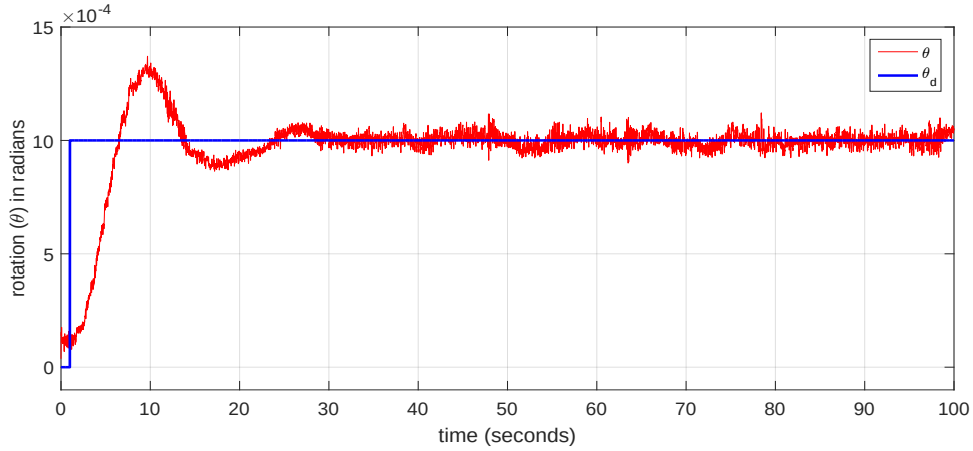

(42b) Slewing.

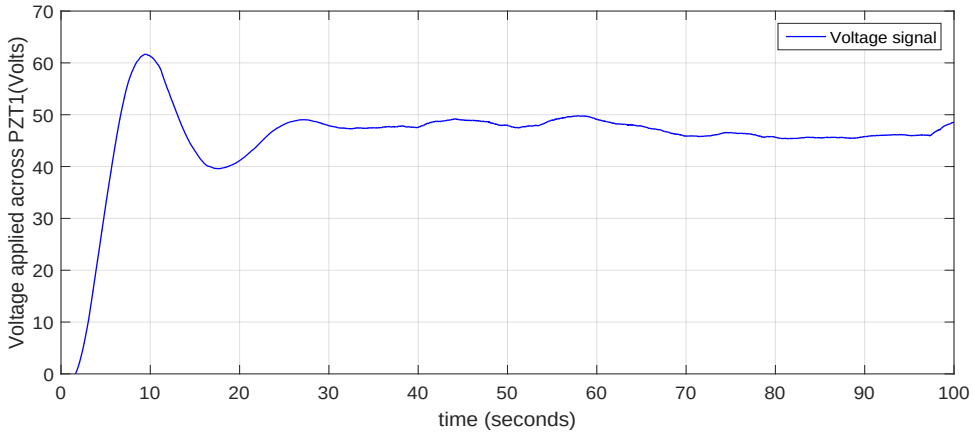

(42c) Control effort in Volts.

Figure 42: Slewing (Experiment) for $\delta = 0.5$ using controller 1 with gains $\lambda = 1$, $K_\theta = 0.25$, $K_\xi = 0.5$.

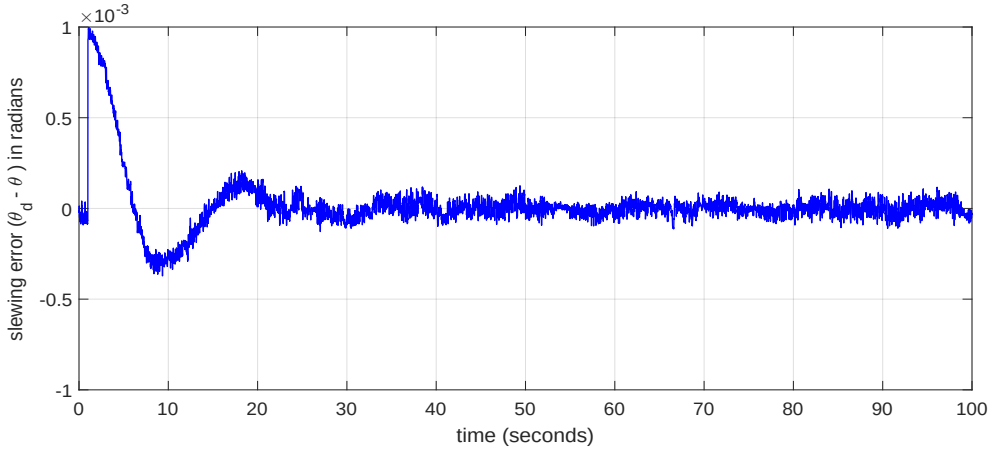

(43a) Slewing error.

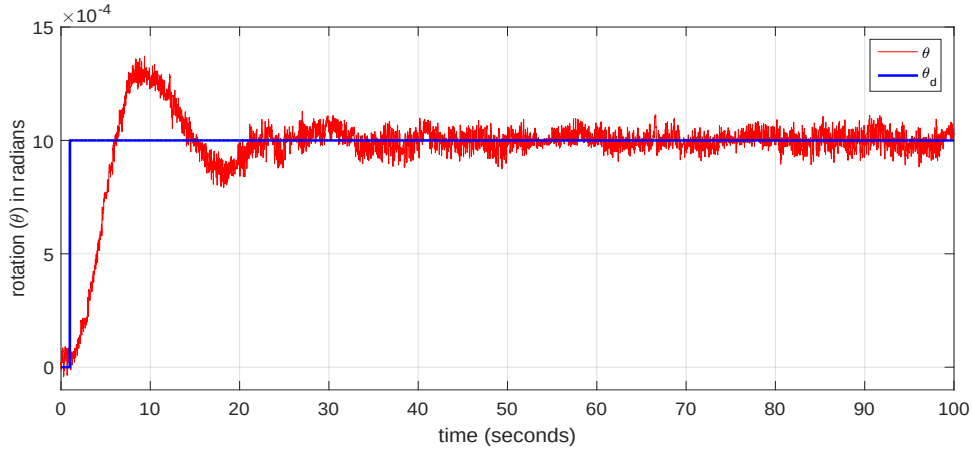

(43b) Slewing.

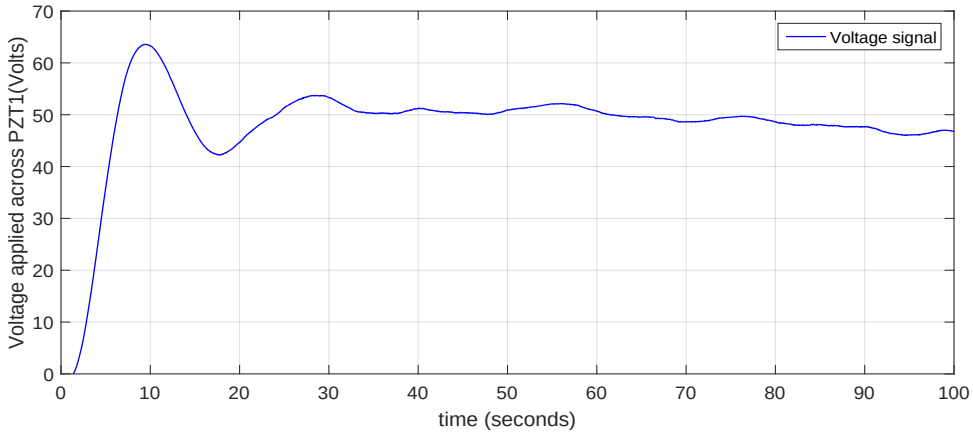

(43c) Control effort in Volts.

Figure 43: Slewing (Experiment) for $\delta = 0$ using controller 1 with gains $\lambda = 1$, $K_\theta = 0.25$, $K_\xi = 0.5$.

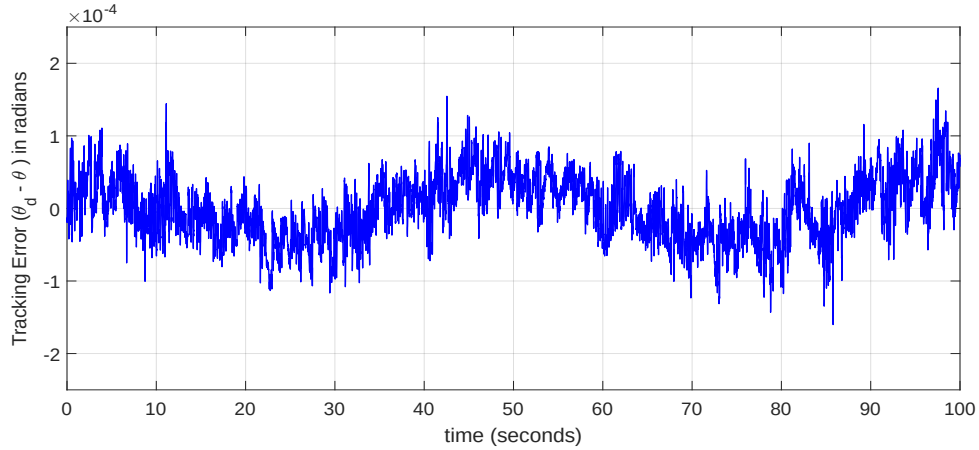

(44a) Tracking error.

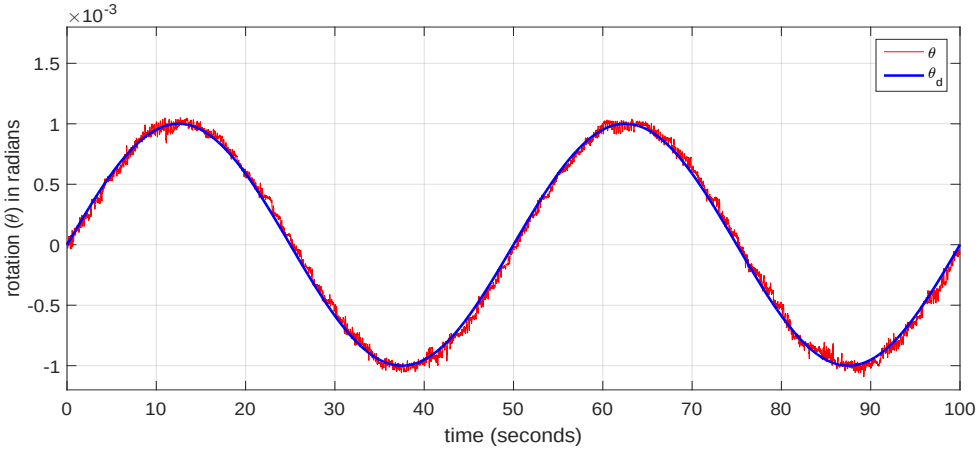

(44b) Trajectory tracking.

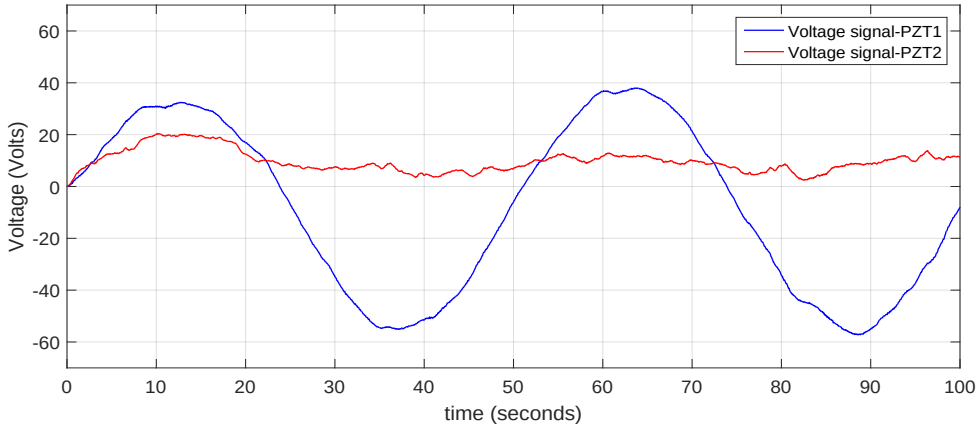

(44c) Control effort in Volts.

Figure 44: Trajectory tracking (Experiment) for $\delta = 0.5$ using controller 1 distributed PZT (configuration 2) with gains $\lambda = 2$, $K_\theta = 0.5$, $K_\xi = 0.5$.

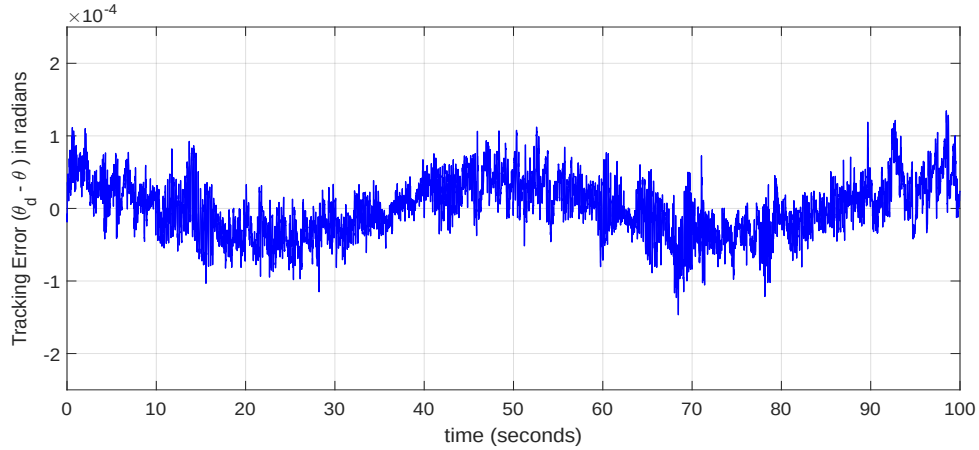

(45a) Tracking error.

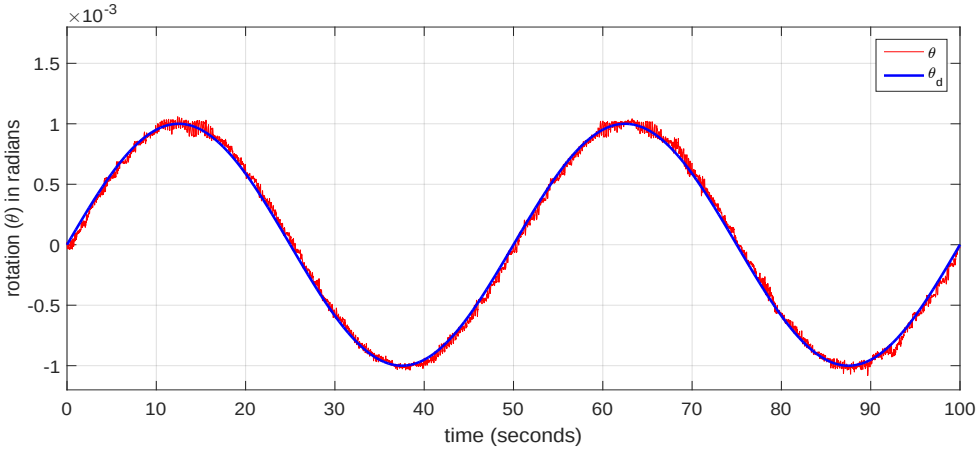

(45b) Trajectory tracking.

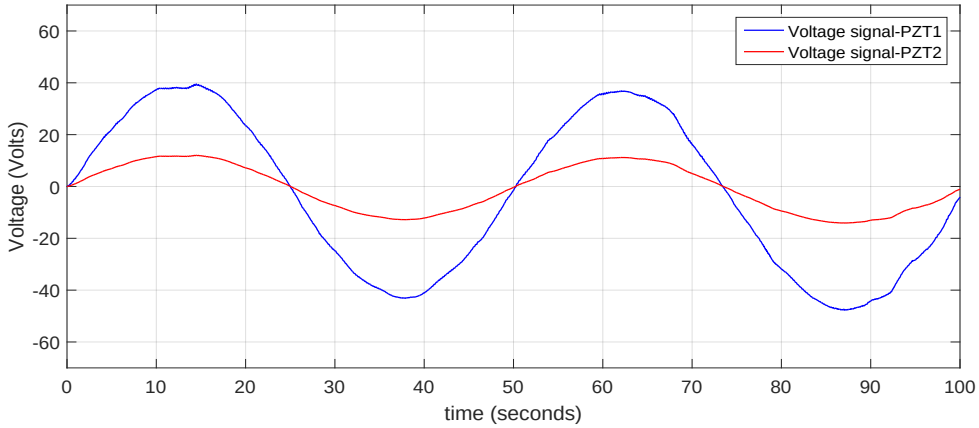

(45c) Control effort in Volts.

Figure 45: Trajectory tracking (Experiment) for $\delta = 0$ using controller 1 distributed PZT (configuration 2) with gains $\lambda = 2$, $K_\theta = 0.5$, $K_\xi = 0.5$.

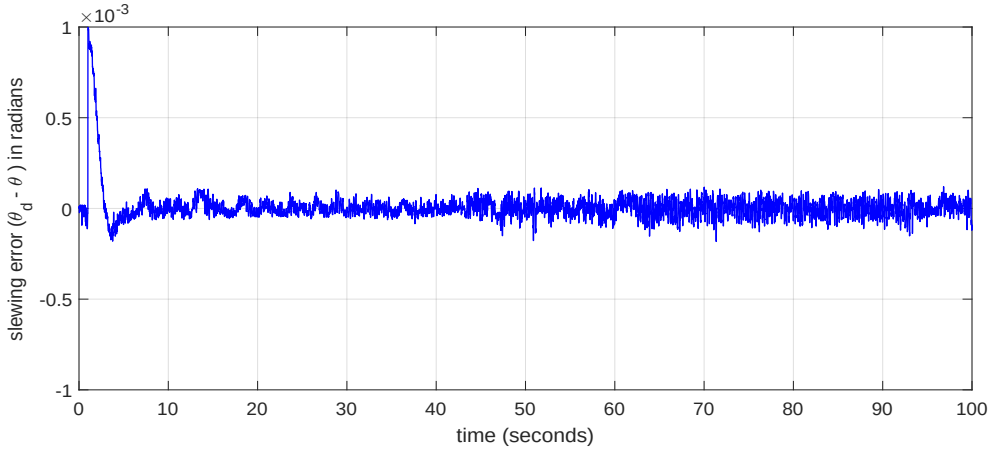

(46a) Slewing error.

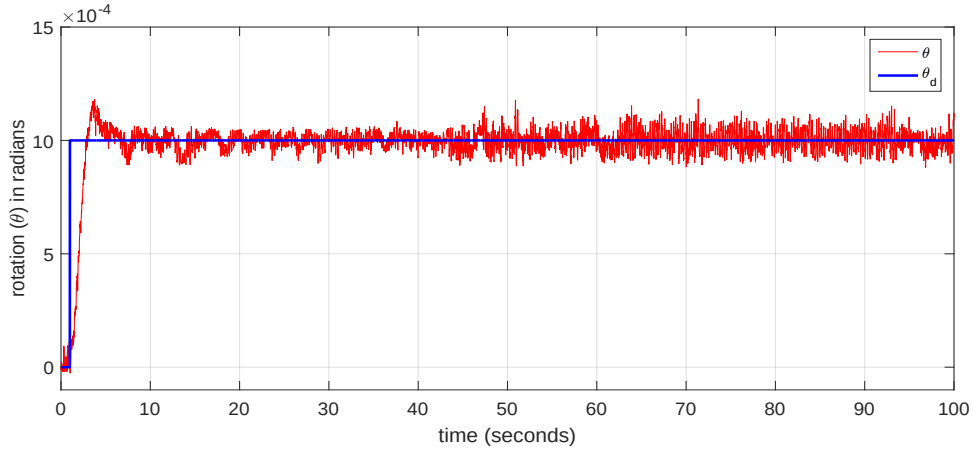

(46b) Slewing.

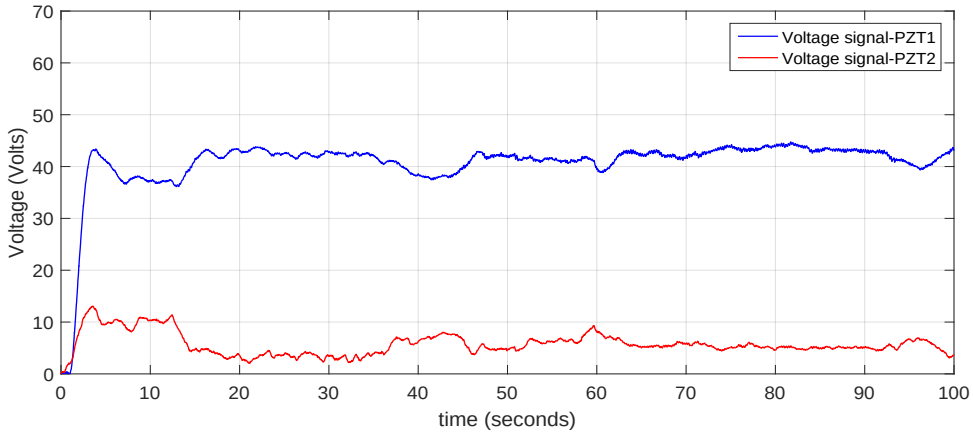

(46c) Control effort in Volts.

Figure 46: Slewing (Experiment) for $\delta = 0.5$ using controller 1 distributed PZT (configuration 2) with gains $\lambda = 2$, $K_\theta = 0.5$, $K_\xi = 0.5$.

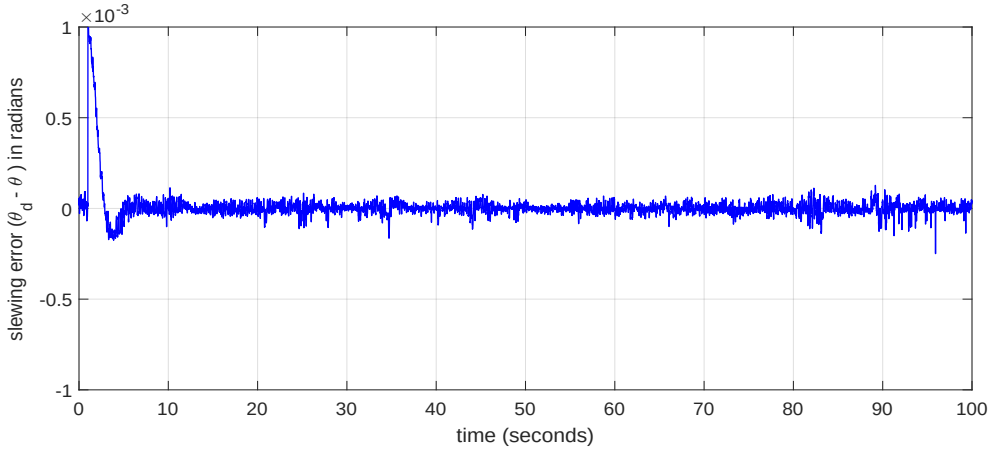

(47a) Slewing error.

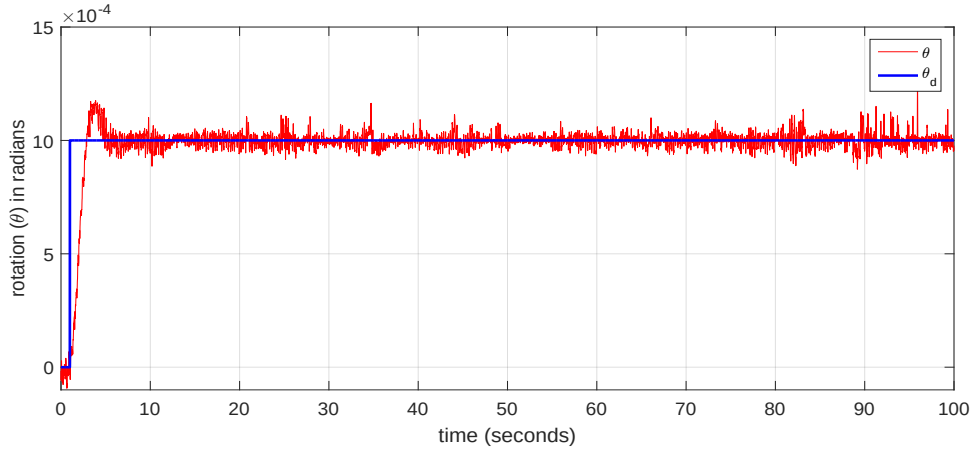

(47b) Slewing.

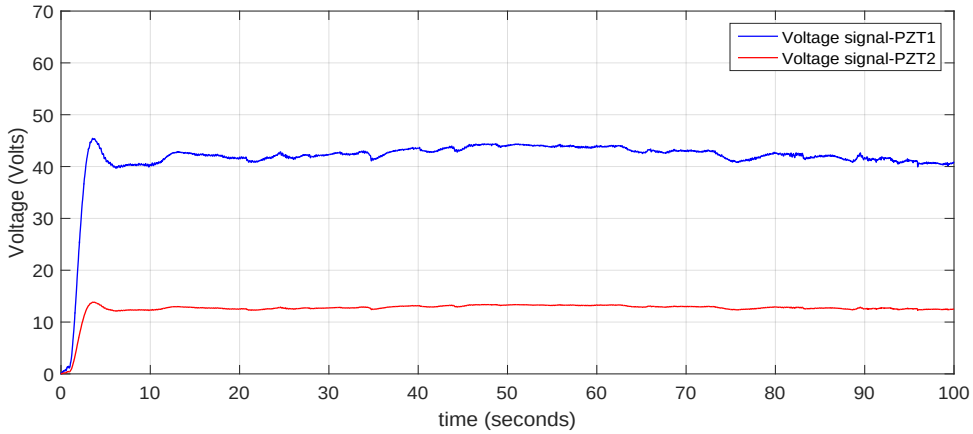

(47c) Control effort in Volts.

Figure 47: Slewing (Experiment) for $\delta = 0$ using controller 1 with gains distributed PZT (configuration 2) $\lambda = 2$, $K_\theta = 0.5$, $K_\xi = 0.5$.

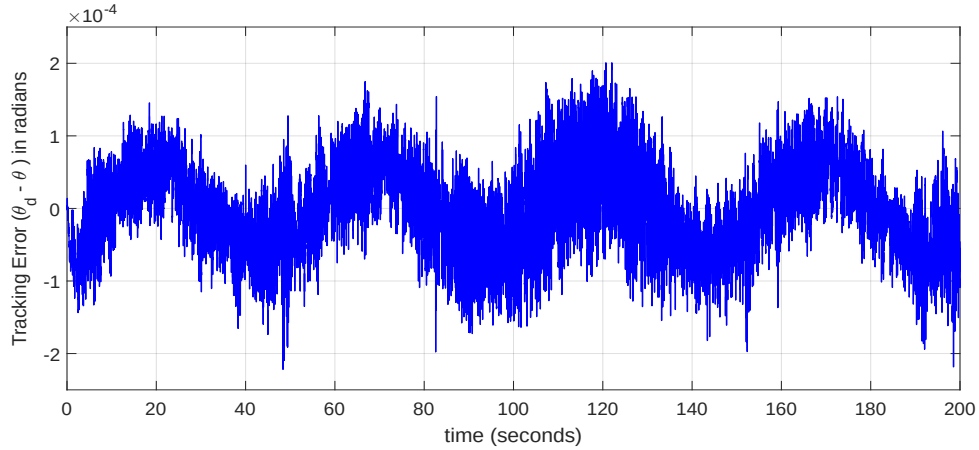

(48a) Tracking error.

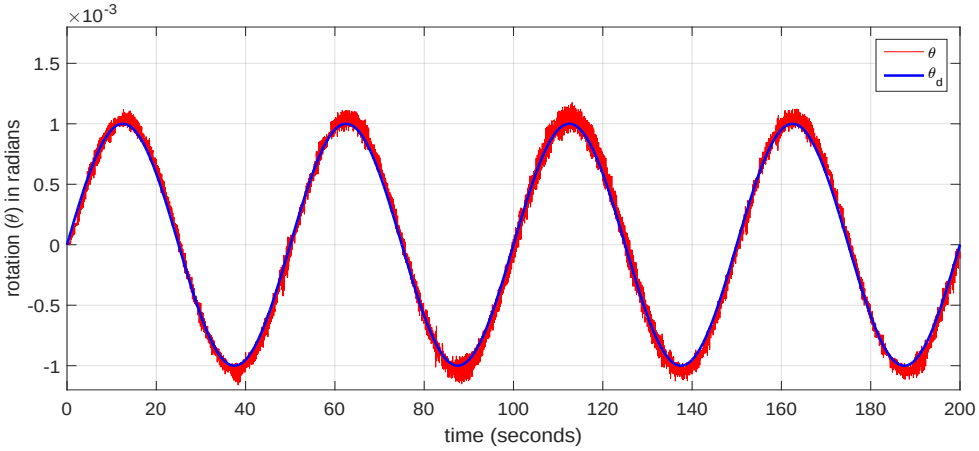

(48b) Trajectory tracking.

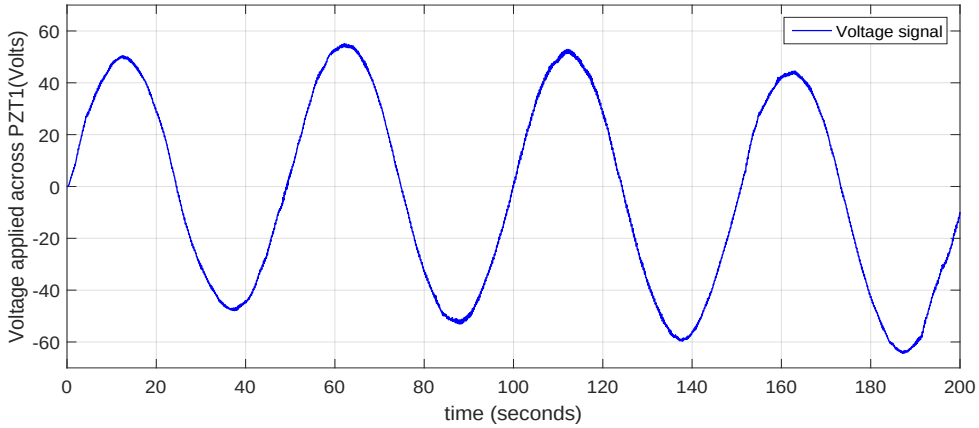

(48c) Control effort in Volts.

Figure 48: Trajectory tracking (Experiment) for $\delta = 0.0001$ using controller 2 with gains $\lambda = 1$, $K_\theta = 0.5$, $K_\xi = 0.5$.

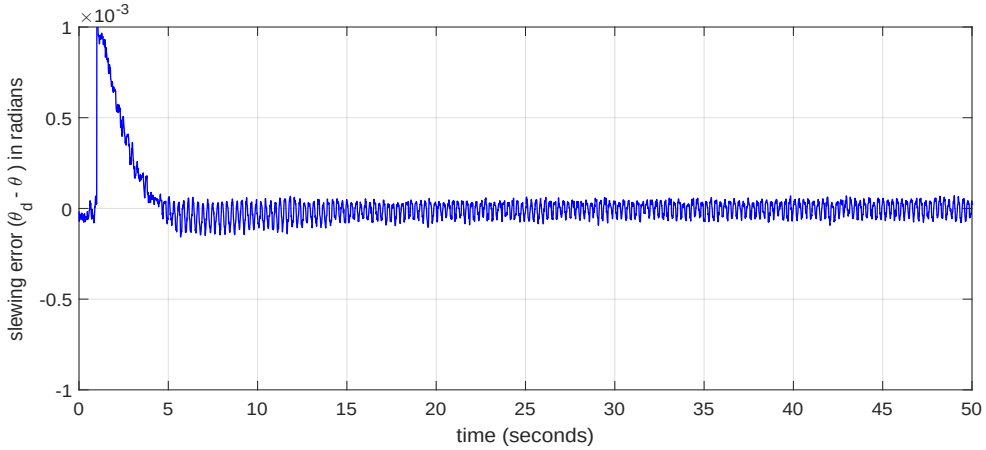

(49a) Slewing error.

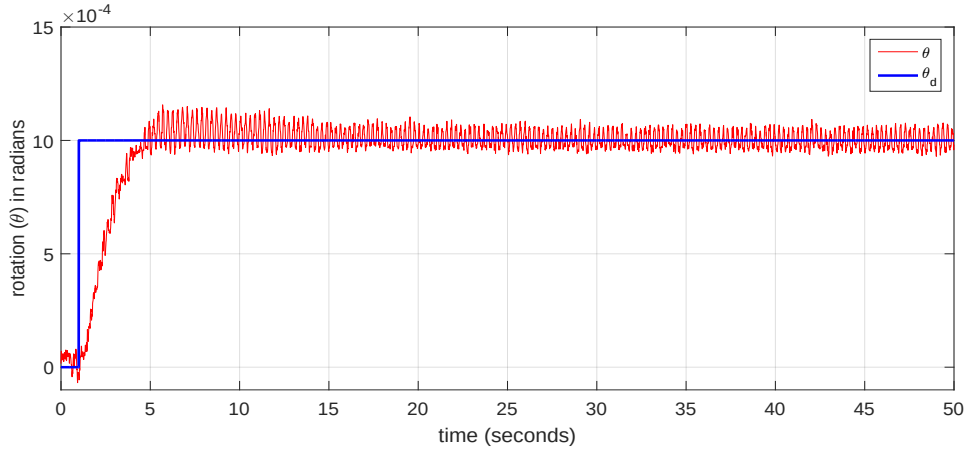

(49b) Slewing.

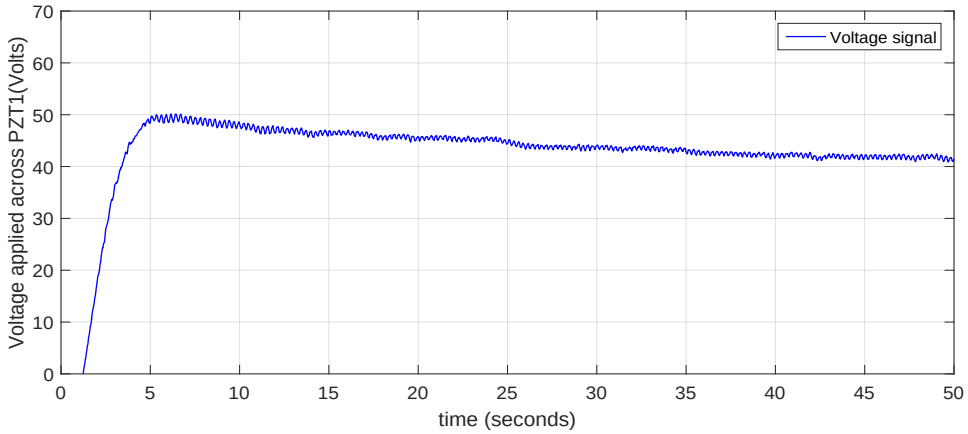

(49c) Control effort in Volts.

Figure 49: Slewing (Experiment) for $\delta = 0.0001$ using controller 2 with gains $\lambda = 1$, $K_\theta = 0.5$, $K_\xi = 0.5$.

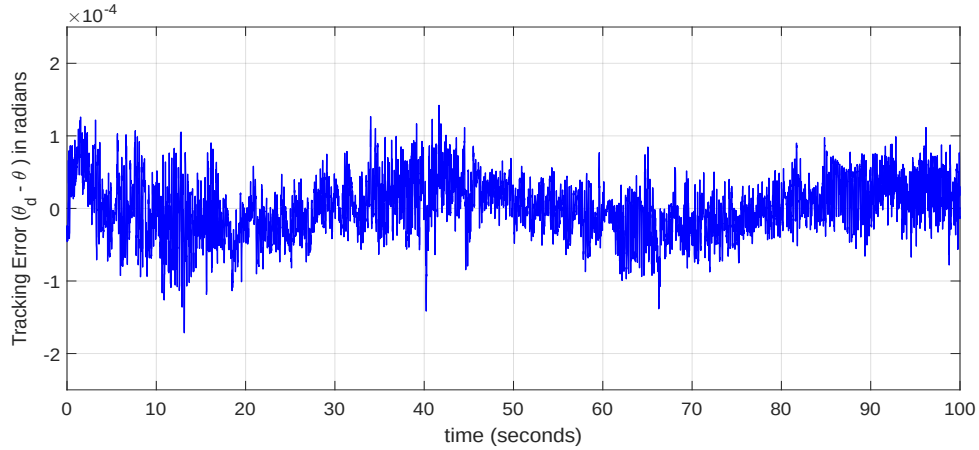

(50a) Tracking error.

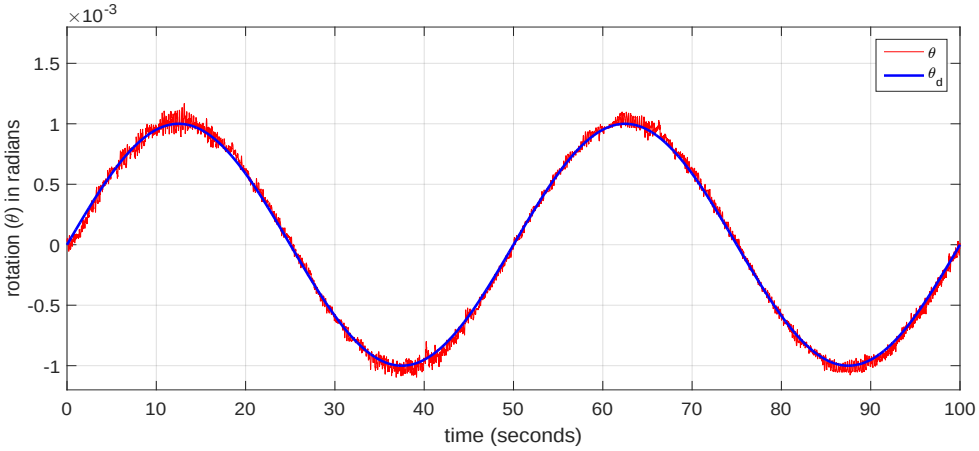

(50b) Trajectory tracking.

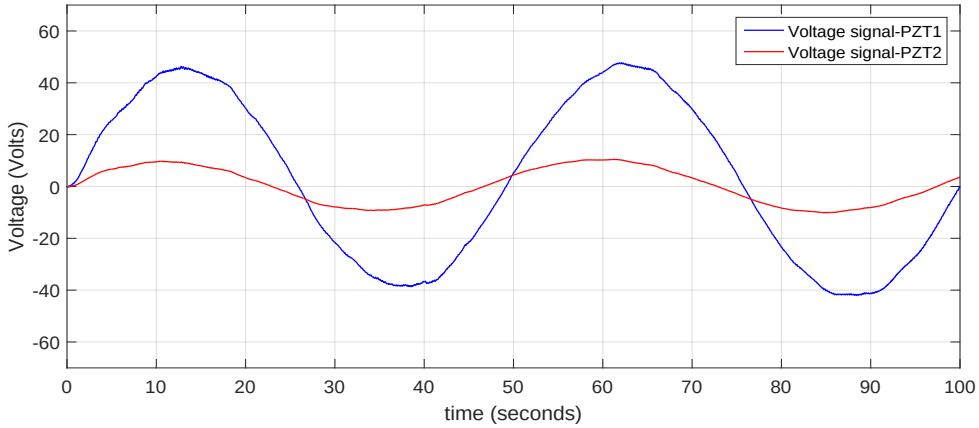

(50c) Control effort in Volts.

Figure 50: Trajectory tracking (Experiment) for $\delta = 0.0001$ using controller 2 distributed PZT (configuration 2) with gains $\lambda = 2$, $K_\theta = 0.5$, $K_\xi = 0.5$.

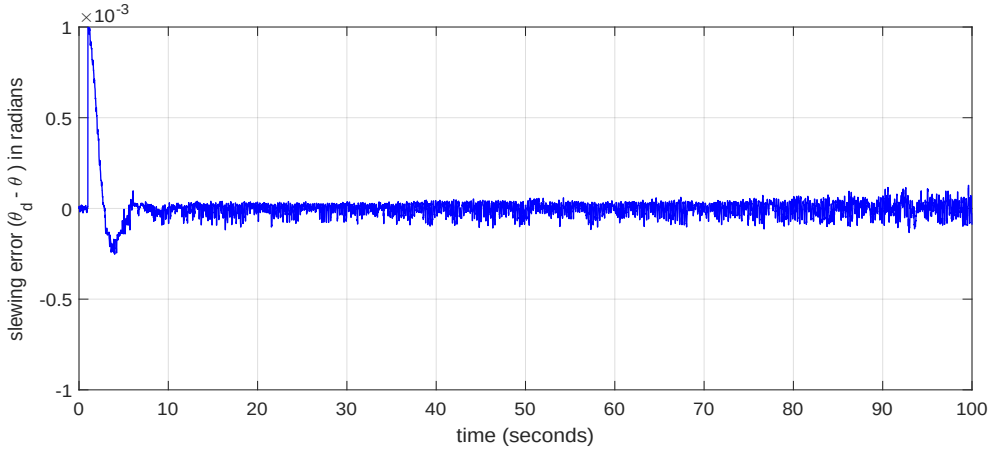

(51a) Slewing error.

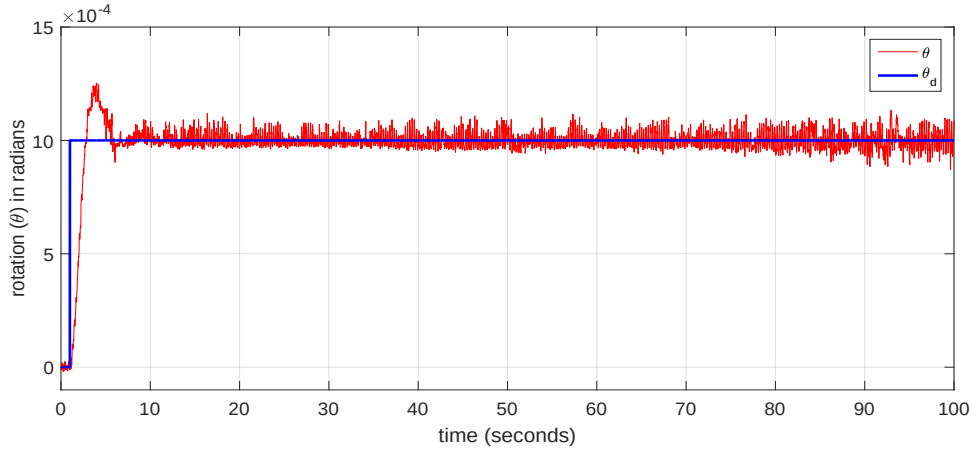

(51b) Slewing.

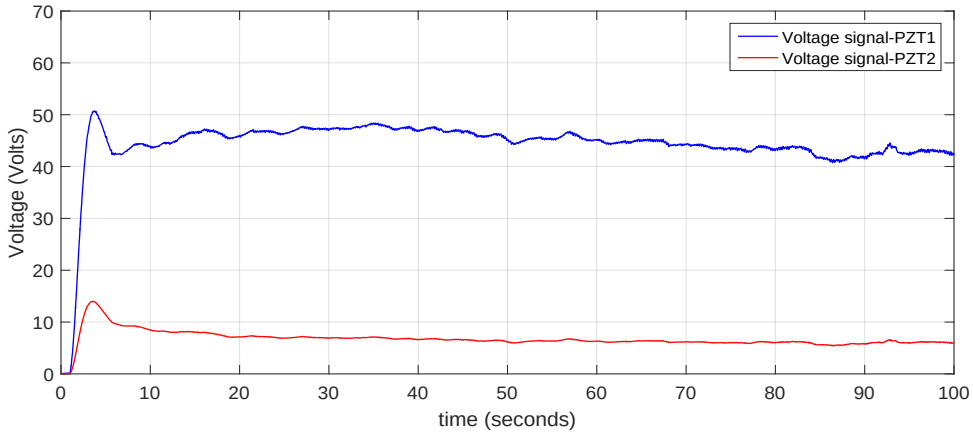

(51c) Control effort in Volts.

Figure 51: Slewing (Experiment) for $\delta = 0.0001$ using controller 2 distributed PZT (configuration 2) with gains $\lambda = 2$, $K_\theta = 0.5$, $K_\xi = 0.5$.

6.5 Comparison of Beam Deflection During Tracking (Simulations vs. Experiments)

The deflections of the beam estimated from simulation and experiment, while tracking the sinusoidal signal from 0 radians to 0.001 radians between the time interval 100 to 110 seconds using controller 1 is shown in Figs. 52 and 53. It can be observed that the difference between the deflections obtained from simulations to that of experiments is drastically different, which was observed in all the cases. To investigate this, we plot tip deflection in both cases including the effect of 'θ' rotation (see Figs. 54 and 55). The amplitudes of tip deflections are comparable. The phase difference between these plots is the reason for disparity between beam deflections. Further analysis is needed to quantify this difference exactly, this phase difference could be because of the ball bearing dynamics and friction.

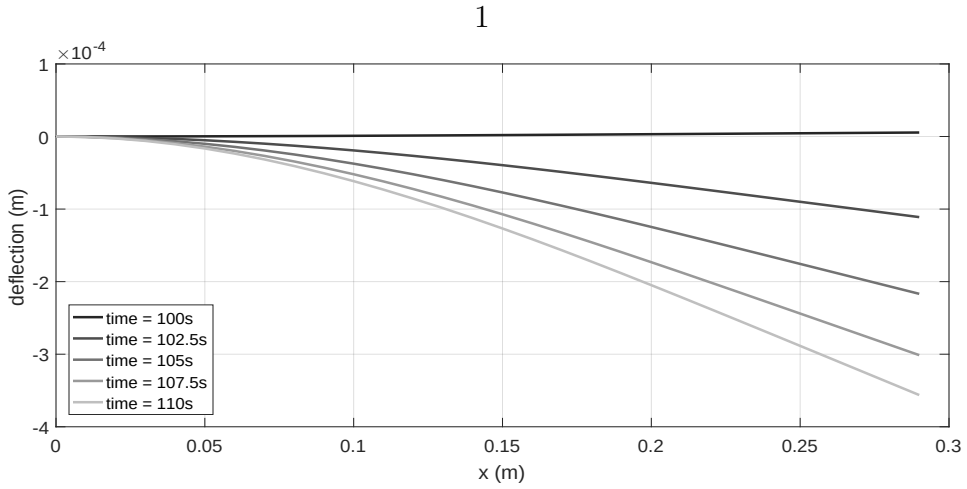

Figure 52: Bending in the beam while tracking the sinusoidal signal from 0 to 0.001 radians using controller 1, computed from simulation.

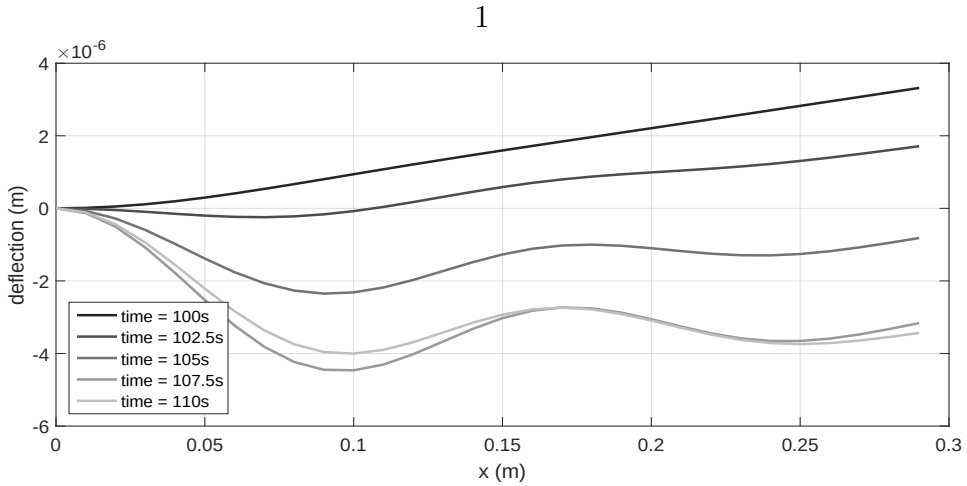

Figure 53: Bending in the beam while tracking the sinusoidal signal from 0 to 0.001 radians using controller 1, estimated from experiments.

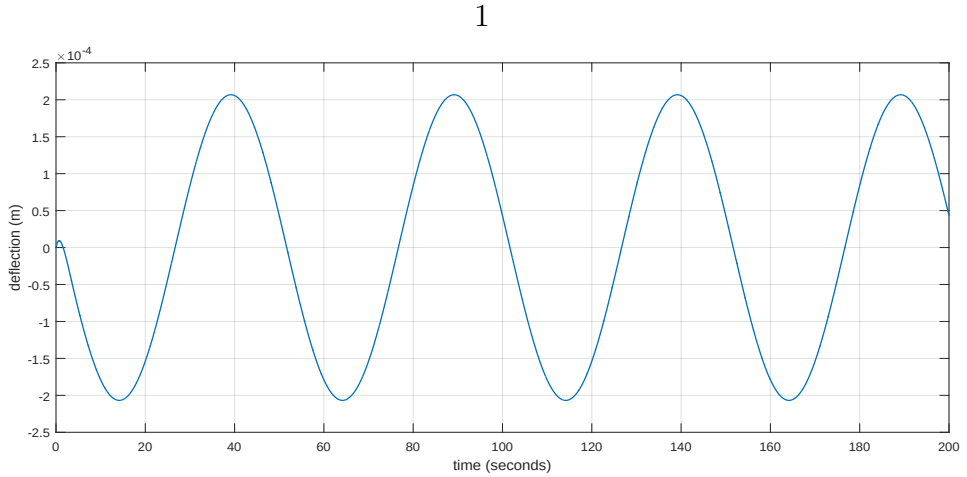

Figure 54: Tip deflection of the beam while tracking a sinusoidal signal using controller 1, computed from simulation.

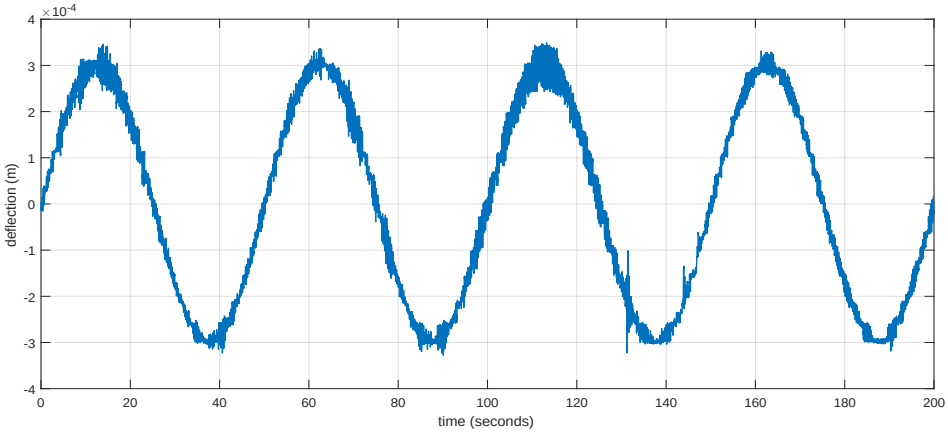

Figure 55: Tip deflection of the beam while tracking the sinusoidal signal using controller 1, estimated from experiments .

7 Conclusion

In this thesis, we derived nonlinear equations of motion that describe the 1-DOF rotation of a spacecraft with strain-actuated solar arrays. The equations form a nonlinear ODE-PDE model, with ODE describing the rotation of the hub and PDE describing the flexible dynamics. The control objective of attitude control was achieved using the inertial coupling between the cylinder and the flexible appendage. The control law computes the beam dynamics required to achieve the attitude. These beam dynamics and desired attitude signal were used to close the loop of the system. The control law's were designed in terms of a variable (δ) that scales the stiffness term. The stability of the closed-loop system for unit scaling ($\delta = 1$) was proved using the Lyapunov direct method. It was observed that this system is Input-to-State stable with the help of an ISS-Lyapunov function. This property is used to define a range of values for the variable (δ) that makes the closed-loop system stable. The closed loop system was simulated for different δ values to verify trajectory tracking and slewing. To test the control algorithms in real-time, we developed an experimental setup. The setup includes a cylinder and a beam, connected using an interference fit. Strain actuation in the beam was achieved using piezoelectric actuators. The quasi-static actuator model used for SASA experiments, was validated by comparing tip deflections of a cantilever beam obtained from simulations against experimental measurements. On the experimental setup, we achieved controlled cylinder rotation using the strain-actuation on the beam, which validates the SASA control algorithms. The strain-actuation was extended to a distributed actuation configuration with multiple PZTs. This model was used to test the controllers in distributed configuration for trajectory tracking and slewing. The control effort in the experiments was more than predicted during simulations due to modeling errors and parametric uncertainties.

8 References

[1] Blackmore, L., Murray, E., Scharf, D. P., Aung, M., Bayard, D., Brugarolas, P., Hadaegh, F., Lee, A., Milman, M., Sirlin, S., et al., "Instrument Pointing Capabilities: Past, Present, and Future," *AAS Guidance and Control Conference*, Breckenridge, Colorado, Feb. 2011.

[2] Pong, C. M., *High-precision pointing and attitude estimation and control algorithms for hardware-constrained spacecraft*, Ph.D. thesis, Massachusetts Institute of Technology, 2014.

[3] Knapp, M., Smith, M., Pong, C., Nash, J., and Seager, S., "ExoplanetSat: High Precision Photometry for Exoplanet Transit Detections in a 3U," *IAC 16th Symposium on Small Satellite Missions*, 2012, IAC-12-B4.

[4] "Exo-C Imaging Nearby Worlds," *https*: *//exoplanets.nasa.gov/stdt/Exo-C_InterimReport.pdf*.

[5] Guelman, M., Kogan, A., Livne, A., Orenstein, M., and Michalik, H., "Acquisition and pointing control for inter-satellite laser communications," *Aerospace and Electronic Systems, IEEE Transactions on*, Vol. 40, No. 4, 2004, pp. 1239–1248.

[6] Lucke, R. L., Sirlin, S. W., and San Martin, A. M., "New definitions of pointing stability-ac and dc effects," *Journal of the Astronautical Sciences*, Vol. 40, 1992, pp. 557–576.

[7] Cowen, R., "The Wheels Come Off Kepler," *Nature*, Vol. 497, No. 7450, 2013, pp. 417–418.

[8] Tafazoli, M., "A study of on-orbit spacecraft failures," *Acta Astronautica*, Vol. 64, No. 2, 2009, pp. 195–205.

[9] Smith, M. J., Grigoriadis, K. M., and Skelton, R. E., "Optimal Mix of Passive and Active Control Structures," *Journal of Guidance, Control, and Dynamics*, Vol. 15, No. 4, July 1992, pp. 912–919.

[10] Herber, D. R., McDonald, J. W., Alvarez-Salazar, O. S., Krishnan, G., and Allison, J. T., "Reducing Spacecraft Jitter During Satellite Reorientation Maneuvers via Solar Array Dynamics," *AIAA/ISSMO Multidisciplinary Analysis and Optimization Conference*, No. AIAA 2014-3278, Atlanta, GA, USA, June 2014.

[11] Balas, M. J., "Active Control of Flexible Systems," *Journal of Optimization Theory and Applications*, Vol. 25, No. 3, July 1978, pp. 415–436.

[12] Alvarez-Salazar, O., Aldrich, J., Filipe, N., Allison, J., and Chung, S.-J., "Strain Actuated Solar-Arrays for Precision Pointing of Spacecraft," *AAS Guidance, Navigation, and Control Conference*, Breckenridge, Colorado, Feb. 2016.

[13] Chilan, C. M., Herber, D. R., Nakka, Y. K., Chung, S.-J., and Allison, J. T., "Co-Design of Strain-Actuated Solar Arrays for Precision Pointing and Jitter Reduction," *57th AIAA/ASCE/AHS/ASC Structures, Structural Dynamics, and Materials Conference*, 2016, p. 0162.

[14] Chilan, C. M., Herber, D. R., Nakka, Y. K., Chung, S.-J., and Allison, J. T., "Co-Design of Strain-Actuated Solar Arrays for Precision Pointing and Jitter Reduction," *AIAA Journal (to be submitted)*.

[15] Meirovitch, L., *Dynamics and Control of Structures*, John Wiley & Sons, 1990.

[16] Hodges, D. H. and Pierce, G. A., *Introduction to Structural Dynamics and Aeroelasticity*, Cambridge University Press, 2nd ed., 2011.

[17] Junkins, J. L. and Kim, Y., *Introduction to Dynamics and Control of Flexible Structures*, AIAA, 1st ed., 1993.

[18] Spong, M. W., *Underactuated mechanical systems*, Springer Berlin Heidelberg, Berlin, Heidelberg, 1998, pp. 135–150.

[19] Chung, S.-J., Slotine, J.-J. E., and Miller, D. W., "Propellant-Free Control of Tethered Formation Flight, Part 2: Nonlinear Underactuated Control," *Journal of Guidance, Control, and Dynamics*, Vol. 31, No. 5, sep 2008.

[20] Fati-Saber, R., "Nonlinear control and reduction of underactuated systems with symmetry. I. Actuated shape variables case," *Decision and Control, 2001. Proceedings of the 40th IEEE Conference on*, Vol. 5, 2001, pp. 4158–4163 vol.5.

[21] Krstic, M. and Smyshlyaev, A., *Boundary control of PDEs: A course on backstepping designs*, Vol. 16, Siam, 2008.

[22] Dashkovskiy, S. and Mironchenko, A., "Input-to-state stability of infinite-dimensional control systems," *Mathematics of Control, Signals, and Systems*, Vol. 25, No. 1, 2013, pp. 1–35.

[23] Bisplinghoff, R. L., Ashley, H., and Halfman, R. L., *Aeroelasticity*, Addison-Wesley, 1995.

[24] Rao, S. S. and Sunar, M., "Piezoelectricity and Its Use in Disturbance Sensing and Control of Flexible Structures: A Survey," *Applied Mechanics Reviews*, Vol. 47, No. 4, April 1994, pp. 113–123.

[25] Bailey, T. and Hubbard Jr., J. E., "Distributed Piezoelectric-Polymer Active Vibration Control of a Cantilever Beam," *Journal of Guidance, Control, and Dynamics*, Vol. 8, No. 5, Sept. 1985, pp. 605–611.

[26] Crawley, E. F. and Luis, J. D., "Use of Piezoelectric Actuators as Elements of Intelligent Structures," *AIAA Journal*, Vol. 25, No. 10, Oct. 1987, pp. 1373–1385.

[27] Fanson, J. L. and Chen, J. C., "Structural Control by the Use of Piezoelectric Active Members," *NASA-Langley Research Center NASA/DOD Control/Structures Interaction Technology*, 1986, pp. 809–829.

[28] Moheimani, S. O. M. and Fleming, A. J., *Piezoelectric Transducers for Vibration Control and Damping*, Springer, 1st ed., 2006.

[29] Alvarez-Salazar, O. S. and Iliff, K., "Destabilizing Effects of Rate Feedback on Strain Actuated Beams," *Journal of Sound and Vibration*, Vol. 221, No. 2, March 1999, pp. 289–307.

[30] Crawley, E. F. and Anderson, E. H., "Detailed models of piezoceramic actuation of beams," *Journal of Intelligent Material Systems and Structures*, Vol. 1, No. 1, 1990, pp. 4–25.

[31] Moheimani, S. R. and Fleming, A. J., *Piezoelectric transducers for vibration control and damping*, Springer Science & Business Media, 2006.

[32] "IEEE Standard on Piezoelectricity," *ANSI/IEEE Std 176-1987*, 1988.

[33] Paranjape, A. A., Chung, S.-J., Hilton, H. H., and Chakravarthy, A., "Dynamics and Performance of Tailless Micro Aerial Vehicle with Flexible Articulated Wings," *AIAA Journal*, Vol. 50, No. 5, May 2012, pp. 1177–1188.

[34] Paranjape, A. A., Guan, J., Chung, S.-J., and Krstic, M., "PDE Boundary Control for Flexible Articulated Wings on a Robotic Aircraft," *IEEE Transactions on Robotics*, Vol. 29, No. 3, June 2013, pp. 625–640.

[35] Manecy, A., Marchand, N., and Viollet, S., "RT-MaG: an open-source SIMULINK Toolbox for Real-Time Robotic Applications," *IEEE International Conference on Robotics and Biomimetics*, Bali, Indonesia, Dec. 2014.